Dissertation
submitted to the
Combined Faculties for the Natural Sciences
and for Mathematics
of the Ruperto-Carola University of Heidelberg,
Germany
for the degree of
Doctor of Natural Sciences

Put forward by
Dipl.-Phys. Marcel Vogler
born in Heilbronn

Oral examination: 27.05.2009

Elementary kinetic modelling applied to solid oxide fuel cell pattern anodes and a direct flame fuel cell system

Referees:	**Prof. Dr.**	**Annemarie Pucci**
	Priv.-Doz. Dr.	**Wolfgang G. Bessler**

Elementarkinetische Modellierung von Festoxid- und Direktflammen-Brennstoffzellen

Zusammenfassung: Im Rahmen dieser Arbeit wurde ein Modell zur Vorhersage makroskopischer Zellcharakteristika von Festoxid-Brenstoffzellen (Solid Oxide Fuel Cell, SOFC) entwickelt und zur Untersuchung verschiedener Systeme verwendet. Das Modell basiert auf einer elementarkinetischen Beschreibung elektrochemischer Prozesse und den grundlegenden Erhaltungsprinzipien für Masse und Energie. Es erlaubt eine quantitative Vorhersage von Zellspannung und -strom und eröffnet damit gute Validierungsmöglichkeiten. Ziel der Arbeit ist die Identifizierung von ratenbestimmenden Prozessen und die Aufklärung des Reaktionsweges beim Ladungstransfer. Durch die numerische Simulation von Experimenten an Modellanoden ist es gelungen, einen Wasserstofftransfer als wahrscheinlichsten Ladungstransfermechanismus zu identifizieren und den Einfluß von Diffusionsprozessen aufzuzeigen. Die Anwendung der Wasserstoff-Kinetik auf das Komplettsystem der Direktflammen-Brennstoffzelle (direct flame fuel cell, DFFC) zeigte, dass damit auch die elektrochemische Umsetzung von CO möglich ist. Verbessungsvorschläge, gewonnen aus der Quantifizierung der Verlustprozesse im DFFC System, lassen eine Leistungssteigerung von 80% erwarten.

Elementary kinetic modelling applied to solid oxide fuel cell pattern anodes and a direct flame fuel cell system

Abstract: In the course of this thesis a model for the prediction of polarisation characteristics of solid oxide fuel cells (SOFC) was developed. The model is based on an elementary kinetic description of electrochemical reactions and the fundamental conservation principles of mass and energy. The model allows to predict the current-voltage relation of an SOFC and offers ideal possibilities for model validation. The aim of this thesis is the identification of rate-limiting processes and the determination of the elementary pathway during charge transfer. The numerical simulation of experiments with model anodes allowed to identify a hydrogen transfer to be the most probable charge-transfer reaction and revealed the influence of diffusive transport. Applying the hydrogen oxidation kinetics to the direct flame fuel cell system (DFFC) showed that electrochemical oxidation of CO is possible based on the same mechanism. Based on the quantification of loss processes in the DFFC system, improvements on cell design, predicting 80% increase of efficiency, were proposed.

Contents

Chapter 1

Introduction and background

1.1 Introduction

The ever increasing demand for energy imposes severe problems on the world society. The emission of greenhouse gases from the consumption of fossil fuels is held responsible for negative effects on the worlds climate. Lawyers start to see legitimations for small countries suing industrial nations for damage. Damage resulting from the extravagance in the use of fossil fuels and the resulting existential threats for small states like Tuvalu [1]. Beside the ideal solution of reducing the energy consumption, increasing the efficiency of energy utilisation can help to reduce green-house gases.

Today, electrical energy is generated mainly via thermomechanical processes. Heat is generated via combustion or thermonuclear reactions and subsequently converted first into mechanical and ultimately into electrical energy. All thermo-mechanical processes, even in an ideal system, obey Carnot's theorem which states, that efficiency of such a process cannot exceed a certain limit. A fuel cell is not based on thermo-mechanical processes but electrochemically converts the energy stored in the fuel directly into electrical energy; its efficiency is therefore not limited by Carnot's theorem. As 66% of the world's demand on electrical energy is generated from fossil fuels [2], the use of fuel cells provides a good way to increase the efficiency of energy conversion [3] and may therefore aid in reducing the severe climate problems of our planet.

Today, fuel cell systems range from centralised multi-megawatt power plants over domestic heat and power co-generation down to battery-replacement in mobile electronic devices. Although all systems are available at least on the basis of prototypes, the commercial breakthrough still faces significant challenges concerning long-term stability, cost reduction and performance improvement. A major obstacle in overcoming this challenges is the still poor understanding of the underlying physical and chemical processes taking place

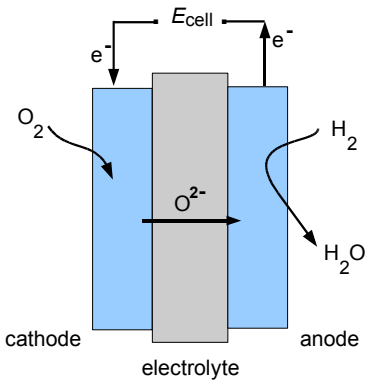

Figure 1.1: *Schematic drawing of a solid oxide fuel cell run on hydrogen and oxygen.*

at cell level [4]. Understanding these elementary processes is the key to optimising cell design and finding alternative materials for the reduction of costs and the increase of long-term stability [3, 5, 6].

Gaining experimental insight into the fundamental processes is difficult, firstly, because the electrochemical reactions take place at the solid-solid interface of the electrodes and, secondly, because of the tight coupling between transport and electrochemical reactions. This is true even more as these processes occur inside the complex structure of porous electrodes. However, macroscopic electrochemical characterisation can be performed with relative ease.

To bridge the gap between the experimental characterisation on a macroscopic level and the elementary processes ultimately governing fuel cell performance on the microscopic scale we have developed a detailed physico-chemical model. The model is capable of predicting cell performance based on fundamental physical processes and therefore allows to identify rate-limiting steps and helps understanding their relations.

In the remainder of this chapter a general overview of fuel cells and solid oxide fuel cells will be given. In Ch. 2 the model is developed and afterwards used for numerical simulations of Ni/YSZ-based model anodes in Ch. 3. Based on the identification of the charge-transfer kinetics, design improvements for a direct flame fuel cell system will be derived in Ch. 4. The thesis is closed by a summary.

1.2 Background

1.2.1 Fuel cells

A fuel cell is an electrochemical device that converts chemical energy directly into electrical energy. Unlike in batteries, where the chemical reactants are

contained within the electrochemical device, a fuel cell only provides a pathway for the electrochemical reaction to proceed, whereas fuel and oxidising agents are supplied externally. In principle any exothermic chemical reaction that can be separated into a reduction reaction and an oxidation reaction can be exploited in a fuel cell for the generation of electrical power.

Global reaction. Typical reactions are the full oxidation of hydrogen or carbon monoxide with molecular oxygen [5, 6]. If hydrogen is used as a fuel and oxygen as the oxidiser the global reaction is the hydrogen-oxidation reaction,

$$\mathrm{H_2} + {}^1\!/_2\mathrm{O_2} \rightleftharpoons \mathrm{H_2O} \; . \tag{1.1}$$

Half-cell reactions. In a fuel cell, the fuel and oxidiser are separated by a gas-tight electrolyte and the global reaction is split up into two half-cell reactions: an oxygen reduction reaction taking place at the cathode,

$${}^1\!/_2\mathrm{O_2} + 2\mathrm{e}^- \rightleftharpoons \mathrm{O}^{2-} \; , \tag{1.2}$$

and a hydrogen oxidation reaction occurring at the anode,

$$\mathrm{H_2} + \mathrm{O}^{2-} \rightleftharpoons \mathrm{H_2O} + 2\mathrm{e}^- \; . \tag{1.3}$$

Efficiency. The total amount of energy released by the chemical reaction Eq. 1.1 is the free enthalpy ΔH. This energy would be converted into heat if the reaction was allowed to proceed freely. In an ideal fuel cell, only the free reaction enthalpy $\Delta G = \Delta H - T\Delta S$ can be converted into electrical energy. From this, the maximum theoretical efficiency of a fuel cell can be calculated as

$$\eta_{\mathrm{FC}} = \frac{\Delta G}{\Delta H} \; . \tag{1.4}$$

For the generally-used thermomechanical processes for energy conversion, the theoretical limit of efficiency is given by Carnot's theorem [5]. It states that the maximum efficiency of a thermomechanical process operating between a hot state with temperature T_1 and a cold state (T_2) can be calculated by

$$\eta_{\mathrm{Carnot}} = \frac{T_1 - T_2}{T_1} \; . \tag{1.5}$$

At a system temperature of 800 K and a ambient temperature of 300 K a fuel cell running on hydrogen works with a theoretical efficiency of 80% whereas a thermo-mechanical process is limited to 60% [3].

Operating principle. The basic operating principle of a fuel cell (Fig. 1.1) can be described as a concentration cell. As any electrochemical device, a fuel

Table 1.1: *Overview of fuel cell types indicating operating temperature, the type of electrolyte, charge carriers and fuel.*

Fuel cell type	Operating temperature	Electrolyte (charge carrier)	Fuel
Alkaline fuel cell (AFC)	80 °C	Potassium hydroxide (OH^-)	H_2
Polymer electrolyte membrane fuel cell (PEFC)	80 °C (today), 150 °C (future)	Ionomer (conducting polymer) (H^+)	H_2 ($CO < 10$ ppm today, ≤ 1000 ppm future)
Direct methanol fuel cell (DMFC)	80 °C	Ionomer (H^+)	Methanol
Phosphoric acid fuel cell (PAFC)	200 °C	Immobilized phosphoric acid (H^+)	H_2 ($CO < 5$ %)
Molten carbonate fuel cell (MCFC)	650 °C	Molten alkali carbonates (CO_3^{2-})	H_2, CO, hydrocarbons (internal reforming)
Solid oxide fuel cell (SOFC)	900 °C (today), 600 °C (future)	Oxide ceramic (O^{2-})	H_2, CO, hydrocarbons (direct utilization)

cell consists of an anode (where the fuel, H_2, is oxidised), a cathode (where the the oxidiser, here molecular oxygen, O_2, is reduced) and an ionically conducting electrolyte establishing a concentration gradient by separating the anode and cathode gas volumes. Due to the concentration gradient an electrical voltage, $E_{\text{cell}}^{\text{th}}$, develops between the electrodes. This maximum voltage of about 1.2 V for a fuel cell running on hydrogen can be calculated via [7],

$$E_{\text{cell}}^{\text{th}} = -\frac{1}{zF}\Delta G\,, \tag{1.6}$$

where z is the number of electrons transferred and F is Faraday's constant. The free enthalpy of reaction depends on the concentrations of reactants and products in the gas-mixture actually fed to the anode and cathode. Generally the gases supplied to the electrodes are not pure (e.g., ambient air is used frequently as oxidiser), and from Eq. 1.6 the Nernst equation follows [4]:

$$E_{\text{cell}}^{\text{th}} = -\frac{\Delta G^0}{zF} - \frac{RT}{zF}\cdot \ln\frac{a_{\text{H}_2\text{O}}}{a_{\text{H}_2} a_{\text{O}_2}^{0.5}}\,, \tag{1.7}$$

where ΔG^0 is the free enthalpy of reaction at standard conditions, R the ideal gas constant, T the temperature and a_i the activities of the species.

1.2.2 Types of fuel cells

Since in 1839 William Groove and Walter Schönbein discovered the operation principle of a fuel cell, a number of different realisations of the basic principle have been developed. Depending on the materials used for anode, electrolyte and cathode, the resulting fuel cell exhibits different characteristics in terms of operating temperature or fuel acceptance. The most common fuel cell types are summarised in Tab. 1.1. The different fuel cells can be characterised by the type of electrolyte used, because its physical properties (ionic conductivity and physical state) determines the operating conditions with respect to temperature [3].

Why SOFC? All types of fuel cells in Tab. 1.1 are currently subject of academic and industrial research and it cannot be forseen which, if any of them, will be dominating in future. This thesis focuses on the solid oxide fuel cell (SOFC), because it is the most fuel-flexible of all fuel cell systems developed today. It can run on H_2, CO-rich mixtures and hydrocarbons (gaseous or gasified liquid hydrocarbons and even on flame exhaust gases, Sec. 4). In today's economy, which is based mainly on hydrocarbon energy resources, SOFCs can be operated with considerably less effort for fuel processing than H_2-operated fuel cells [8].

1.2.3 Solid oxide fuel cell

A solid oxide fuel cell is made of all-solid material and derives its name from the oxidic electrolyte. The electrolyte, responsible for the conduction of oxygen ions, is sandwiched between two electrodes. The electrodes are formed by a porous structure consisting of an electronically conducting phase, an ionically conducting phase and a gas phase for the supply of fuel and oxidiser. Fig. 1.2 shows a micrograph of the membrane electrode assembly (MEA) of a typical electrolyte-supported cell structure. From left to right, the figure shows the porous cathode, the dense layer of the electrolyte and the porous cermet anode.

Operating conditions. Typical SOFC operating conditions are high temperatures (between 600 °C and 1000 °C), a highly reducing atmosphere at the anode side and an oxidising atmosphere at the cathode side. The high temperature level is crucial for SOFC operation as the ionic conductivity of the solid electrolyte depends exponentially on temperature and would decrease the performance considerably at lower temperatures. Also from the high operating temperatures follow the capability of the SOFC to run directly on hydrocarbon fuels and the possibility to use non-noble metals for the catalysis of electrochemical reactions. Beside these positive effects, the

Figure 1.2: *Scanning electron micrograph (SEM) of an electrolyte-supported solid oxide fuel cell with porous electrodes. SEM courtesy of Prof. Ellen Ivers-Tiffée, Institut für Werkstoffe der Elektrotechnik, Universität Karlsruhe.*

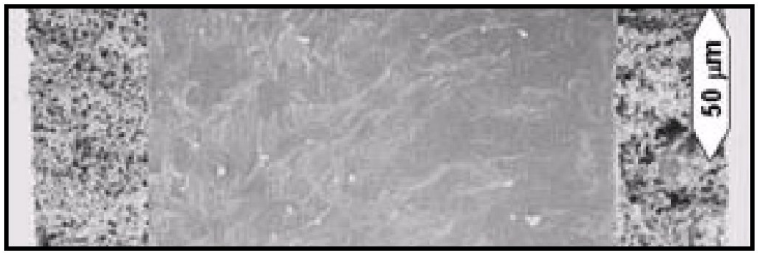

need for high-temperature sealing techniques and thermal stresses resulting from different thermal expansion coefficients of the individual materials are significant drawbacks. Furthermore the choice of materials is limited by the need for high redox stability of the electrolyte which is in contact with both, the anodic reducing and the cathodic oxidising atmosphere [8, 9].

Application areas. The most prominent application area for SOFC-based fuel cell systems are stationary power plants. At this relatively large scale (several kW to MW), the high temperatures and the associated structural problems during heating up and cooling down can be handled most effectively. In fact, the high temperature level can be positive if SOFCs are used in combination with gas-turbines [10, 11]. For these hybrid systems, overall efficiencies of around 70% can be expected. SOFC systems are also being developed as auxiliary power units (APU) for the use in trucks or mobile homes, providing about 5 kW. Today, the power to supply the on-board electrical devices (air-conditioning, refrigerator, television etc.) is generated by idling the combustion engine of this vehicles under inefficient conditions. SOFC-based APUs running on reformate Diesel can help to significantly increase efficiency [12]. Finally, the fuel flexibility and high-temperature-tolerance of SOFCs opens up niche market segments [13, 14]. In Ch. 4 studies on the direct flame fuel cell system will be presented. Running on the exhaust of a hydrocarbon flame, this system is able to produce about 200 mW electrical power.

1.2.4 SOFC materials

Electrolyte. The dense layer of the solid electrolyte plays an important role in the SOFC design. It has to be a good oxygen-ion conductor, because all current drawn from the cell has to pass through the electrolyte in terms of oxygen ions. On the other hand, it must electronically separate the anode from the cathode to prevent electronic current from passing through the electrolyte and short-circuit the fuel cell. As the separator between the anode and the cathode side it needs good redox stability at elevated temperatures

to withstand SOFC operating conditions. The traditional material is yttria-stabilised zirconia (YSZ, $Y_{2x}Zr_{1-2x}O_{2-x}$, where x is the concentration of the dopant in mol-% Y_2O_3 in ZrO_2). First used in 1937 by Baur and Preis it is still widely used in SOFC systems of today. The doping of ZrO_2 with trivalent yttrium ions forms oxygen ion vacancies in the host lattice. This allows for vacancy-mediated conduction of oxygen ions on and stabilises the cubic phase of zirconia at higher temperatures. The ionic conductivity ranges from 0.01 S/cm at 700 °C to about 0.1 S/cm at 1000 °C and additionally depends on dopant concentration.

Research is carried out to reduce the operating temperature of SOFCs using different electrolyte materials which show higher ionic conductivities at relatively low temperatures. Among these materials gadolinium-doped ceria (GDC, $Gd_{2x}Ce_{1-2x}O_{2-x-\delta}$, x=dopant concentration of Gd_2O_3 in CeO_2, δ depending on oxygen partial pressure) is a promising candidate. It shows ionic conductivities five times higher than YSZ at 700 °C [8]. The ceria-based electrolytes are mixed ionic and electronic conducting materials (MIEC). At low oxygen partial pressured these materials become electronically conducting. However, as only the anodic side of a SOFC is exposed to a reducing atmosphere, the electronic current hardly reaches the fully oxidised cathodic regions of the electrolyte and the positive impact of the better ionic conductivity may outweigh the negative effect resulting from short-circuiting of the cell [15].

Anode. A typical SOFC anode is formed by a porous composite structure, consisting of an ionically conducting phase (often the same as used for the dense electrolyte) and an electronically conducting phase (e.g., nickel or copper). A traditional material system is Ni/YSZ which exhibits good chemical stability in the hot reducing atmosphere of the SOFC. At the elevated temperatures nickel is a good catalyst for electrochemical reactions, thus, noble metals hardly need to be used.

Cathode. For the cathode material, chemical stability under oxidising conditions at high temperatures as well as a good electronic conductivity for current collection are necessary. At the cathode mainly electronically conducting oxide ceramics are used. A typical example is strontium-doped lanthanum magnetite (LSM, $La_{1-x}Sr_xMnO_3$) which shows an electronic conductivity of about 10 S/cm at 700 °C .

1.2.5 Electrochemical characterisation

The most prominent techniques for the electrochemical characterisation of fuel cells are steady-state polarisation measurements (IV measurements) and electrochemical impedance spectroscopy (EIS). During an IV measurement

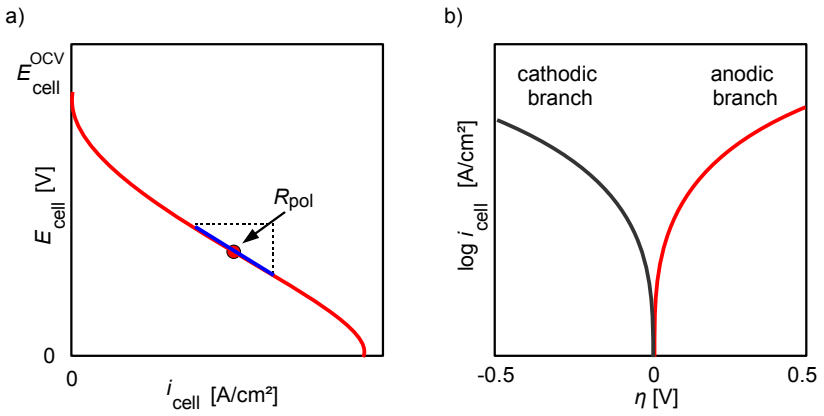

Figure 1.3: *Two representations of current-voltage relations (IV curves). a) Cell voltage plotted over the current density, used mainly in full SOFC setups. b) Tafel plot. The absolute value of the current density is plotted logarithmically over the overpotential* $\eta = E_{\text{cell}}^{\text{th}} - E_{\text{cell}}$*. This representation is used frequently in the context of reference electrode measurements. Anodic* ($\eta > 0$*, red) and cathodic* ($\eta < 0$*, dark) polarisations are possible.*

the cell voltage is measured with respect to a time-constant electrical load imposed on the cell. During EIS measurements a transient current is used for excitation.

IV curve. If a series of time-constant currents i with different absolute values are applied to a fuel cell, a current-voltage relation (IV curve, polarisation curve) results. In Fig. 1.3 two frequently used representations for IV measurements are shown :

a) Current-voltage relation. The actual cell voltage $E_{\text{cell}}(i)$ is plotted over the cell's current density. The actual cell voltage decreases with increasing current as internal loss processes depend on the cell current. Typically the measurements stop if the cell voltage drops below a certain value. This representation is mainly used in Ch. 4 for the characterisation of the direct flame fuel cell.

b) Tafel representation. Here, the absolute value of the current density is plotted over the difference between open-circuit voltage and actual cell voltage (the overpotential $\eta(i) = E_{\text{cell}}^{\text{OCV}} - E_{\text{cell}}(i)$). Typically, this representation is used with a logarithmic abscissa in the context of reference electrode measurements (Ch. 3). The Tafel representation may have an anodic and a cathodic branch. The anodic brach results from the operation of the fuel cell in the direction of hydrogen oxidation, the cathodic brach from the reverse reaction, using the fuel cell as an electrolyser.

Except for the cathodic brach in the Tafel plot, both representations contain the same information.

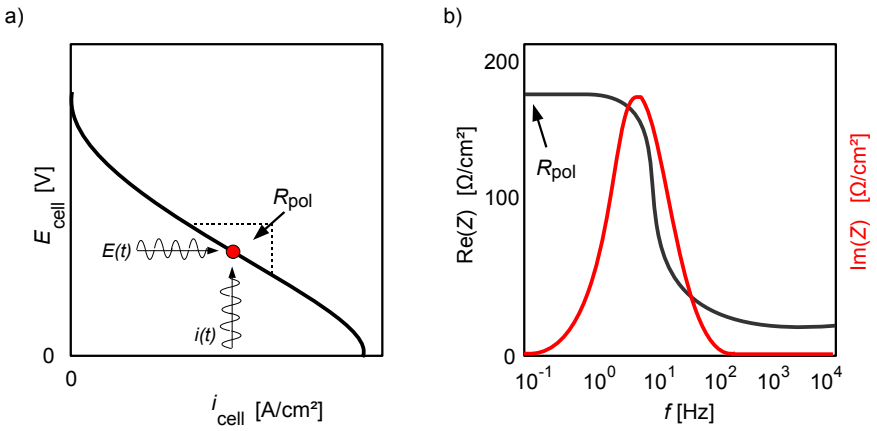

Figure 1.4: *Schematic of an electrochemical impedance spectroscopy measurements (EIS). a) Current-voltage relation showing operating point of EIS and the transients in current and voltage. b) Bode representation of the impedance answer of a system. The polarisation resistance R_{pol} can be derived from EIS and IV measurements.*

EIS. During electrochemical impedance spectroscopy a transient current signal $i(t)$ is imposed on the system and the answer, the impedance Z, is measured (Fig. 1.4). The amplitude of the excitation signal is usually chosen small (few mV) so that the system response is approximately linear to the excitation whereas the offset may be chosen arbitrarily (red circle in Fig. 1.4 a can be anywhere on the IV curve). If, for a series of different frequencies, the real and imaginary part of the impedance are plotted over the frequency, the so-called Bode representation results (Fig. 1.4 b).

From both types of measurements, EIS and IV, the polarisation resistance, R_{pol}, a frequently-used quantity for SOFC characterisation, can be derived. Using EIS, R_{pol} corresponds to the real part of the impedance at low frequencies. Using IV measurements the, polarisation resistance can be derived from the slope of the IV curve:

$$R_{\mathrm{pol}} = \frac{\mathrm{d}\eta}{\mathrm{d}i} \,. \tag{1.8}$$

The polarisation resistance is the main characteristic for the studies on model anodes in Ch. 3.

1.2.6 Model anodes

A technical fuel cell is optimised for power by increasing the active surface area of the electrodes. Consequently, such electrodes have a complex microstructure. The electrodes are highly porous structures with interpenetrating clusters of the electronic and ionic phases formed by differently sized particles. For studying elementary processes at the interface of the solid electrolyte and the solid electrode, special setups are frequently used [16–21]. In these setups, the MEA of an SOFC is reduced to simple geometries, typically a flat,

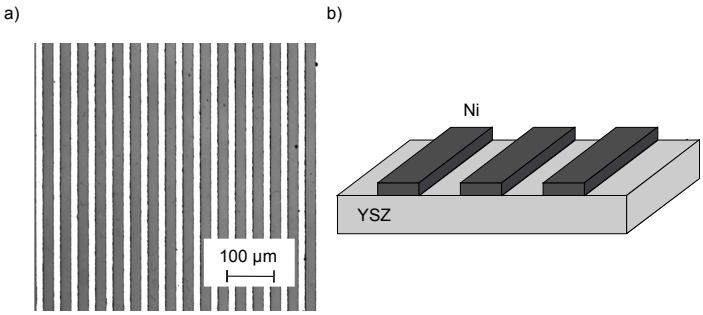

Figure 1.5: *Model anode. a) Micrograph of Ni/YSZ model anode. Dark nickel stripes form the electrode on a YSZ single crystal, the electrolyte (bright). b) Schematic view. Micrograph, courtesy of A. Bieberle-Hütter, ETH Zürich, Switzerland.*

dense electrolyte disc with non-porous electrode patterns on top (Fig. 1.5). These simplified electrodes reduce structural influences on the polarisation behaviour and allow to study the electrochemical processes in more detail.

Chapter 2

Physico-chemical modelling

The energy conversion capability of an SOFC is based on a variety of different electrochemical and physical processes which are tightly coupled and appear on different length scales ranging from sub-micrometer (electrochemical reactions) to centimeters (gas supply). To account for these processes adequately, a multi-scale model was developed including electrochemical processes, gas transport and the transport of charge. The different length scales are coupled via appropriate source terms. The model forms a system of time-dependent differential equations which is spatially discretised and numerically time-integrated to predict polarisation curves.

The smallest model level is an entity called species. The species forming part of the SOFC system may be charged or neutral atoms or molecules adsorbed on surfaces (e.g., H_{Ni}, O^{2-}_{YSZ}), freely existing in the gas phase (H_2^{gas}, O_2^{gas}), constituents of the lattice structure of bulk materials ($O^{X}_{O\,YSZ}$), solved as interstitials in bulk material ($H^{x}_{i\,Ni}$) or electrons in the conduction bands of the electrodes (e^-). All species are considered mobile and may undergo chemical reactions within the same phase (e.g., homogeneous gas-phase and surface reactions) or over phase boundaries (e.g., ad- and desorption reactions or electrochemical reactions).

Chemical reactions in the gas phase and on the surfaces of electrode and electrolyte are modelled by an elementary kinetic, thermodynamically consistent description of the reaction kinetics. The surface chemistry is treated within the mean-field approximation [22]. The elementary steps of electrochemical reactions are resolved and physically meaningful electrical potentials are used to calculate their rates instead of the widely-spread approach of deriving electrochemical reaction kinetics based on half-cell overpotentials [23–26].

Mass transport in the bulk gas phase occurs on the scale of millimeters to several centimetres and is modelled using a one-dimensional approach based on the Navier-Stokes equations. On a micrometer scale, the mass-transport in the porous structures of the electrodes are modelled by Stefan-Maxwell multi-component diffusion using averaged Bosanquet diffusion coefficients and

pressure driven Darcy-flow. Below the micrometer-scale, the interstitial bulk species and surface-adsorbed species are transported purely diffusive which we treat within the context of Fickian diffusion. The transport of charge and mass through the porous composite material of the electrodes is based on homogenisation approach using effective transport coefficients [27–29].

In the following the complete set of equations used for the simulations in Chapters 3 and 4 will be compiled. Although the experimental setups modelled in these chapters differ strongly, they can be consistently described within the same model framework developed in the remainder of this chapter. We will start with the general electrochemical properties of an SOFC, describe the elementary kinetic approach used to derive reaction rates and the electrical current, and describe the transport of heat and mass throughout the system.

2.1 Electrochemistry

In an electrochemical system such as the SOFC, the gradient in the electrochemical potential is the driving force for reactions occurring inside the system. If the system has reached equilibrium, this gradient has vanished and an electrical voltage E has formed between the electrodes. At equilibrium the relation [4, 5],

$$\Delta G = -zFE \,, \tag{2.1}$$

follows from thermodynamic considerations, relating the free reaction Enthalpy ΔG of the global reaction to the product of Faraday's constant,F, the number of transferred electrons, z, and the cell voltage, E. Globally, the hydrogen oxidation reaction can be written as,

$$\mathrm{H_2} + {}^1\!/_2\mathrm{O_2} \rightleftharpoons \mathrm{H_2O} \,. \tag{2.2}$$

Typically, for describing electrochemistry within an SOFC where the electrolyte (e.g., YSZ) is a solid oxygen ion conductor and the reactants and products are supplied in the gas phase, this reaction can be spatially separated into two half-cell reaction proceeding at the anode side,

$$\mathrm{H_2^{gas}} + \mathrm{O^X_{O\,YSZ}} \rightleftharpoons \mathrm{H_2O^{gas}} + \mathrm{V^{\bullet\bullet}_{O\,YSZ}} + 2\,\mathrm{e^-} \quad , \tag{2.3}$$

and the cathode side,

$$\frac{1}{2}\mathrm{O_2^{gas}} + \mathrm{V^{\bullet\bullet}_{O\,YSZ}} + 2\,\mathrm{e^-} \rightleftharpoons \mathrm{O^{2-}_{YSZ}} \,. \tag{2.4}$$

In the above equations Kröger-Vink notation was used, where $\mathrm{V^{\bullet\bullet}_{O\,YSZ}}$ denotes a oxygen vacancy in the bulk electrolyte, $\mathrm{O^{2-}_{YSZ}}$ a surface adsorbed oxygen ion and $\mathrm{O^X_{O\,YSZ}}$ an oxygen in the lattice structure of the bulk electrolyte.

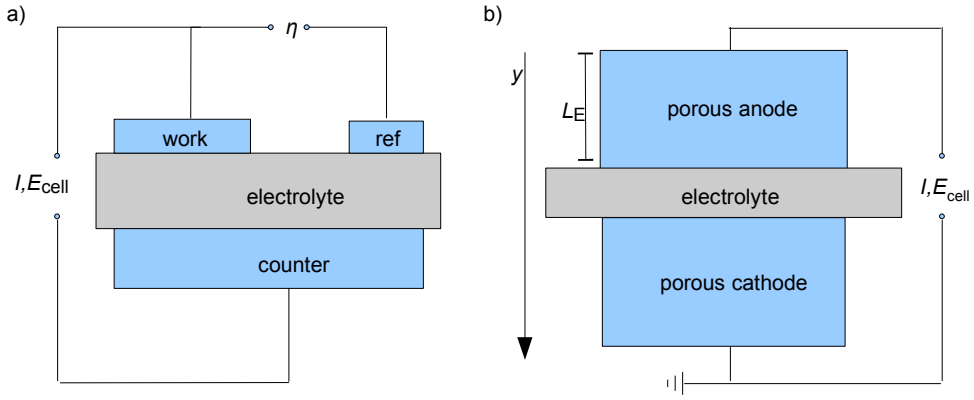

Figure 2.1: *Schematic representation of fuel cell setups. a) Reference electrode setup, used for studies on model anodes (Ch. 3). b) Full SOFC, used for simulations of direct-flame fuel cells (Ch. 4).*

For these reactions the potential difference in thermodynamical equilibrium between the electrolyte and the electrode, $\Delta\phi_{\text{equil}}$, can be calculated using the Nernst equation [7, 30]:

$$\Delta\phi_{\text{equil,an}} = \frac{\Delta G_{\text{an}}}{2F} - \frac{RT}{2F} \cdot \ln\left(\frac{a(\text{H}_2) \cdot a(\text{O}^{\text{X}}_{\text{O YSZ}})}{a(\text{H}_2\text{O}) \cdot a(\text{V}^{\bullet\bullet}_{\text{O YSZ}})}\right) \quad , \tag{2.5}$$

$$\Delta\phi_{\text{equil,ca}} = \frac{\Delta G_{\text{ca}}}{2F} - \frac{RT}{2F} \cdot \ln\left(\frac{a(\text{O}^{\text{X}}_{\text{O YSZ}})}{a(\text{O}_2)^{1/2} \cdot a(\text{V}^{\bullet\bullet}_{\text{O YSZ}})}\right) \quad . \tag{2.6}$$

The cell voltage at equilibrium is given by the difference in the electrical potential of the anode and the cathode:

$$E_{\text{equil}} = \Delta\phi_{\text{equil,ca}} - \Delta\phi_{\text{equil,an}} \, . \tag{2.7}$$

The two electrodes are at different potentials because of two potential steps $\Delta\phi$ forming at the interfaces of the electrode and the electrolyte at the anode and cathode [5]:

$$\Delta\phi_{\text{an}} = \phi_{\text{elde,an}} - \phi_{\text{elyt,an}} \text{ and } \Delta\phi_{\text{ca}} = \phi_{\text{elde,ca}} - \phi_{\text{elyt,ca}} \, , \tag{2.8}$$

where ϕ_{elde} is the electrical potential of the electrode and ϕ_{elyt} represents the electrical potential of the electrolyte just beyond the space-charge region. If current is drawn from the cell, the cell voltage and the potential steps become dependent on the cell current i:

$$E(i) = \phi_{\text{elde,ca}} - \phi_{\text{elde,an}}(i) \, . \tag{2.9}$$

Current-voltage relationships. The relationship between the cell voltage $E(i)$ and the cell current i forms the basis for evaluating polarisation behaviour and performance of a fuel cell. In the course of this thesis, experi-

mental data derived from two different fuel cell setups will be used and must be reflected in the model. These setups are: (1) A full SOFC comprising of porous composite electrodes and a dense ionically and electronically conducting electrolyte where cell voltage and cell current are measured between anode and cathode current collector (Fig. 2.1 b). (2) A reference electrode setup consisting of 3 non-porous electrodes and a purely ionically conducting electrolyte. This setup is used for studies on model anodes. In the latter, only the working and the counter electrode are polarised during experimental characterisation while the reference electrode remains unpolarised (Fig. 2.1 a).

Full SOFC. When porous electrodes are used that consist of an electrode and an electrolyte phase, the potential steps depend on the spatial position y along the electrode thickness and all potentials depend on the cell's current density i, except $\phi_{\mathrm{elde,ca}}$ which we set to zero as reference:

$$\Delta\phi_{\mathrm{elde,ca}} = \phi_{\mathrm{elde,ca}} - \phi_{\mathrm{elyt,ca}}(y) \quad \text{and } \Delta\phi_{\mathrm{elde,an}} = \phi_{\mathrm{elde,an}} - \phi_{\mathrm{elyt,an}}(y)\ . \tag{2.10}$$

Consequently, additional expressions are needed to close Eqs. 2.8 that describe the variation of $\Delta\phi_{\mathrm{ca}}$, $\Delta\phi_{\mathrm{an}}$ and ϕ_{elyt} over the thickness of the fuel cell. The current density i is the sum of the Faradaic current $i_{\mathrm{F}}^{\mathrm{V}}$ resulting from electrochemical charge-transfer processes (see 2.2.3) and the electrical current i_{el} resulting from the electronic conductivity of the electrolyte (see 2.3.4):

$$i = \int_{y=0}^{L_{\mathrm{E}}} i_{\mathrm{F}}^{\mathrm{V}}\,\mathrm{d}y + i_{\mathrm{el}} \quad . \tag{2.11}$$

The charge-transfer reactions are possible over the whole thickness of the porous electrode and we integrate the volumetric current density $i_{\mathrm{F}}^{\mathrm{V}}$ over the electrode thickness L_{E} to get the current density i with respect to the cell surface.

Model anode. In the reference electrode setup (Fig. 2.1 a) the overpotential $\eta(i)$,

$$\eta(i) = \phi_{\mathrm{elde,work}}(i) - \phi_{\mathrm{elde,ref}} \quad - iR_{\mathrm{elyt}}, \tag{2.12}$$

given by the difference between the potentials of the working electrode ($\phi_{\mathrm{elde,work}}(i)$) and the reference electrode ($\phi_{\mathrm{elde,ref}}$), is measured in relation to the current density i between working and counter electrode. The potential steps at the electrodes are given by

$$\Delta\phi_{\mathrm{elde,work}} = \phi_{\mathrm{elde,work}} - \phi_{\mathrm{elyt,work}} \quad \text{and} \quad \Delta\phi_{\mathrm{elde,ref}} = \phi_{\mathrm{elde,ref}} - \phi_{\mathrm{elyt,ref}}\ . \tag{2.13}$$

If the reference electrode is placed correctly and sees a constant gas atmosphere, it represents the potential at the center of the electrolyte and is independent of the current density i [31, 32].

2.2 Elementary kinetics

In this section the model equations describing the kinetics of a general electrochemical reaction,

$$\sum_{i \in R_\mathrm{f}} \nu_i^{'} A_i^{'} + z\mathrm{e}^- \rightleftharpoons \sum_{j \in R_\mathrm{r}} \nu_j^{''} A_j^{''} \tag{2.14}$$

are summarised. The Eq. 2.14 describes the reaction between the products $A^{''}$ and the reactants $A^{'}$ with stoichiometric coefficients $\nu^{''}$ and $\nu^{'}$. The reaction is formulated in the direction of reduction, where z denotes the number of electrons transferred. In this thesis the reaction is assumed to proceed at the interface of a solid electrolyte and a solid electrode. The reaction proceeds until thermodynamical equilibrium is reached. However, as charge is transported in the course of the reaction, an electrical potential difference

$$\Delta\phi = \phi_\mathrm{elde} - \phi_\mathrm{elyt} \tag{2.15}$$

develops between the electrolyte and the electrode. The kinetics of the reaction described by Eq. 2.14 is characterised by the forward and reverse reaction rates $k_\mathrm{r/f}$ derived from transition-state theory [30]:

$$k_\mathrm{f} = k_\mathrm{f}^0 \exp\left(-\frac{E_\mathrm{f}^\mathrm{act}}{RT}\right) \exp\left(-\left(1-\alpha\right)\frac{zF}{RT}\cdot\Delta\phi\right) \quad , \tag{2.16}$$

$$k_\mathrm{r} = k_\mathrm{r}^0 \exp\left(-\frac{E_\mathrm{r}^\mathrm{act}}{RT}\right) \exp\left(\alpha\frac{zF}{RT}\cdot\Delta\phi\right) \quad . \tag{2.17}$$

where E^act are the activation energies, α the symmetry factor and F, R, T respectively are Faraday's constant, ideal-gas constant and temperature. According to mass-action kinetics the net change of species i due to an electrochemical reaction is given by the rate $\dot{s}_i$ [7]:

$$\dot{s}_i = \nu_i \left(k_\mathrm{f} \prod_{j \in R_\mathrm{f},} A_j^{\nu_j^{'}} - k_\mathrm{r} \prod_{j \in R_\mathrm{r},} A_j^{\nu_j^{''}} \right) \ , \tag{2.18}$$

where $\dot{s}_i$ and A_i can be given as volumetric or area specific quantities. If a charged species participates in the reaction, the rate $\dot{s}_i$ gives rise to an electrical current density

$$j_i = zF\dot{s}_i \ . \tag{2.19}$$

2.2.1 Gas-phase chemistry

The fuel and product species in an SOFC system are supplied by gas channels. The species in the bulk gas phases may undergo chemical reactions if the gas mixture is not in thermodynamical equilibrium. For the reactions in the gas phase the Eqs. 2.16-2.18 hold. However, all gas-phase species share the same phase and the same electrical potential resulting in $\Delta\phi = 0$. Consequently, at thermodynamical equilibrium, where the net rate $\dot{s}_i$ of all species must be zero the free Enthalpy of reaction ΔG must vanishes,

$$\Delta G = \Delta H - T\Delta S \equiv 0 \,. \tag{2.20}$$

Here ΔH and ΔS, respectively, are the enthalpy and entropy derived from the molar quantities of the species:

$$\Delta H = \sum_{i \in R_\mathrm{f}} \nu_i'' h_i - \sum_{i \in R_\mathrm{r}} \nu_i' h_i \quad , \tag{2.21}$$

$$\Delta S = \sum_{i \in R_\mathrm{f}} \nu_i'' s_i - \sum_{i \in R_\mathrm{r}} \nu_i' s_i \quad . \tag{2.22}$$

The pre-exponential factors k^0 as well as the activation energies E^act of the forward and reverse reaction rates in Eq. 2.16 and Eq. 2.17 are not independent but related via the equilibrium relation (Eq. 2.20) [4]:

$$E_\mathrm{f}^\mathrm{act} - E_\mathrm{r}^\mathrm{act} = \Delta H \quad , \tag{2.23}$$

$$\frac{k_\mathrm{f}^0}{k_\mathrm{r}^0} = \exp\left(\frac{\Delta S}{R}\right) \quad . \tag{2.24}$$

The gas mixture will be described in terms of the mass density ρ, the total concentration $c_\mathrm{tot} = \sum_i c_i$ and the mean molar mass $\bar{M} = {}^1\!/_{c_\mathrm{tot}} \sum_i c_i M_i$. The quantity of species will be given either in molar concentrations c_i, mole fractions $X_i = {}^{c_i}\!/_{c_\mathrm{tot}}$ or mass fractions $Y_i = {}^{M_i}\!/_{\bar{M}} X_i$, where M_i represents the molar mass of species i. The assumption of an ideal gas is assumed to hold throughout this thesis:

$$\rho = \frac{p\bar{M}}{RT} \,, \tag{2.25}$$

where p is the pressure, R the gas constant and T the temperature of the mixture. The volumetric source terms of the gas-phase species $\dot{s}_i^\mathrm{V}$ are calculated applying mass-action kinetics (Eq. 2.18) using the software package DETCHEM [33].

2.2.2 Surface chemistry

The surface chemistry is treated in analogy to the gas-phase chemistry. We make use of the mean-field approximation (i.e. we assume that the state of a surface adsorbed species can be described by averaged surface coverages, thermodynamic and kinetic parameters). The detailed structures of the surface (steps, kinks, crystal disorders) are assumed to be included in these quantities. Wherever appropriate, the area-specific molar surface concentrations c_i are normalised to the total of available surface sites Γ_k yielding the dimensionless surface coverage

$$\theta_i = \frac{c_i \cdot \sigma_i}{\Gamma_k} \ , \tag{2.26}$$

where σ_i is the number of surface sites a species occupies. The coverages of surface species is coupled to the concentration of gas-phase species by heterogeneous chemistry. We assume a Langmuir-Hinshelwood reaction pathway. The species production rate of a species i is calculated via mass-action kinetics (Eq. 2.18) yielding the area-specific production rate $\dot{s}_i^{\mathrm{A}}$ which can be converted into the change of surface coverage using Eq. 2.26.

2.2.3 Charge transfer

Calculating the current resulting from the charge transfer (CT) via electrochemical reactions may be realised with different approaches. In a global view Butler-Volmer kinetics may be used. A second possibility, combining the low computational costs of the global approach with basic elementary kinetics was published by Goodwin, Kee and co-workers [34–36]. Thirdly, the current can be directly calculated from the kinetics of the elementary charge-transfer reaction. Throughout this thesis the latter approach will be used exclusively for the SOFC anode, because it allows to account for the coupling between the various processes governing SOFC operation without any *a priory* assumptions on rate-limiting steps. The approach may be used for any number and any kind of charge-transfer processes including 1D line-specific surface-spillover reactions as well as charge transfer over a 2D interface between bulk materials and it holds under non-equilibrium conditions. For modelling the cathode electrochemistry a modified Butler-Volmer approach will be used to save computation time in Ch. 4.

Global Butler-Volmer kinetics. Using global reaction kinetics, Butler-Volmer expressions are used frequently to relate the current density i to the activation overpotential of the electrode η_{act} [7, 30]:

$$i = i^0 \left[\exp\left(\beta_{\mathrm{a}} \frac{F}{RT} \eta_{\mathrm{act}} \right) - \exp\left(-\beta_{\mathrm{c}} \frac{F}{RT} \eta_{\mathrm{act}} \right) \right] \ , \tag{2.27}$$

where i^0 is the exchange current density and β_a and β_c are the symmetry factors for the anodic and cathode reaction, respectively. For a symmetrical electron transfer of one electron, β_a=β_c =0.5. The dependence of the current density on experimental conditions such as pressure and composition of the gas phase is included via the exchange current density. Elementary charge-transfer reactions are not resolved.

Modified Butler-Volmer kinetics. To reduce the empiricism included in the Butler-Volmer description, Goodwin, Kee and co-workers [34, 35] formulated analytical expressions for the exchange current densities of the hydrogen oxidation reaction (Eq. 2.3),

$$i^0_{\mathrm{an}} = i^*_{\mathrm{an}} \exp\left(-\frac{E^{\mathrm{act}}_{\mathrm{an}}}{RT}\right)\left(\frac{p^{\mathrm{an}}_{\mathrm{H_2}}}{p^*_{\mathrm{H_2}}}\right)^{1/4}\left(\frac{p^{\mathrm{an}}_{\mathrm{H_2O}}}{101325\ \mathrm{Pa}}\right)^{3/4}\left(1+\frac{p^{\mathrm{an}}_{\mathrm{H_2}}}{p^*_{\mathrm{H_2}}}\right)^{-1/2} \quad , \quad (2.28)$$

with $\beta_a = 1.5$ and $\beta_c = 0.5$ and the oxygen reduction reaction (Eq. 2.4),

$$i^0_{\mathrm{ca}} = i^*_{\mathrm{ca}} \exp\left(-\frac{E^{\mathrm{act}}_{\mathrm{cath}}}{RT}\right)\left(\frac{p^{\mathrm{ca}}_{\mathrm{O_2}}}{p^*_{\mathrm{O_2}}}\right)^{1/4}\left(1+\frac{p^{\mathrm{ca}}_{\mathrm{O_2}}}{p^*_{\mathrm{O_2}}}\right)^{-1/2} \quad , \quad (2.29)$$

with $\beta_a = 0.5$ and $\beta_c = 0.5$. Here, i^* are the preexponential factors and p^* are nonlinear functions of partial pressure given in [35]. To derive the analytical expression for the exchange current densities they assumed that one specific CT reaction is the only rate-limiting process. In this picture, the surface is always in equilibrium with the gas phase. This allowed to include basic elementary kinetics into the global Butler-Volmer approach but inherently assumes fast heterogeneous chemistry and fast mass transport on the surfaces.

Elementary kinetics. In contrast to the two approaches presented so far, we will not assume any specific rate-limiting processes. As the charge transfer in an SOFC inherently involves the transition from electronic conduction of the electrical current in the electrode to ionic conduction in the electrolyte, all CT reactions in this thesis are assumed to proceed over the interface between electrode and electrolyte. This interface may be either a line, formed by the intersection of the three phases gas/electrode/electrolyte (three phase boundary, TPB), or the contact area of the bulk electrode and the bulk electrolyte. The CT reaction proceeds over the whole length of this interface, consequently, the total current generated by a CT reaction depends on the absolute dimensions of the interface. The length of this interface, l_{TPB}, is given either as an area-specific quantity ($l^{\mathrm{A}}_{\mathrm{TPB}}$) for the studies on the elementary kinetics of charge-transfer in Ch. 3, or as volume-specific quantity ($l^{\mathrm{V}}_{\mathrm{TPB}}$) in Ch. 4 where porous electrodes are modelled. The Faradaic current density i_{F} of one CT reaction with respect to the surface area of the whole cell is

given by

$$i_{\mathrm{F,ct}} = zFl_{\mathrm{TPB}} \left(k_{\mathrm{f,ct}} \prod_{j \in \mathrm{R_{ct}}} A_j^{\nu_j'} - k_{\mathrm{r,ct}} \prod_{j \in \mathrm{P_{ct}}} A_j^{\nu_j''} \right) . \tag{2.30}$$

If more than one electrochemical reaction takes place, the overall current density i_{F} is the sum over all CT reactions:

$$i_{\mathrm{F}} = \sum_{\mathrm{all\,CTRs}} i_{\mathrm{F,ct}} . \tag{2.31}$$

The advantages of modelling the charge-transfer in SOFC using a detailed elementary kinetic approach over the widely used description via Butler-Volmer-type kinetics are:

- The potential difference entering the rate equations (Eq. 2.17 and Eq. 2.16) are "real" physical potential steps due to the formation of electrical double layers at the interfaces of the electrodes with the electrolyte.
- The description of charge transfer using elementary kinetics allows to resolve the full kinetic coupling of all processes governing fuel cell performance.
- There is no need for an *a priori* assumption of an rate-determining step. In contrast, this approach allows to identify the relevance of individual processes.
- The model is applicable in non-equilibrated conditions.
- The open-circuit voltage is not an input into the model but a model prediction.

2.3 Multi-scale transport

2.3.1 General conservation principles

The quantity F of an extensive variable within an control volume V follows from the integration over its density in V [37],

$$F(t) = \int_V f(\vec{x}, t)\, \mathrm{d}V \quad . \tag{2.32}$$

Temporal changes of this variable $F(t)$ may be introduced by flux $\vec{J}_f(\vec{x},t)$ over the surface ∂V into the control volume (e.g., electrical current, diffusion or convection), by source terms within the volume (e.g., resulting from chemical reactions $q_f(\vec{x},t)$) or via interaction with external fields s_f (e.g., heat radiation or gravitation). For a differential area element $\mathrm{d}A$ or volume element $\mathrm{d}V$ these contributions can be calculated by

$$\vec{J}_f\,\vec{n}\,\mathrm{d}A\;, \quad q_f\,\mathrm{d}V\;, \text{ and } \quad s_f\,\mathrm{d}V \quad . \tag{2.33}$$

Here, $\vec{n}$ denotes the vector normal to $\mathrm{d}A$ facing outwards. From the conservation of the extensive variable F it follows that

$$\frac{\partial F}{\partial t} = -\int_{\partial V} \vec{J}_f\,\vec{n}\,\mathrm{d}A + \int_V q_f \mathrm{d}V + \int_V s_f \mathrm{d}V\,. \tag{2.34}$$

Combining this equation with the time derivative of Eq. 2.32,

$$\frac{\partial F}{\partial t} = \int_V \frac{\partial f}{\partial t}\mathrm{d}V \tag{2.35}$$

and applying Gauß' divergence theorem [38] on the flux through the surface ∂V of V, the continuity equation is derived

$$\frac{\partial f(\vec{x},t)}{\partial t} = -\mathrm{div}\vec{J}_f(\vec{x},t) + q_f(\vec{x},t) + s_f(\vec{x},t)\;. \tag{2.36}$$

2.3.2 Homogenisation approach

For the porous structure of the composite electrodes consisting of three phases (pore space, metal electrode and ceramic electrolyte) a homogenisation approach will be used [39–41]. In this approach the microstructure is not spatially resolved; its influence on the macroscopic description is accounted for using effective transport coefficients.

2.3.3 Charge transport

Porous SOFC electrodes typically are composite materials comprising of gas-filled pores, an electronically conducting electrode phase and an ionically conduction electrolyte phase. Typical material systems are Ni/YSZ for the anode and LSM/YSZ for the cathode. The electronic conductivity of the electrode phase is several orders of magnitude higher than the ionic conductivity of the electrolyte phase. Therefore a potential gradient in the electrode phase does not occur,

$$\frac{\partial \phi_{\mathrm{elde}}}{\partial y} = 0\;. \tag{2.37}$$

In the electrolyte phase, the local current density i_{elyt} follows Ohm's law,

$$i_{\mathrm{elyt}} = -\sigma_{\mathrm{elyt}}^{\mathrm{eff}} \frac{\partial}{\partial y}\phi_{\mathrm{elyt}} = -\sigma_{\mathrm{elyt}} f_\sigma \frac{\partial}{\partial y}\phi_{\mathrm{elyt}} \ , \tag{2.38}$$

where ϕ_{elyt} is the electrical potential and $\sigma_{\mathrm{elyt}}^{\mathrm{eff}} = \sigma_{\mathrm{elyt}} f_\sigma$ is the effective ionic conductivity. In analogy to the effective diffusion coefficient in the porous medium, the effective conductivity is calculated from conductivity σ_{elyt} and a geometrical effectiveness factor $f_\sigma \approx \epsilon/\tau$. Where the electrolyte and electrode phase are in contact, the currents in the two phases are coupled by electrochemical reactions. The Faradaic current density i_{F}, following from Eq. 2.31, represents a source term for the ionic current. The first spatial derivative of the ionic current follows from the continuity equation (Eq. 2.36):

$$\frac{\partial i_{\mathrm{elyt}}}{\partial y} = i_{\mathrm{F}} \ . \tag{2.39}$$

A combination of the above equations yields the expression for the spatial distribution of the potential step $\Delta\phi = \phi_{\mathrm{elde}} - \phi_{\mathrm{elyt}}$ in the composite electrode,

$$\frac{\partial}{\partial y}\left(\sigma_{\mathrm{elyt}} f_\sigma \frac{\partial}{\partial y}\Delta\phi_{\mathrm{an}}\right) = -i_{\mathrm{F}} \ . \tag{2.40}$$

This equation is solved for the anode and the cathode.

Within the dense electrolyte no sources or sinks for electrical charges are present and the continuity equation takes the homogeneous form,

$$\frac{\partial}{\partial y}\left(\sigma_{\mathrm{elyt}} \frac{\partial}{\partial y}\phi_{\mathrm{elyt}}\right) = 0 \ . \tag{2.41}$$

The conductivity of the electrolyte is assumed temperature dependent [42–44] according to:

$$\sigma_{\mathrm{elyt}} = \frac{A_\sigma}{T} \cdot \exp\left(-\frac{E_\sigma}{RT}\right) \ , \tag{2.42}$$

where A_σ and E_σ are the pre-exponential factor and the activation energy for the ionic conductivity.

Boundary conditions. At the interface of the porous electrode with the dense electrolyte, charge transport occurs purely ionic. As the conductivities of the electrolyte phase in composite electrode and the dense electrolyte layer differ by the effectiveness factor f_σ, a step in the gradient of the electrical potential develops,

$$\frac{\partial}{\partial y}\phi_{\mathrm{elyt}}(\mathrm{dense}) = f_\sigma \frac{\partial}{\partial y}\phi_{\mathrm{elyt}}(\mathrm{porous}) \ , \tag{2.43}$$

whereas the potential itself is continuous,

$$\phi_{\text{elyt}}(\text{dense}) = \phi_{\text{elyt}}(\text{porous}) \ . \tag{2.44}$$

When simulating reference electrode setups, only the working electrode is taken into account. The electrolyte potential of the reference electrode is set to the potential at the center of the electrolyte. Consequently, the difference in electrical potential of working electrode and reference electrode can be given as the overpotential,

$$\eta = \phi_{\text{elde,ref}} = \phi_{\text{elde,work}} \ . \tag{2.45}$$

The absolute potential is defined by choosing an arbitrary reference point. We choose the cathode as reference point for simulations of full SOFCs and the center of the electrolyte layer as reference point for simulations of reference electrode setups. In both cases the reference is set to zero for convenience:

$$\phi_{\text{elyt,center}} = 0 \ , \ \phi_{\text{ca}} = 0. \tag{2.46}$$

2.3.4 Mixed ionic and electronic conductors (MIEC)

In composite materials used for electrode design in SOFCs (e.g., Ni/YSZ) the conduction of the charge carriers occurs within two separate phases, they are heterogeneous mixed conductors (H-MIEC). In mixed ionic and electronic conducting materials (MIEC) such as GDC (gadolinia-doped ceria) or SDC (samaria-doped ceria) ionic and electronic charge carriers are transported within one single phase. The advantages of such materials are

- The ionic conductivity can be about one order of magnitude larger than for conventional materials such as YSZ [45]. This would allow to reduce operating temperature without loss of performance.
- They would allow to spread the electrochemically active regions over the whole electrode surface. As MIEC may as well act as catalysts for electrochemical reactions, simultaneously transporting electrons and ions, electrochemical reactions are not restricted to the interface of electronically and ionically conducting phases, but can take place on the whole surface.

There is also a drawback assigned to using MIEC as solid electrolytes. As the MIEC exhibit electronic conductivity, current may pass from the anode to the cathode through the dense electrolyte, thereby "short-circuiting" the SOFC and reducing the performance. However, as the electronic conductivity of MIECs depend nonlinearly on the partial pressure of oxygen [15, 45] the conductivity at the cathode is low due to the high $p\mathrm{O}_2$, whereas at the anode the low $p\mathrm{O}_2$ allows for higher electronic conductivity. To account for the

electronic conductivity of the MIEC used in the study of the DFFC in Ch. 4 we use the expression

$$i_{\mathrm{el}} = -i_{\mathrm{elyt}} \frac{\sigma^{\mathrm{e}}_{\mathrm{elyt}}(p^{\mathrm{ca}}_{\mathrm{O_2}}, T)}{\sigma^{\mathrm{i}}_{\mathrm{elyt}}(T)} \exp\left(\frac{\eta_{\mathrm{ca}} F}{RT}\right) \cdot \frac{\exp\left(EF/RT\right) - 1}{1 - \exp\left(\left(-i_{\mathrm{elyt}} L_{\mathrm{elyt}} F\right)/\left(RT\sigma^{\mathrm{i}}_{\mathrm{elyt}}\right)\right)} \quad (2.47)$$

developed by Hao and Goodwin [46, 47] based on a model by Riess [45]. Here i_{el} is the electric current that enters the cell level model via Eq. 2.11, i_{elyt} the ionic current density in the electrolyte, $\sigma^{i}_{\mathrm{elyt}}$ and $\sigma^{\mathrm{e}}_{\mathrm{elyt}}$ the ionic and electronic conductivity of the MIEC, η_{ca} the overpotential of the cathode, E the cell voltage and L_{elyt} the thickness of the electrolyte. The ionic conductivity is temperature dependent as given by Eq. 2.42 and the electronic conductivity depends on the partial pressure of oxygen at the cathode $p^{\mathrm{ca}}_{\mathrm{O_2}}$ as well as on temperature following

$$\sigma^{\mathrm{e}}_{\mathrm{elyt}}(p^{\mathrm{cath}}_{\mathrm{O_2}}, T) = \left(\frac{p^{\mathrm{cath}}_{\mathrm{O_2}}}{p^0}\right)^{-1/4} \cdot \frac{a^{\mathrm{elyt}}_0}{T} \cdot \exp\left(\frac{b^{\mathrm{elyt}}_0}{T}\right) . \quad (2.48)$$

2.3.5 Heat transport

Within the membrane electrode assembly (MEA), heat transport is dominated by heat conduction in the solid phases,

$$\frac{\partial\left(\rho c_{\mathrm{P}} T\right)}{\partial t} = \frac{\partial}{\partial y}\left(\lambda_{\mathrm{q}} \frac{\partial T}{\partial y}\right) + \dot{s_{\mathrm{q}}} , \quad (2.49)$$

where c_{P} is the heat capacity, T the temperature, ρ the density of the electrolyte or the electrode, λ_{q} the heat conductivity and $\dot{s_q}$ an additional source term including the heat sources or sinks due to chemical reactions (electrochemistry, surface and gas-phase chemistry) and ohmic heating (Joule heating) resulting from the resistances in the electrolyte,

$$\dot{s_q} = \underbrace{\sigma^{i}_{\mathrm{elyt}} \left(\frac{\partial \phi_{\mathrm{elyt}}}{\partial y}\right)^2}_{\dot{s_{\mathrm{q}}}^{\mathrm{Joule}}} + \underbrace{\sum_{i \in S_{\mathrm{g}}, S_{\mathrm{s}}} \dot{s}^{V}_{i} h_i}_{\dot{s_{\mathrm{q}}}^{\mathrm{chem}}} . \quad (2.50)$$

Boundary conditions. The surfaces of the electrodes (anode and cathode) are in direct thermal contact with the gas phase. Depending on the cell configuration, different boundary conditions apply:

- For model anodes studies, experiments are typically performed inside a furnace where gas phase and fuel cell are forced on the same constant temperature level. For this setup isothermal conditions are assumed,

$$T_{\mathrm{ca}} = T_{\mathrm{an}} = T_{\mathrm{fluid}} . \quad (2.51)$$

- For the direct flame fuel cell system, the fuel cell is placed into the exhaust of a flame with the anode facing the flame front. The anode side of this configuration is spatially resolved and the temperature profile has to be continuous at the interface of gas phase and surface,

$$T_{\text{anode}} = T_{\text{gas}} \ . \tag{2.52}$$

From the conservation of energy it follows that the heat fluxes leaving the MEA must be equal to the flux entering the adjacent gas phase. However, the surface additionally exchanges heat with its environment via heat radiation. Using the Stefan-Boltzmann law to describe heat radiation, the boundary condition is

$$j_{\text{q}}^{\text{anode}} = j_{\text{q}}^{\text{gas}} + \sigma_{\text{SB}} \cdot \epsilon_{\text{q}}^{\text{an}} \left(T_{\text{anode}}^4 - T_{\text{ref,an}}^4 \right) \tag{2.53}$$

where σ_{SB} is the Stefan-Boltzmann constant, and $\epsilon_{\text{q}}^{\text{an}}$ the emissivity of the anode. The reference temperature for calculating the heat radiation is the temperature of the burner surface,

$$T_{\text{ref,an}} = T_{\text{burner}} \ . \tag{2.54}$$

On the cathode side, natural convection and heat radiation are accounted for yielding,

$$j_{\text{q}}^{\text{cathode}} = \alpha \left(T_{\text{cathode}} - T_{\text{ref}} \right) + \sigma_{\text{SB}}^{\text{ca}} \cdot \epsilon_{\text{q}}^{\text{ca}} \left(T_{\text{cathode}}^4 - T_{\text{ref}}^4 \right) \ , \tag{2.55}$$

where the natural convection is described via a Nusselt index law,

$$\alpha = Nu \frac{\lambda_{\text{q}}^{\text{gas}}}{L} \ . \tag{2.56}$$

The heat conductivity and the reference temperatures are assumed to correspond to ambient air at $T_{\text{ref}} = 293$ K.

2.3.6 Gas-phase transport

In analogy to 2.3.1 conservation equations can be derived for the extensive variables of the gas phase, mass, species, energy and momentum. These equations, the Navier-Stokes equations, are described in detail in [37, 48–52]. The summary given here follows the nomenclature of Bird et al. [48].

For the mass the continuity equation (Eq. 2.36) leads to the first Navier-Stokes equation:

$$\frac{\partial \rho}{\partial t} = -\text{div} \underbrace{(\rho \vec{v})}_{\vec{J}_f} + \underbrace{S_{\text{m}}}_{q_f} \ . \tag{2.57}$$

Here, ρ is the density, $\vec{v}$ the convective velocity and S_m a species source term resulting from the coupling of gas-phase concentration to surface coverages via ad- and desorption reactions.

In multicomponent mixtures mass conservation is related to species conservation. The mass density ρ_i of species i follows from the multiplication of the molar density of species i with its molecular mass. In analogy to Eq. 2.57 a continuity equation for the species can be formulated,

$$\frac{\partial \rho_i}{\partial t} = -\mathrm{div} \underbrace{\left(\rho_i \vec{v} + \vec{j}_i^{\mathrm{diff}}\right)}_{\vec{J}_f} + \underbrace{S_i}_{q_f} \,. \tag{2.58}$$

In addition to the purely convective flux in Eq. 2.57 a diffusive flux $\vec{j}_i^{\mathrm{diff}}$ appears, accounting for the movement due to gradients in concentration and temperature. The sum over all species conservation equations must be equal to Eq. 2.57 thus, the fluxes $\vec{j}_i^{\mathrm{diff}}$ have to sum up to zero. The chemical source term S_i includes the ad- and desorption reactions from the surface and the species conversion by the homogeneous gas-phase reactions.

In Newtonian fluids the conservation of momentum is described the second Navier-Stokes equation,

$$\frac{\partial \left(\rho \vec{v}\right)}{\partial t} = \underbrace{-\left[\vec{\nabla} \cdot \rho \vec{v} \vec{v}\right] - \mathrm{grad}\, p - \left[\vec{\nabla} \cdot \overline{\tau}\right]}_{-\mathrm{div} \vec{J}_f} + \underbrace{\rho \vec{g}}_{s_f} \quad . \tag{2.59}$$

The divergence of the flux $\vec{J}_f$ (Eq. 2.36) comprises three parts: The term $\left[\vec{\nabla} \cdot \rho \vec{v} \vec{v}\right]$ is the divergence of the dyadic product $\rho \vec{v} \vec{v}$. It describes the convective transport of momentum. The gradient in the hydrostatic pressure p and the divergence of the stress tensor $\overline{\tau}$ due to viscous transport describe the effect of the molecular transport on the momentum balance. The influence of gravity is accounted for by the term $\rho \vec{g}$.

The principle of energy conversion leads to another continuity equation which is given here in terms of the specific enthalpy h:

$$\frac{\partial \left(\rho h\right)}{\partial t} = -\left[\vec{\nabla} \cdot \rho \vec{v} h\right] - \left[\vec{\nabla} \cdot \vec{j_\mathrm{q}}\right] - \left[\overline{\tau} \vec{\nabla} \cdot \vec{v}\right] + \frac{\partial p}{\partial t} + \left[\vec{v} \cdot \mathrm{grad}\, p\right] + S_\mathrm{q} \,, \tag{2.60}$$

where $\vec{j_\mathrm{p}}$ describes heat transport due to heat conduction (Fourier's law), mass diffusion and concentration gradients (Dufour effect). The source term S_q includes thermal radiation and thermal conduction at the interfaces of bulk gas-phase and pore-space.

The equation system (Eqs. 2.57-2.59) describes the gas phase based on the state variables of pressure, temperature and density (p, T and ρ). Assuming

an ideal gas, the equation system can be closed using the state equation,

$$p\overline{M} = \rho RT \quad . \tag{2.61}$$

Where the the mean molar mass $\overline{M}$ is calculated from

$$\frac{1}{\overline{M}} = \sum_{i \in S_g} \frac{Y_i}{M_i} \quad . \tag{2.62}$$

Here S_g represents all species present in the gas phase, M_i is the molar mass of species i and Y_i the mass fraction.

Transport coefficients. In the following, we describe diffusive mass and heat transport for a one-dimensional case only. We distinguish three cases described in more detail in [48, 49, 51, 53]:

1. Fickian diffusion will be used for binary mixtures,

$$j_1^{\text{diff}} = -\rho D_{12} \frac{\partial Y_1}{\partial x} \quad \text{and} \quad j_2^{\text{diff}} = -\rho D_{21} \frac{\partial Y_2}{\partial x} \quad . \tag{2.63}$$

2. An analytical solution of the Stefan-Maxwell equations will be used for ternary mixtures,

$$\frac{\partial c_i}{\partial x} = \sum_{j \in S_g} \frac{X_i J_j^{\text{diff}} - X_j J_i^{\text{diff}}}{D_{ij}} \quad . \tag{2.64}$$

3. For multicomponent mixtures we will apply [49],

$$j_i^{\text{diff}} = -\rho \frac{Y_i}{X_i} \overline{D}_i \frac{\partial X_i}{\partial x} \tag{2.65}$$

   using mixture-averaged individual diffusion coefficients $\overline{D}_i$ calculated via

$$\overline{D}_i = \frac{1 - Y_i}{\sum_{j \in S_g, j \neq i} X_j / D_{ij}} \quad . \tag{2.66}$$

Here D_{ij} is the binary diffusion coefficient of the species i and j calculated from the reduced molecular masses, collision diameters and the collision integral of the colliding molecules [49]. This results in a symmetry of the diffusion coefficients $D_{ij} = D_{ji}$. The concentration of species i enters the Eqs. 2.63-2.65 in terms of molar concentrations c_i and in terms of mole and mass fractions X_i and Y_i. Consequently the diffusive fluxes are given as mass fluxes j_i^{diff} or

molar fluxes J_i^{diff}. The conversion between mass and molar fluxes is given by:

$$j_i^{\text{diff}} = M_i \, J_i^{\text{diff}} \quad \text{und} \quad X_i = Y_i \frac{\overline{M}}{M_i} \quad . \tag{2.67}$$

The convective velocity of a control volume is given with respect to its center of mass. This implies, that all diffusive mass fluxes have to sum-up to zero

$$\sum_{i \in S_{\text{g}}} j_i^{\text{diff}} = 0 \quad . \tag{2.68}$$

This inherently holds for the description of binary and ternary mixtures (Eqs. 2.63 and 2.64) whereas for the third approach the following correction is used to enforce the condition given by Eq. 2.68

$$j_i^{\text{diff, corr}} = j_i^{\text{diff}} - Y_i \sum_{j \in S_{\text{g}}} j_j^{\text{diff}} \, . \tag{2.69}$$

The transport of heat within a control volume consists of three parts: Heat convection (Fourier's law), diffusive heat transport and heat transport due to concentration gradients (Dufour effect) [54]. Assuming that the Dufour effect is negligible, the heat flux j_{q} is the sum of heat conduction and enthalpy transport:

$$j_{\text{q}} = -\lambda \frac{\partial T}{\partial x} + \sum_{i \in S_{\text{g}}} h_i j_i^{\text{diff}} \tag{2.70}$$

The transport coefficients of a gas mixture are calculated from the the species' individual properties for thermal conductivity λ_i,

$$\lambda = \frac{1}{2} \left[\sum_{i \in S_{\text{g}}} X_i \lambda_i + \left(\sum_{i \in S_{\text{g}}} \frac{X_i}{\lambda_i} \right)^{-1} \right] \quad , \tag{2.71}$$

and viscosity μ_i,

$$\mu = \frac{1}{2} \left[\sum_{i \in S_{\text{g}}} X_i \mu_i + \left(\sum_{i \in S_{\text{g}}} \frac{X_i}{\mu_i} \right)^{-1} \right] \quad . \tag{2.72}$$

The viscosity determines shear stress at the limiting walls in the one-dimensional representation of the conservation equation and therefore the shear tensor in Eq. 2.59. For the numerical solution of the transport equations, the values of the species' enthalpy, thermal conductivity and viscosity, as well as the binary diffusion coefficients are calculated either using the simulation software DETCHEM by Deutschmann et al. [33, 55], or using the relations

and coefficients given by Todd et al. [56].

2.3.7 Stagnation-point flow

The basic equations governing fluid flow, the Navier-Stokes equations, form a system of nonlinear partial differential equations. Although today it is possible to numerically calculate solutions to the general Navier-Stokes equations, it is computationally expensive and for large Reynolds numbers this task becomes more and more complex. For special cases exact solutions to the Navier-Stokes equations exist. The stagnation-point flow is such an exact solution for an incompressible viscous flow of large Reynolds numbers onto an infinitely spreading plane. In the stagnation-point flow the Navier-Stokes equations (Eqs. 2.57-2.60) can be formulated in one dimension because of the radial-symmetric problem. Using the axial mass flow density ρv_y, the scaled radial velocity $V = {}^{v_\mathrm{r}}/_{r}$, the mass fraction Y_i and the radial pressure gradient $\Lambda = {}^{1}/_{r} \cdot ({}^{\mathrm{d}p}/_{\mathrm{d}r})$ as dependent variables, the equation system describing the stagnation-point flow reads [49]:

$$\frac{\partial \rho}{\partial t} = -\frac{\partial (\rho v_y)}{\partial y} - 2\rho V \tag{2.73}$$

$$\frac{\partial (\rho V)}{\partial t} = -\frac{\partial (\rho v_y V)}{\partial y} - \frac{\partial}{\partial y}\left(\mu \frac{\partial V}{\partial y}\right) - \rho V^2 - \Lambda \tag{2.74}$$

$$\frac{\partial (\rho Y_i)}{\partial t} = -\frac{\partial (\rho v_y Y_i)}{\partial y} - \frac{\partial j_i^{\mathrm{diff}}}{\partial y} + \dot{s}_i^V M_i \tag{2.75}$$

$$\begin{aligned}\frac{\partial (\rho c_\mathrm{P} T)}{\partial t} = &-\frac{\partial (\rho v_y c_\mathrm{P} T)}{\partial y} + \frac{\partial}{\partial y}\left(\lambda_\mathrm{q} \frac{\partial T}{\partial y}\right) \\ &-\sum_{i \in S_\mathrm{g}} c_{\mathrm{P},i} j_i^{\mathrm{diff}} \frac{\partial T}{\partial y} - \sum_{i \in S_\mathrm{g}} \dot{s}_i^V h_i \quad .\end{aligned} \tag{2.76}$$

Boundary conditions. At the inflow, the mass-flow density and the temperature are given by the inlet conditions ($\rho_\mathrm{in} v_\mathrm{in}$ and T_in). The gas concentrations are corrected for back-diffusion from the flow field, following from mass conservation [57]. At the fuel cell the axial velocity is given by the so-called Stefan velocity [49],

$$v^{\mathrm{Stef}} = \frac{1}{\rho} \sum_i M_i \dot{s}_i{}^{\mathrm{A}} \ , \tag{2.77}$$

which is non-zero if there is mass exchange between the gas and the surface. The radial velocity is zero at fuel cell surface (stagnation point) and the temperature boundary condition at the fuel cell follows from heat exchange with the porous electrode.

2.3.8 Mass transport in the porous electrodes

Gas transport in the porous electrodes is modelled by coupled diffusion and viscous flow. The continuity equation (Eq. 2.57) can then be formulated as

$$\frac{\partial\ (\varepsilon c_i)}{\partial t} = -\frac{\partial J_i^{\text{diff}}}{\partial y} - \frac{\partial J_i^{\text{flow}}}{\partial y} + \dot{s}_i^{\text{V}}\ . \tag{2.78}$$

Here J_i^{diff} is the diffusive flux of species i in the multi-component mixture, J_i^{flow} is the viscous flow of species i, according to Darcy's law, $\dot{s}_i^{\text{V}}$ denotes the volumetric production rate resulting from ad- and desorption reactions and ε is the porosity of the electrode. The source term $\dot{s}_i^{\text{V}}$ is calculated from the area-specific production rate $\dot{s}_i^k$ and the volumetric surface area A_k^{V}

$$\dot{s}_i^{\text{V}} = \sum_{k \in S_{\text{k}}} A_k^{\text{V}} \dot{s}_i^k \quad . \tag{2.79}$$

where the sum runs over all surfaces in contact to the gas phase.

The diffusive flux of the species is calculated using the appropriate expressions (Eq. 2.63-2.65). In difference to the diffusion in the bulk gas phase, an additional transport pathway (Knudsen diffusion) may occur in the pore space when the pore radii get in the range of the free length of path. To account for both, free molecular diffusion and Knudsen diffusion, the Bosanquet relation [53] is used for the calculation of the individual diffusion coefficients. To avoid violation of the species conservation principle, the effective diffusion coefficients D_{ij}^{eff} are averaged over the Bosanquet diffusion coefficients of the individual species,

$$D_{ij}^{\text{eff}} = D_{ji}^{\text{eff}} = \frac{\varepsilon}{2\tau^2}\left(\frac{D_i^{\text{K}} D_{ij}}{D_i^{\text{K}} + D_{ij}} + \frac{D_j^{\text{K}} D_{ij}}{D_j^{\text{K}} + D_{ij}}\right) \quad . \tag{2.80}$$

The pre-factor ε/τ^2 accounts for the pore diameter available for the gas transport in the porous media and the increase of path length due to the trailing path. The Knudsen diffusion coefficient D_i^{K} is calculated from the molar mass and the pore radius of the medium r_{P} [53],

$$D_i^{\text{K}} = \frac{2 r_{\text{P}}}{3}\sqrt{\frac{8RT}{\pi M_i}} \quad . \tag{2.81}$$

The pressure-driven flow J_i^{flow} follows from Darcy's law,

$$J_i^{\text{flow}} = -X_i c^{\text{g}} \frac{B}{\mu}\frac{\partial p}{\partial y} \quad , \tag{2.82}$$

where c^{g} is the concentration, μ the mean viscosity and p the pressure. The permeability B of the porous electrode can be derived using the Kozeny-

Carman relation [58, 59],

$$B = \frac{\varepsilon^3 d_{\mathrm{P}}^2}{72\tau^2 \left(1-\varepsilon\right)^2} \quad , \tag{2.83}$$

which includes the average particle diameter d_{P} of the porous medium.

The boundary conditions at the interface of of the porous electrode and the bulk gas phase follow from exchange of species,

$$J_i^{\mathrm{diff}} + J_i^{\mathrm{flow}} = \dot{s}^{\mathrm{gas}} \ , \tag{2.84}$$

as well as the continuity of pressure,

$$p\left(\text{electrode}\right) = p\left(\text{gas}\right). \tag{2.85}$$

At the interface with the solid electrolyte no diffusive flux is possible,

$$J_i^{\mathrm{diff}} = J_i^{\mathrm{flow}} = 0 \quad . \tag{2.86}$$

2.3.9 Mass transport on the surface and in the bulk

Charge transfer is associated with mass transport between the electrolyte and the electrode phase leading to concentration gradients in the vicinity of the electrode/electrolyte interface. The concentration gradients give rise to transport phenomena, in our case to surface and bulk diffusion processes. Diffusion in the bulk lattice structure and the surfaces of electrolyte and electrode are treated using a Fickian approach. Following Fick's first law the flux $\overrightarrow{J}_i$ of a species i is proportional to the gradient in the species' concentration, given here in the dimensionless activity a_i:

$$\overrightarrow{J_i} = -D_i \cdot \overrightarrow{\nabla} \cdot a_i \ , \tag{2.87}$$

where D_i is the diffusion coefficient of species i and the activities a_i are normalised quantities based on the area specific concentration of surface-adsorbed species ($a_i = \theta_i = {}^{\sigma_i}/_{\Gamma_i c_i}$) or on the volume specific concentration of interstitial atoms in the lattice structure of the bulk material ($a_i = {}^{c_i}/_{c_{\mathrm{tot}}}$).

Fick's law was derived for a three-dimensional case. On a surface we have to take into account that the number of adsorption sites is a conserved quantity and therefore, the coverages of all species including the unoccupied surface sites have to sum up to unity:

$$\theta_{\mathrm{tot}} = \sum_{i \in S} \theta_i = 1 \ . \tag{2.88}$$

As a consequence, the flux of species has to be weighted with the available

free sites $\theta_\square$ of so that the flux vanishes in the limit of complete coverage:

$$\overrightarrow{J_i} = -\theta_\square D_i \cdot \overrightarrow{\nabla}\theta_i \ . \tag{2.89}$$

The diffusion on the surfaces are modelled in a one-dimensional representation of Eq. 2.87 whereas the bulk diffusion is modelled in 2D.

Boundary conditions. The diffusion of the surface-adsorbed species or the interstitial species solved in the bulk structure is geometrically limited resulting in Neumann boundary conditions for the governing differential equations,

$$\overrightarrow{\nabla} a_i = 0 \ . \tag{2.90}$$

Diffusion coefficients for surface-adsorbed species. Species subject to surface diffusion are treated within the hard-core lattice gas assumption, sometimes referred to as Langmuir lattice gas. In this context, all species share the same set of adsorption sites and the particles do not interact except for site blocking. We assume that all particles are random walkers, that is, the adsorbates move on the surface by a sequence of spatially and temporally uncorrelated jumps at a frequency ν_{at} from one adsorption site to an unoccupied neighbouring one. For this system the pre-exponential factor of the diffusion coefficient D_i^0 is given by the Einstein-Smoluchowsky relation [60, 61],

$$D_i^0 = \langle x^2 \rangle / 2t = 1/s \cdot \nu_{\mathrm{at}} \cdot l^2 \ , \tag{2.91}$$

where the mean square displacement $\langle x^2 \rangle$ is equal to the square of the lattice constant l^2 if $1/t = \nu_{\mathrm{at}}$. Adsorption sites are local minima in the potential energy hypersurface. For every jump, the adsorbate has to overcome the energy barrier between neighbouring sites. This energy barrier E_i^{act} depends on the bonding strength of the adsorbate to the surface and gives rise to an activated process which we account for by assuming an Arrhenius-type dependence of the surface diffusion coefficient on temperature,

$$D_i = D^0 \cdot \mathrm{e}^{-\frac{E^{\mathrm{act}}}{R \cdot T}} \ . \tag{2.92}$$

Diffusion coefficients for bulk diffusion. Diffusion of the species $\mathrm{H}^{\mathrm{x}}_{\mathrm{iNi}}$ and $\mathrm{H}^{\bullet}_{\mathrm{iYSZ}}$ takes place by interstitial diffusion. The diffusion coefficients are taken from literature and are effective diffusion coefficients representing transport in a non-ideal crystal. The temperature-dependence follows the Arrhenius equation.

2.3.10 Conclusions

In this chapter we presented a modelling framework representing a single cell SOFC system. The model is based on an elementary kinetic description of gas-phase, surface and charge-transfer reactions coupled to transport of mass, heat and charge. The model allows to predict experimentally accessible quantities (cell current and cell voltage) referring to SOFC performance based on physically meaningful parameters only (experimental pressure, temperature, gas composition). The model accounts for the full kinetic coupling of the underlying physico-chemical processes and allows for the identification of rate-limiting steps. The model is not restricted to a special fuel cell setup. In contrary, it will be applied to reference electrode setups, used for investigating fundamental properties of charge-transfer processes as well as for the optimisation of a full SOFC system.

Chapter 3

Ni/YSZ model anode

3.1 Introduction

The traditional Nickel/Yttria-stabilised zirconia (Ni/YSZ) materials system is still widely used today as anode for solid oxide fuel cells (SOFCs) [62]. However, despite the large body of experimental electrochemical data available, the mechanistic details of even the simple hydrogen oxidation reaction are still unclear. This reaction can be formulated globally as

$$H_{2,gas} + O^{X}_{O\,YSZ} \rightleftharpoons H_2O_{gas} + V^{\bullet\bullet}_{O\,YSZ} + 2e^{-}_{Ni} \tag{3.1}$$

where Kröger-Vink notation is used for bulk species. As noted in a recent review article, "Understanding the mechanisms of the surface reactions that occur on the anode near the three-phase boundary is likely to be key to further advances in this area.".

Motivation. It is generally assumed that the electrochemical reaction 3.1 takes place close to the three-phase boundary (TPB) of gas phase, electrode and electrolyte. However, there is quite some controversy as to the actual pathway and nature of the elementary steps [27, 63–65]. Different mechanisms proposed before were recently reviewed [31] (see Fig. 3.1) and are discussed in detail in the following Section.

Experimental characterisation using model electrodes. The use of model electrodes with defined geometry (patterned electrodes, point electrodes) allows the defined characterisation of the three-phase boundary electrochemistry, and is therefore recognised as highly useful for model validation. Studies include patterned anodes [16–19] and point anodes [20, 21]. The main focus in this studies lies on the influence of gas composition and temperature on the polarisation resistance. Here all experiments consistently show

the same trends: A decreasing polarisation resistance with increasing water vapour content and temperature as well as a nearly constant polarisation resistance under variation of the hydrogen content.

Quantitative elementary kinetic modelling approach. Experimental investigations of such a complex reaction system as illustrated in Fig. 3.1 can only be understood with an appropriate theoretical background. In most of the references cited above, the reaction pathways shown in Fig. 3.1 were discussed in *qualitative* terms only, based on chemical intuition and order-of-magnitude estimates. However, for an unambiguous analysis, *quantitative* models are required, allowing to predict macroscopic electrochemical behaviour (polarisation curves, impedance spectra, dependence on gas composition and temperature, surface coverages) that can be compared with experimental data. Only few quantitative studies have been performed to date, and the results have not yet lead to a unique view of the hydrogen oxidation reaction.

There are two challenges in quantitative elementary kinetics: (1) A large number of model parameters (thermodynamic, kinetic and transport coefficients) must be compiled and validated, and (2) the mechanistic complexity requires numerical simulation approaches. In order to circumvent both challenges, a common approach is the *a priori* assumption of one single rate-determining step (usually the charge-transfer reaction, but also surface reactions). This allows the analytical derivation of electrochemical behaviour in dependence of only one or two semiempirical model parameters that can be fitted to experimental data. This kind of analysis has been performed for hydrogen spillover [35, 66, 67], oxygen spillover [68] and interstitial transfer mechanisms [69]. While useful for a qualitative analysis, this approach makes an *a posteriori* validation of the assumptions difficult, unless several possible mechanisms are compared. Assuming the charge-transfer reaction to be the rate-determining step, Bessler et al. have compared five different charge-transfer mechanisms [27]. It was shown that the reaction kinetics strongly depends on the gas-phase composition through a variation of the equilibrium (Nernst) potential. By comparing to experimental patterned anode data at open circuit [16], the hydrogen spillover Reaction H1 was identified as likely rate-determining step. However, it was also pointed out that confirmation of this result through quantitative kinetic modelling was still required.

The first true quantitative elementary kinetic model of the hydrogen oxidation reaction at Ni/YSZ anodes was presented by Bieberle and Gauckler, assuming an oxygen spillover two-electron charge-transfer mechanism (Reaction O5) [70]. Impedance simulations based on state-space modelling were in modest agreement with experimental patterned anode data. The same mechanism was later studied by Bessler using a transient numerical simulation approach [71]. Both studies did not include surface diffusion, and did not resolve surface chemistry on the YSZ surface. Williford and Chick investigated an analogous

mechanism at Pt/YSZ anodes [72, 73]. Considering the full reaction-diffusion system on Pt, they observed electrochemically active TPB widths of several ten nanometres only. Goodwin was the first to quantitatively investigate hydrogen spillover (Reactions H1 and H2) [74], yielding reasonable agreement with experimental polarisation curves by de Boer [18].

Scope of this work. In this work we present a computational model based on elementary physical and chemical processes without the assumption of a rate-determining step. We take into account the heterogeneous chemistry on both, the Nickel and the YSZ surfaces, their coupling via the spillover reactions at the TPB (Fig. 3.1 a-c) or via bulk exchange and the surface transport processes on both surfaces as well as in the bulk material. A database for quantitative modelling of the Ni/YSZ system suitable as general basis for quantitative modelling is compiled. As some parameters (ie. surface diffusion coefficient and YSZ kinetic data) are highly tentative this database must be seen as a first step. The model is validated against experimental pattern anode data from Bieberle et al. [16]. We focus on this data because they represent the most consistent and holistic dataset available. By comparing model and experiment, we identify the processes determining the anode performance and estimate pre-exponential factors and activation energies for the charge-transfer reaction as well as diffusion coefficients for various species on the surfaces of YSZ and Ni. The present study does not include the reactive electrolyte mechanisms (Fig. 3.1 e) which is shown for the sake of completeness only. Although we recognise the importance this mechanism, this must remain subject of future work. The goal is to determine which one, if any, of the spillover reactions is active and can consistently describe the complete experimental data set.

3.2 Elementary charge-transfer reaction

The hydrogen oxidation formulated globally in Eq. 3.1 is generally assumed to occur at or near the three-phase boundary (TPB) of gas phase, electrode and electrolyte. This assumption is based on the respective molecular, electronic and ionic transport properties of the involved phases, where the Ni electrode is a purely electronic conductor and the YSZ electrolyte is essentially a purely ionic conductor. This view is supported by experiments with micro-patterned anodes, where the performance was observed to be proportional to the TPB length [16]. In the following, various reaction pathways proposed previously are briefly summarised. They are illustrated schematically in Fig. 3.1.

(a) *Hydrogen spillover.* At the three-phase boundary line, Ni-adsorbed hydrogen atoms may hop to either a hydroxyl ion (Reaction H1) or an oxygen ion (Reaction H2) on the YSZ. This kind of species hop between different surfaces is referred to as spillover in the heterogeneous catalysis literature. At

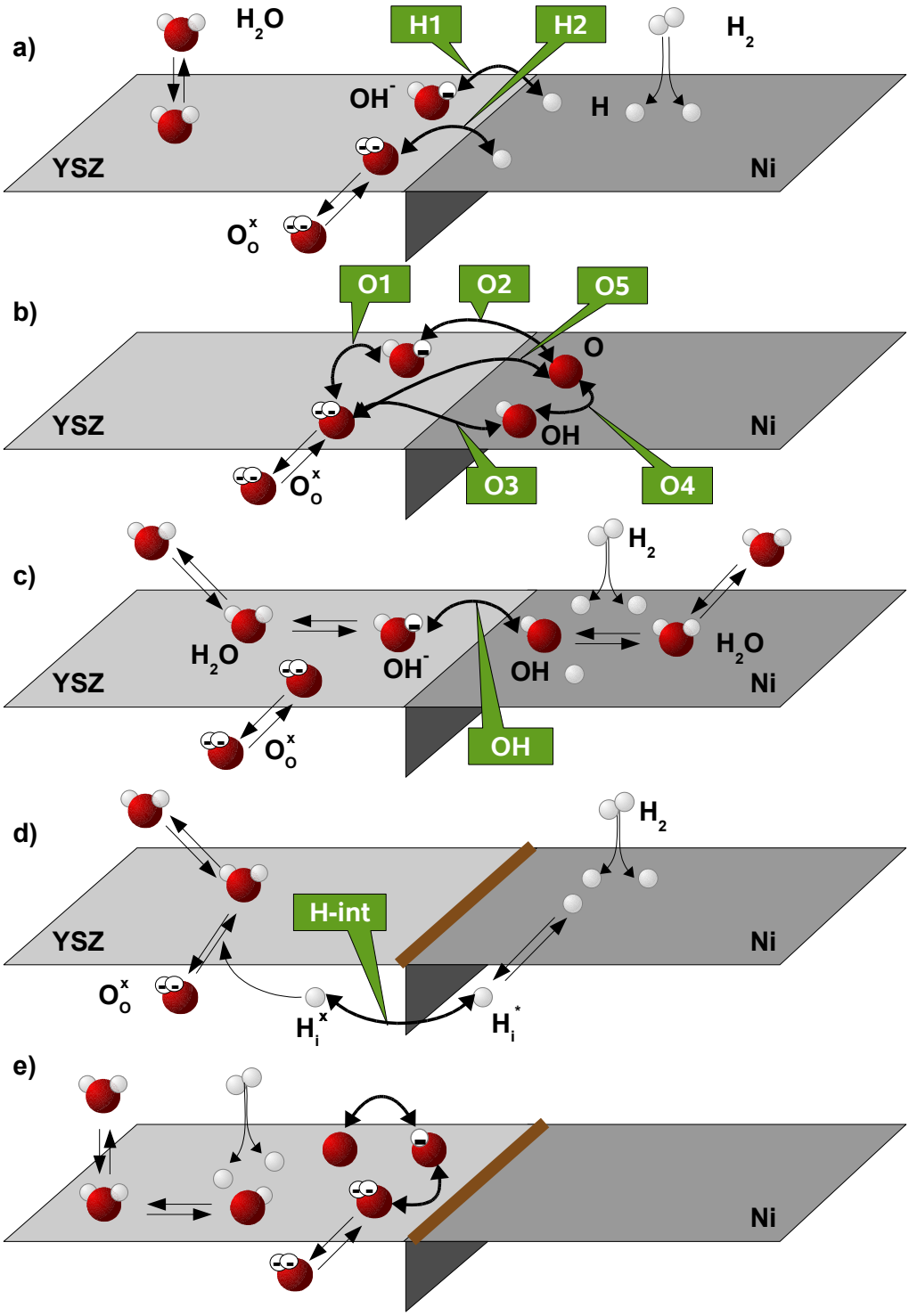

Figure 3.1: *Elementary kinetic scenarios at a Ni/YSZ three-phase boundary. Each charge-transfer reaction is a reversible reaction taking up or releasing charge to the valence band of the Ni electrode. a) Spillover of hydrogen from the Ni surface onto an oxygen ion or hydroxyl ion on the YSZ surface. b) Charge-transfer reactions with and without spillover of oxygen ions from the YSZ surface to the Ni surface. c) Hydroxyl spillover from the YSZ surface to the Ni surface. d) Charge-transfer by an interstitial proton. e) Charge-transfer and reactions on the electrolyte surface only. The brown "walls" in panels d) and e) indicate potential segregated impurities.*

the SOFC anode, spillover is accompanied by charge transfer. Both reactions may be active in parallel or consecutively. Note that H_2 adsorbs on the Ni surface, but H_2O desorbs from the YSZ surface. The pathway was proposed by several authors [16, 28, 35, 66, 67, 74–76]. Although there is, to the best of our knowledge, no direct experimental evidence of hydrogen spillover, the feasibility of this mechanism is supported by the possibility of fast surface transport of both, adsorbed hydrogen on the Ni surface [77] and protons on the YSZ surface [78].

(b) *Oxygen spillover.* Oxygen ions (formally O^{2-}_{YSZ}) may hop from the YSZ surface to the Ni surface, undergoing two charge-transfer reactions that can take place before, after or during the hop (Reactions O1-O5). Subsequent chemical reactions of hydrogen and oxygen species, including adsorption of molecular H_2 and desorption of H_2O, take place on the Ni surface. This pathway was proposed by several authors [17, 68, 71, 79–82]. There is direct experimental evidence for oxygen spillover at Pt/YSZ electrodes from photoelectron emission microscopy [83].

(c) *Hydroxyl spillover.* Spillover of hydroxyl ions (formally OH^-_{YSZ}) from the YSZ to the Ni surface has been proposed [20] (Reaction OH). OH^-_{YSZ} is formed from adsorption and dissociation of water on YSZ.

(d) *Interstitial hydrogen transfer.* At the typically high SOFC operating temperatures, both interstitial hydrogen atoms in bulk Ni and interstitial protons in bulk YSZ are present in concentrations around 0.1 %. Charge transfer may therefore take place at the two-phase boundary of Ni and YSZ. Interstitial hydrogen and protons are formed via surface adsorption, dissociation and surface/bulk exchange from H_2 on Ni and H_2O on YSZ, respectively. This pathway was proposed by several authors [69, 84–86]. It takes place at a 2D surface instead of a 1D line as the spillover pathways, thus potentially supporting higher currents.

(e) *Reactive electrolyte.* Oxygen ions can be oxidised to form oxygen atoms on the YSZ surface. Due to the low electronic conductivity of YSZ, this is only possible close to the TPB. Atomic oxygen can undergo chemical reactions on YSZ in analogy to the scenario shown in (a) on Ni surface. Mixed ionic and electronic conductivity of the electrolyte can make this a preferential pathway, as charge transfer can take place over the complete electrolyte surface area. Nevertheless, this mechanism has been proposed for Ni/YSZ anodes [87, 88].

The spillover pathways (a)-(c) require direct contact between the Ni and the YSZ surfaces. It was observed that segregated impurities may partially or completely block the three-phase boundary and the YSZ surface [21, 89], as indicated in panels (d) and (e). The impurities may effectively suppress spillover reactions. In this case, the interstitial hydrogen transfer pathway (d) and the reactive electrolyte pathway (e) are more likely [21, 65].

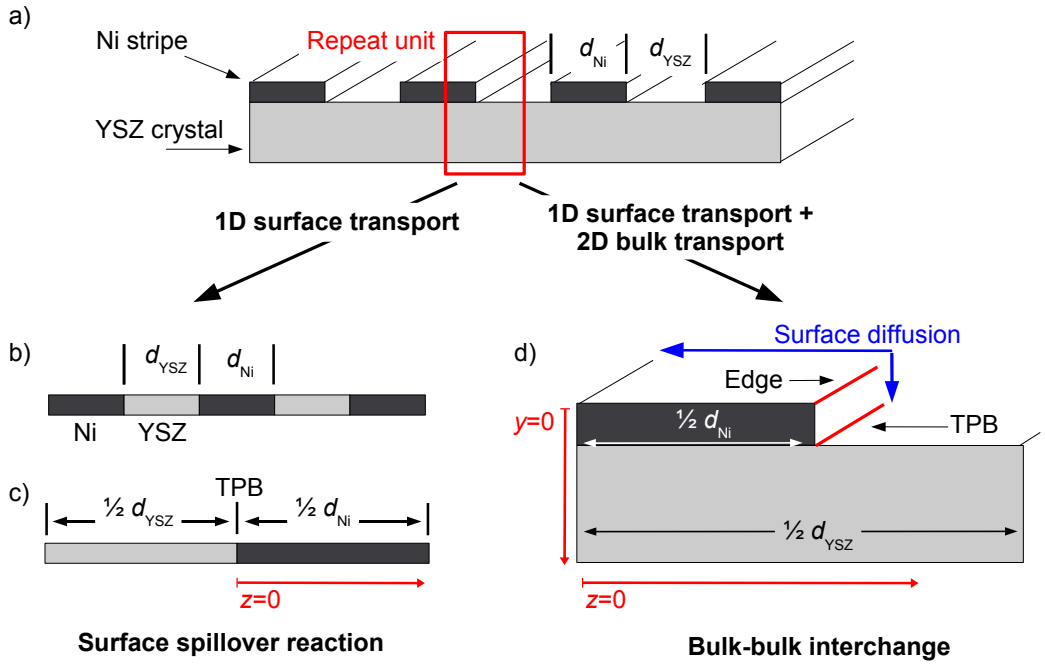

Figure 3.2: *a) Schematic view of the 3D pattern geometry. b) and c) Representation of the 3D structure by a 1D model that allows to simulate surface diffusion perpendicular to the TPB line used for charge-transfer reactions based on surface spillover reactions (Fig. 3.1 a-c). d) Modelling domain including 2D bulk diffusion and 1D surface diffusion used for simulations based on the interstitial hydrogen transfer (Fig. 3.1 d).*

3.3 Model

The model describes the anode half cell of an SOFC. It represents the experimental situation of a patterned Ni anode on a YSZ single crystal with reference electrode shown in Fig. 3.2 a. To perform the simulations the 3D anode design is mapped to a periodic computational domain: (1) For studies including surface-spillover processes only, a 1D representation of the electrode and electrolyte surfaces is used, where transport occurs only in z-direction perpendicular to the TPB (Fig. 3.2 c). (2) For simulations bases on the bulk-bulk interchange of the interstitial hydrogen transfer species adsorbed on the Ni-electrode diffuse on the top and right surface of the electrode and YSZ-adsorbed species on the uncovered YSZ surface area (Fig. 3.2 d). This study is performed within the physically based modelling framework described in detail in Ch. 2. The governing model equations are summarised in Tab. 3.3.2; this Table also defines all symbols and units used hereafter. The main model assumptions are:

- Electrochemical reactivity is described by *elementary kinetics*, that is, by resolving single steps that represent chemical reactivity on a molec-

ular scale. The models are thermodynamically consistent by using reversible reactions throughout. For surface chemistry and surface transport a mean-field approach is used. A set of elementary reactions, alongside with the according kinetic parameters and thermodynamic data, form the so-called *reaction mechanism*.

- The charge-transfer reaction is assumed to be either a *surface spillover reaction* taking place at the TPB (cf. Fig. 3.2 a-c) or a *bulk-bulk transfer* of interstitial species taking place at the 2D interface of electrolyte and electrode (cf. Fig. 3.2 d).
- *Surface diffusion* is modelled in one dimension perpendicular to the TPB on the basis of a surface-adapted Fickian diffusion approach.
- *Bulk transport* of interstitial hydrogen is modelled by Fickian diffusion inside the bulk electrode and bulk electrolyte in two dimensions.
- The gas volume above the anode is assumed to have a constant composition, reflecting the constant gas supply of the anode in the experimental setup.
- Mapping the experimental setup used by Bieberle et al., the model describes a reference electrode setup.

3.3.1 Simulation methodology

The model equations described in this Section represent the implicit relationship between current and overpotential. We have implemented the model into the software package DENIS [28] which allows the simulation of current-voltage relations as well as electrochemical impedance spectra.

The coupled chemistry and surface transport is represented by a partial differential equation (PDE) (Tab. 3.3.2, Eq. 3.4). The PDE is spatially discretised using a finite volume technique. We use 30 grid points spaced on a logarithmic scale between 0.2 nm and 5 μm. The resulting system of differential algebraic equations (DAE) is numerically time-integrated using the stiff DAE solver LIMEX [90] . Chemistry source terms are calculated using the software package DETCHEM [33].

In order to simulate Tafel plots, the overpotential is set to a constant value and the equation system is solved for the current in the steady state. This is preformed for a range of overpotentials. The calculation of 2000 points between -0.5 V and +0.5 V takes 6 min. on a 2 GHz desktop computer. The polarisation resistance R_{pol} is calculated from the current-overpotential curves according to its definition,

$$R_{\mathrm{pol}} = \frac{\mathrm{d}\eta}{\mathrm{d}i} \; . \tag{3.2}$$

Table 3.1: *Thermodynamic data for gas-phase, surface, and bulk species given as molar entropies s_i in [J/(K·mol)] and molar enthalpies h_i in [kJ/mol] at 973 K. a) Temperature-dependent thermodynamical data are available. b) Data derived from fit to experimental data, no temperature dependence. c) Reference species, thermodynamic parameters set to zero.*

Species	h_i	s_i	Ref.	
Gas				
H_2O_{gas}	-217	222	[91]	a)
$H_{2,gas}$	20	156	[91]	a)
$O_{2,gas}$	22	233	[91]	a)
Nickel surface				
H_{Ni}	-32	41	[34]	b)
O_{Ni}	-222	39	[34]	b)
OH_{Ni}	-193	106	[34]	b)
H_2O_{Ni}	-273	130	[34]	b)
$\square_{Ni}$	0	0	[34]	c)

Species	h_i	s_i	Ref.
YSZ surface			
OH^-_{YSZ}	-283	67	[78]
O^{2-}_{YSZ}	-236	0	[27]
H_2O_{YSZ}	-273	98	[78]
$\square_{YSZ}$	0	0	
Bulk species			
$V^{\bullet\bullet}_{O\,YSZ}$	0	0	
$H^x_{i\,Ni}$	36	42	[92]
$H^{\bullet}_{i\,YSZ}$	16	65	[93]
$O^X_{O\,YSZ}$	-236	0	[27]

From this definition it follows, that a sufficient number of polarisation resistances calculated for different overpotentials holds the same information as a Tafel plot.

3.3.2 Compilation of model parameters

Thermodynamics The anode half-cell system is assumed to consist of three gas-phase species ($H_{2,gas}$, $H_2O_{,gas}$ and $O_{2,gas}$), five species attached to the Ni surface (H_{Ni}, O_{Ni}, OH_{Ni}, H_2O_{Ni}, and $\square_{Ni}$), four species attached to the YSZ surface (O^{2-}_{YSZ}, OH^-_{YSZ}, H_2O_{YSZ}, and $\square_{YSZ}$), two bulk lattice YSZ species ($O^X_{O\,YSZ}$ and $V^{\bullet\bullet}_{O\,YSZ}$), and two interstitial species ($H^{\bullet}_{i\,YSZ}$, $H^x_{i\,Ni}$). Here $\square$ denotes a free surface site. The thermodynamic data (molar enthalpies and entropies) of these species form the basis for consistent kinetic simulations [28]. They are summarised in Tab. 3.1. The compilation of these data is described in [27]. The molar enthalpies and entropies for the interstitial hydrogen species in nickel and YSZ were extracted from equilibrium solvation experiments from Wagner and McLellan. Details are given in the Appendix B.

Chemical kinetics. The electrode, electrolyte and gas phase form a chemically coupled system. The gas-phase species interact with the surface to form surface-adsorbed species. The adsorbates react with other adsorbed species originating from surface reactions, spillover reactions, or bulk-surface exchange reactions. All chemical reactions in this system are resolved into

elementary steps. The rate constants for the forward reactions are calculated via an Arrhenius ansatz. For adsorption reactions, sticking coefficients are transformed into a kinetical description [49]. The rate constant for the reverse reaction is calculated in a thermodynamically consistent way from the molar enthalpies and entropies 3.7. For every elementary step, we need to specify the pre-exponential factor $k^0_{\mathrm{f},m}$, the exponent of its temperature dependence β_m, and the activation energy $E^{\mathrm{act}}_{\mathrm{f},m}$ of the forward reaction. In the remainder of this Section, we describe the origin of these parameters. All reactions along with their parameters are summarised in Tab. 3.2.

The Ni surface chemistry has been well-studied in the context of heterogeneous catalysis. The reaction mechanism used in this work is taken from the work of Janardhanan and Deutschmann [34]. This mechanism was developed using a combination of theory and available surface science and catalysis experiments. It was then validated in a specifically designed experiment consisting of a single cermet anode (no electrolyte or cathode) in a flow reactor with gas analysis under various conditions of steam reforming and dry reforming [36]. Note that Janardhanan and Deutschmann have formulated their reaction mechanism in terms of non-reversible elementary steps, that is, they give independent values for forward and reverse rate coefficients. In order to ensure thermodynamic consistency, we use only the forward rate coefficients and calculate the reverse rate constant according to thermodynamic consistency.

For the YSZ surface there is, to the best of our knowledge, no validated reaction mechanism available in literature. The mechanism used in this work (Tab. 3.2) is comprised of the following elementary reaction steps suggested by [78, 94], 1) molecular adsorption and desorption of water, 2) water dissociation and 3) bulk-surface exchange inter-converting bulk oxygen ions ($\mathrm{O}^{\mathrm{X}}_{\mathrm{O\,YSZ}}$) and surface adsorbed oxygen ions ($\mathrm{O}^{2-}_{\mathrm{YSZ}}$). Lacking detailed experimental or theoretical data, the rate coefficients for these reactions are obtained as typical "educated guesses" as follows.

For the adsorption reaction of H_2O on YSZ we assume a sticking coefficient of 1, owing to the strong interaction of oxidic surfaces with polar water molecules. The adsorption is assumed to be non-activated; the activation energy for the desorption reaction thus corresponds to the thermodynamic stability of adsorbed water.

For the water dissociation reaction, we estimate the pre-exponential factor via [54]

$$k^0 = \frac{\nu_{\mathrm{at}}}{\Gamma_k} \tag{3.3}$$

where ν_{at} is the attempt frequency which is related to the vibrational frequency of the adsorbate. A value of 10^{13} Hz is often used [54, 95, 96]. This value and the resulting pre-exponential factor must be seen as a rough estimate. For example, a comparison of the pre-exponential factor for the dissociation of water on Ni calculated based on Eq. 3.3 with the value given in

Tab. 3.2 results in a difference of two orders of magnitude. The activation energy for the water dissociation is set to 0.1 eV. This is a value that was obtained in density functional theory (DFT) studies of H_2O dissociation at defect sites of TiO_2 [97]; although this is a very different chemical system, it reflects the observation that H_2O dissociation on defective oxidic surfaces proceeds fast [98].

Bulk diffusion. Bulk transport of interstitial species takes place by a vacancy diffusion mechanism ($O^{X}_{O\,YSZ}$) or by interstitial diffusion ($H^{x}_{i\,Ni}$, $H^{\bullet}_{i\,YSZ}$). In all cases the bulk-surface exchange step can in principle be seen as diffusion over the terminating bulk layer to the surface. We therefore take the activation energy for this reaction from experimental data for bulk diffusion [92, 93, 99]. We are aware that this assumption neglects effects such as lattice reconstruction and symmetry breaking close to interfaces or the formation of charged complexes. The pre-exponential factor is calculated from Eq. 3.3.

Surface diffusion. Charge transfer by surface spillover is associated with mass transport over the TPB. This may lead to concentration gradients not only of the spilling species but, because of the chemical coupling, of all surface-adsorbed species. In order to estimate the diffusion coefficients, we treat the surface adsorbates as a one-dimensional hard-core lattice gas sometimes referred to as Langmuir lattice gas as described in detail in Ch 2.

The literature on diffusivities of Ni- and YSZ-adsorbed species is sparse, making the reliable assessment of surface diffusion coefficients difficult. Tab. 3.3 lists a compilation of diffusion coefficients from various literature sources. Where more than one data source was available, an average value was estimated and used for the calculations, whereas the lowest and highest available values serve as boundaries of the confidence interval for the respective diffusion coefficient. Most Ni data have their origin in DFT calculations of the activation energy of adsorbate movement between adjacent surface sites. The diffusivity of surface oxide ions on YSZ is taken from various measurements of YSZ, ZrO_2 and TiO_2. The diffusion coefficients for OH and H_2O on YSZ are calculated from Eq. 3.3 and 3.10 using the measured (macroscopic) activation energy for surface ionic conduction of YSZ powder [78]. We expect a large uncertainty associated with the diffusion coefficients given in Tab. 3.3 for several reasons. (a) The description of adsorbates as random walkers neglects interaction between adsorbates, which may be significant at high coverages [61, 63] or when the adsorbates are charged [72]. (b) The Ni self-diffusion coefficient is estimated to be $1.4 \cdot 10^{-7}\,{}^{\mathrm{cm}^2}/_{\mathrm{s}}$ at 973 K [114]; it may be possible that species adsorbed on a Ni atom can move as pair at the Ni self-diffusion rate, increasing adsorbate diffusivity. (c) The DFT calculations for determining diffusion coefficients were performed at ideal flat surfaces, while realistic polycrystalline surfaces may show high diffusivities along grain boundaries. (d) Subsurface diffusion may contribute to the transport. We estimate that the uncertainty in the diffusivities is up to 2-3 orders of magnitude.

Table 3.2: *Standard set of model parameters for Ni and YSZ surface reactions and charge-transfer reactions. Surface site densities are* $\Gamma_{YSZ} = 1.3 \cdot 10^{-9}$ mol/cm² *and* $\Gamma_{Ni} = 6.1 \cdot 10^{-9}$ mol/cm². *a) Calculated from sticking coefficients* S_i *[49] b)* k_i^0 *calculated from Eq. 3.3. c) Parameter obtained from fitting to experimental data and given in Tab. 3.6; for the CT reactions see also Fig. 3.1.*

No.	Reaction	k_i^0	E_i^{act} [kJ/mol]	β_i	Comment
	YSZ surface reactions				
1	$H_2O_{gas} + \square_{YSZ} \rightleftharpoons H_2O_{YsZ}$	$6.6 \cdot 10^{11}$ cm³/(mol·s)	0	0.5	S= 1, a)
2	$H_2O_{YSZ} + O^{2-}_{YSZ} \rightleftharpoons 2 \cdot OH^-_{YSZ}$	$7.7 \cdot 10^{21}$ cm²/(mol·s)	9.6	0	b), [97]
3	$H^{\bullet}_{i\,YSZ} + OH^-_{YSZ} \rightleftharpoons V_{YSZ} + H_2O_{YSZ}$	$7.7 \cdot 10^{21}$ cm²/(mol·s)	75	0	b)
4	$O^{2-}_{YSZ} + V^{\bullet\bullet}_{O\,YSZ} \rightleftharpoons O^{X}_{O\,YSZ} + \square_{YSZ}$	$7.7 \cdot 10^{21}$ cm²/(mol·s)	90.9	0	b),[36, 44, 100–102]
	Ni surface reactions				
5	$H_2O_{gas} + \square_{Ni} \rightleftharpoons H_2O_{Ni}$	$1.4 \cdot 10^{10}$ cm³/(mol·s)	0	0.5	S= 0.1 [36], a)
6	$H_{2,gas} + 2 \cdot \square_{Ni} \rightleftharpoons 2 \cdot H_{Ni}$	$9.8 \cdot 10^{17}$ cm⁵/(mol·s)	0	0.5	S= 0.01 [36], a)
7	$H_{Ni} + O_{Ni} \rightleftharpoons OH_{Ni} + \square_{Ni}$	$5.0 \cdot 10^{22}$ cm²/(mol·s)	97	0	[36]
8	$H_2O_{Ni} + O_{Ni} \rightleftharpoons 2 \cdot OH_{Ni}$	$5.4 \cdot 10^{23}$ cm²/(mol·s)	209	0	[36]
9	$OH_{Ni} + H_{Ni} \rightleftharpoons H_2O_{Ni} + \square_{Ni}$	$3.0 \cdot 10^{20}$ cm²/(mol·s)	43	0	[36]
10	$H_{Ni} + V_{Ni} \rightleftharpoons H^{x}_{i\,Ni} + \square_{Ni}$	$1.6 \cdot 10^{21}$ cm²/(mol·s)	45	0	b)
	Charge-transfer reactions				
H1	$H_{Ni} + OH^-_{YSZ} \rightleftharpoons H_2O_{YSZ} + e'_{Ni} + \square_{Ni}$	c)	c)	0	$\alpha = 0.5$
H2	$H_{Ni} + O^{2-}_{YSZ} \rightleftharpoons OH^-_{YSZ} + e'_{Ni} + \square_{Ni}$	c)	c)	0	$\alpha = 0.5$
O1	$O^{2-}_{YSZ} \rightleftharpoons O^-_{YSZ} + e'_{Ni}$	c)	c)	0	$\alpha = 0.5$
O2	$O^-_{YSZ} + \square_{Ni} \rightleftharpoons O_{Ni} + e'_{Ni} + \square_{YSZ}$	c)	c)	0	$\alpha = 0.5$
O3	$O^{2-}_{YSZ} + \square_{Ni} \rightleftharpoons O^-_{Ni} + e'_{Ni} + \square_{YSZ}$	c)	c)	0	$\alpha = 0.5$
O4	$O^-_{Ni} \rightleftharpoons O_{Ni} + e'_{Ni}$	c)	c)	0	$\alpha = 0.5$
O5	$O^{2-}_{YSZ} + \square_{Ni} \rightleftharpoons O_{Ni} + 2 \cdot e'_{Ni} + \square_{YSZ}$	c)	c)	0	$\alpha = 0.5$
OH	$OH^-_{YSZ} + \square_{Ni} \rightleftharpoons OH_{Ni} + e'_{Ni} + \square_{YSZ}$	c)	c)	0	$\alpha = 0.5$
HB	$V_{YSZ} + H^{x}_{i\,Ni} \rightleftharpoons V_{Ni} + H^{\bullet}_{i\,YSZ} + e'_{Ni}$	c)	c)	0	$\alpha = 0.5$

Table 3.3: *Summarised literature survey of surface and bulk diffusion coefficients. The "standard" values are used in this work. a) Pre-exponential factor factor D_i^0 calculated by Eq. 3.11 with $\nu_{\mathrm{at}} = 10^{13}\mathrm{Hz}$ and lattice constants of $l_{\mathrm{Ni}} = 3.6{\cdot}10^{-10}\mathrm{m}$ [103] and $l_{\mathrm{YSZ}} = 5.1 \cdot 10^{-10}\mathrm{m}$ [104]. b) E_i^{act} from Rh for comparison. c) Value was taken from ZrO_2, other values for comparison.*

Species	D_i^0 [$\mathrm{cm^2/s}$]	E_i^{act} [$\mathrm{kJ/mol}$]	Ref.	D_i [$\mathrm{cm^2/s}$] at 973 K	
H_{Ni}	$3.7 \cdot 10^{-3}$	11.3	[105]	$9.2 \cdot 10^{-4}$	
	$2.8 \cdot 10^{-3}$	18.9	[77]	$2.7 \cdot 10^{-4}$	
	$6 \cdot 10^{-3}$	14.4	[82]	$1.0 \cdot 10^{-3}$	a)
	$6 \cdot 10^{-3}$	13	[106]	$1.2 \cdot 10^{-3}$	a)
Std.	$4.6 \cdot 10^{-3}$	14.4		$7.8 \cdot 10^{-4}$	
O_{Ni}	$7 \cdot 10^{-3}$	45.3 - 55.0	[107]	$8 \cdot 10^{-5}$-$3 \cdot 10^{-5}$	a), b)
	$6 \cdot 10^{-3}$	55.1	[108]	$6.6 \cdot 10^{-6}$	a)
	$6 \cdot 10^{-3}$	117.4	[109]	$3.0 \cdot 10^{-9}$	a)
Std.	$6.3 \cdot 10^{-3}$	61.3		$3.2 \cdot 10^{-6}$	
OH_{Ni}	$6 \cdot 10^{-3}$	55.2	[109]	$6.5 \cdot 10^{-6}$	a)
	$6 \cdot 10^{-3}$	5.8	[108]	$2.9 \cdot 10^{-3}$	a)
Std.	$6.0 \cdot 10^{-3}$	30.5		$1.4 \cdot 10^{-4}$	
H_2O_{Ni}	$6 \cdot 10^{-3}$	55.9	[109]	$6 \cdot 10^{-6}$	a)
	$6 \cdot 10^{-3}$	~ 0	[108]	$6 \cdot 10^{-3}$	a)
Std.	$6 \cdot 10^{-3}$	28.0		$1.8 \cdot 10^{-4}$	a)
$H^{x}_{i\,Ni}$	$7.6 \cdot 10^{-2}$	41	[110]	$4.7 \cdot 10^{-4}$	
O^{2-}_{YSZ}	$5.5 \cdot 10^{-7}$	90	[111]	$8.1 \cdot 10^{-12}$	ZrO_2
		27	[112]		CeO_2
	$3 \cdot 10^{-9}$	29	[113]	$7.3 \cdot 10^{-11}$	TiO_2, a)
Std.	$5.5 \cdot 10^{-7}$	90		$8.1 \cdot 10^{-12}$	c)
H_2O_{YSZ}	$1.3 \cdot 10^{-2}$	55	[78]	$1.5 \cdot 10^{-5}$	a)
OH^{-}_{YSZ}	$1.3 \cdot 10^{-2}$	55	[78]	$1.5 \cdot 10^{-5}$	a)
$H^{\bullet}_{i\,YSZ}$	$5.6 \cdot 10^{-3}$	86	[93]	$1.4 \cdot 10^{-7}$	

Tabulated model equations

Physicochemical process	Model equation	Eq. No.
Reaction-diffusion model (Ni and YSZ surfaces)		
Surface coverages	$\frac{\partial}{\partial t}\theta_i = \frac{\sigma_i}{\Gamma_k}\dot{s}_i^{\mathrm{A}} - \frac{\partial}{\partial z}J_i^{\mathrm{surf}}$	(3.4)
Chemistry source terms	$\dot{s}_i^{\mathrm{A}} = \sum_m \nu_{i,m}\left(k_{\mathrm{f},m}\prod_{j\in R_{\mathrm{f},m}} c_j^{\nu_j^{'}} - k_{\mathrm{r},m}\prod_{j\in R_{\mathrm{r},m}} c_j^{\nu_j^{''}}\right)$	(3.5)
Forward reaction rate constant	$k_{\mathrm{f},m} = k_{\mathrm{f},m}^0 \cdot T^{\beta m} \cdot \exp\left(-\frac{E_{\mathrm{f},m}^{\mathrm{act}}}{RT}\right)$	(3.6)
Reverse reaction rate constant	$k_{\mathrm{r},m} = k_{\mathrm{f},m} \cdot \exp\left(\frac{\Delta G_m}{RT}\right)$	(3.7)
Gibbs free reaction enthalpy	$\Delta G_m = \sum_{i\in R_{\mathrm{f},m}} \nu_{i,m}^{'}\left(h_i - T\cdot s_i\right) - \sum_{i\in R_{\mathrm{r},m}} \nu_{i,m}^{''}\left(h_i - T\cdot s_i\right)$	(3.8)
Diffusive flux	$J_i^{\mathrm{surf}} = -D_i^{\mathrm{surf}} \cdot \theta_{\square} \cdot \frac{\partial \theta_i}{\partial z}$	(3.9)
Diffusion coefficient	$D_i^{\mathrm{surf}} = D_i^0 \cdot \mathrm{e}^{-\frac{E_i^{\mathrm{act}}}{RT}}$.	(3.10)
Diffusion coefficient (pre-exponential factor)	$D_i^0 = \frac{1}{2} \cdot \nu_{\mathrm{at}} \cdot l^2$.	(3.11)
Electrochemistry		
Forward charge transfer reaction rate constant	$k_{\mathrm{f,ct}} = k_{\mathrm{f,ct}}^0 \exp\left(-\frac{E_{\mathrm{f,ct}}^{\mathrm{act}}}{RT}\right)\exp\left(\alpha\frac{zF}{RT}\cdot\Delta\phi\right)$	(3.12)
Reverse charge transfer reaction rate constant	$k_{\mathrm{r,ct}} = k_{\mathrm{f,ct}} \exp\left(\frac{\Delta G_m}{RT}\right)\exp\left(-\left(1-\alpha\right)\frac{zF}{RT}\cdot\Delta\phi\right)$	(3.13)
Electric potential step between Ni and YSZ	$\Delta\phi_{\mathrm{work}} = \phi_{\mathrm{elde,work}} - \phi_{\mathrm{elyt,work}}$ and $\Delta\phi_{\mathrm{ref}} = \phi_{\mathrm{elde,ref}} - \phi_{\mathrm{elyt,ref}}$	(3.14)
Potential distribution in the solid electrolyte	$\frac{\partial}{\partial y}\left(\sigma_{\mathrm{elyt}}\frac{\partial}{\partial y}\phi_{\mathrm{elyt}}\right) = 0$	(3.15)
Electrolyte resistance	$R_{\mathrm{elyt}} = \frac{T}{A_\Sigma}\cdot\exp\left(\frac{E_\sigma}{RT}\right)$	(3.16)
Overpotential	$\eta = \phi_{\mathrm{elde,work}} - \phi_{\mathrm{elde,ref}}$	(3.17)
Faradaic current of single charge-transfer reaction	$i_{\mathrm{F,ct}}^{\mathrm{A}} = zFl_{\mathrm{TPB}}^{\mathrm{A}}\left(k_{\mathrm{f}}\prod_{j\in \mathrm{R}_{\mathrm{f,ct}}}\theta_j^{\nu_j^{'}} - k_{\mathrm{r}}\prod_{j\in \mathrm{R}_{\mathrm{r,ct}}}\theta_j^{\nu_j^{''}}\right)$	(3.18)
Tafel slope	$m_{\mathrm{Tafel}} = \alpha\cdot z$	(3.19)
Total Faradaic current of the charge-transfer mechanism	$i_{\mathrm{F}}^{\mathrm{A}} = \sum_{\text{all CTRs}} i_{\mathrm{F,ct}}^{\mathrm{A}}$	(3.20)

Table 3.4: *Experimentally determined polarisation resistances $R_{\mathrm{pol}}^{\mathrm{exp}}$ [16] at standard conditions (Tab. 3.5), resulting effectiveness factors f_s and corresponding effective $l_{\mathrm{TPB}}^{\mathrm{A}}$. Best-performing sample 3 is used as reference with the nominal $l_{\mathrm{TPB}}^{\mathrm{A}} = 3.7$ m/cm².*

Sample	Investigated parameter in experiment	$R_{\mathrm{pol}}^{\mathrm{exp}}$ [Ω/cm²]	f_s	Effective $l_{\mathrm{TPB}}^{\mathrm{A}}$ [m/cm²]
1	$p(\mathrm{H_2}) = 2.5 \cdot 10^4 - 7.5 \cdot 10^4$ Pa	333	0.43	1.6
2	$p(\mathrm{H_2O}) = 4 \cdot 10^1 - 2 \cdot 10^3$ Pa	1230	0.12	0.4
3 (ref)	$T = 673 - 973$ K	142	1.0	3.7
4	$\eta = 0 - 200$ mV	362	0.39	1.4

3.4 Simulation targets for model validation

In this chapter, experimental data from patterned anodes obtained previously [16] are re-interpreted and used as targets for parameter estimation and model validation. Briefly, polarisation and electrochemical impedance measurements of photolithographically-prepared Ni/YSZ patterned anodes were carried out in a single gas chamber measurement setup at temperatures between 673 K and 973 K. The fuel gas consisted of a mixture of H_2, H_2O and N_2. The partial pressures of H_2 and H_2O were varied systematically, the latter by wetting of the fuel gas. Measurements were performed at anodic overpotentials between 0 and 400 mV. More detailed information on the preparation of the cells and the electrochemical characterisation is given in [16]. Consequently the simulation targets are the polarisation resistance R_{pol} and the slope m_{Tafel} of the IV curve under different fuel gas compositions and temperatures as well as the polarisation curve itself.

Tab. 3.4 shows the polarisation resistance obtained from impedance measurements $R_{\mathrm{pol}}^{\mathrm{exp}}$ for the four investigated samples obtained at the standard operating conditions given in Tab. 3.5. Sample-to-sample variations are present, even though nominally identical samples were used for the measurements. While parameter studies within one sample are not affected by the variations, a quantitative comparison of experiment and simulation should be based on the complete data set. For the present study, we assume that the sample-to-sample variation is due to a difference in the effective TPB length, as discussed below. An effectiveness factor $f_s = {}^{l_{\mathrm{TPB}}^{s}}/_{l_{\mathrm{TPB}}^{\mathrm{ref}}} = {}^{R_{\mathrm{pol}}^{\mathrm{exp,ref}}}/_{R_{\mathrm{pol}}^{\mathrm{exp},s}}$ was introduced which was used to scale the nominal TPB length. For the calculation of this factor, the the best-performing sample 3 was set as reference, assuming the nominal TPB length of 3.7 m/cm². All experimental data shown in this chapter are normalised using the effectiveness factor.

The assumption of a sample-specific effective TPB lengths is based on the following three arguments. Firstly, from similar systems it is known that impurities such as Si, Al or Na segregate to the interfaces of Ni/YSZ, Ni/gas-phase and YSZ/gas-phase [21, 115, 116]. Different sources of these impurities

Table 3.5: *Standard conditions used in experiments and simulations.*

Parameter	Value	Denotation
$p\mathrm{H_2}$	$2.5 \cdot 10^4$ Pa	Hydrogen partial pressure
$p\mathrm{H_2O}$	$5 \cdot 10^1$ Pa	Water partial pressure
p_{tot}	101325 Pa	Total gas-phase pressure
$l^{\mathrm{A}}_{\mathrm{TPB}}$	3.7 $\mathrm{m/cm^2}$	Length of the TPB
d_{Ni}	20 μm	Width of the Nickel stripes
d_{YSZ}	20 μm	Width of the YSZ stripes
η	0 V	Overpotential
T	973 K	Temperature

are being discussed in literature (electrode, electrolyte and insertion from the gas phase)[21, 116, 117]. Impurity segregation may lead to a blocking of active TPB sites, thereby reducing the effective TPB length. Secondly, the samples were fabricated in different sputtering machines which might result in small variations of surface roughness or grain size (as well as impurity level). Surface roughness and grain size may in turn influence the effective TPB length by influencing the etching quality. Finally, changes in the pattern structure may occur under operating conditions, additionally affecting the effective TPB length.

3.5 Results

In this Section we will compare the simulation results from the seven charge-transfer mechanisms illustrated in Fig. 3.1 a-d. Based on the identification of the most probable CT mechanism in Sec 3.5.1 we will identify the physical processes limiting the SOFC anode performance by a sensitivity analyses in Sec 3.5.2. In Sec. 3.5.4 the mechanism causing the apparent Tafel slope will be analysed and Sec. 3.5.3 will introduce possible model simplifications.The results from the bulk-exchange of the interstitial hydrogen transfer reaction are shown and discussed in Sec. 3.5.5.

3.5.1 Comparison of charge-transfer mechanisms

Only one or two charge-transfer reactions were enabled at a time in the simulations, while the other charge-transfer reactions were disabled. The other chemical reactions (Tab. 3.2, reactions 1-8) were always enabled, and thermo-

dynamic, kinetic, and most diffusional parameters from Tab. 3.2 and Tab. 3.3 were kept constant throughout all simulations.

The kinetics of the charge-transfer reactions are not available from independent literature. Instead, they were taken as free fit parameters for comparing simulation predictions with experimental data. For each CT mechanism, polarisation resistances and Tafel plots were calculated for all available experimental conditions (gas composition, temperature, polarisation). The rate coefficients of the active CT reactions (pre-exponential factors k^0, activation energies E^{act}) were optimised to yield best agreement with the experimental data. Proceeding in this way, it was not possible to reproduce the experiments with any of the assumed CT mechanisms. Only after additionally adjusting selected diffusion coefficients, agreement between simulation and experiment could be achieved. Tab. 3.6 shows the values of fitted rate coefficients and the adjusted diffusion coefficients along with a brief discussion of the parameter adjustment.

Simulation results for the seven investigated CT mechanisms by surface spillover using the optimised model parameters (Tab. 3.6) are compared to experimental data in Fig. 3.3. Experiments are shown as open symbols, simulations as lines. Each row represents the results for one CT mechanism, as indicated in the first column. The first three graphs in each row display the dependence of the polarisation resistance on one experimental parameter ($p\mathrm{H_2}$, $p\mathrm{H_2O}$, T) for four applied overpotentials (different symbols). The vertical lines in every graph mark the standard experimental condition (Tab. 3.5). The last graph in each row shows the Tafel plot at standard conditions. Note that the four graphs show normalised experimental data from different samples (cf. Tab. 3.4).

A number of observations are pointed out from the results shown in Fig. 3.3:

1. The experimentally observed slight decrease of polarisation resistance with increasing H_2 partial pressure is only reproduced by hydrogen spillover CT mechanisms (H1, H2, and H1+H2), whereas all other CT mechanisms predict an increasing polarisation resistance with increasing H_2 partial pressure.

2. All CT mechanisms are able to qualitatively reproduce the experimental decrease of polarisation resistance with increasing H_2O partial pressure; however, the double oxygen spillover CT mechanisms (O1+O2 and O3+O4) fail to give correct predictions when the electrode is polarised at high $p\mathrm{H_2O}$.

3. The decrease of polarisation resistance with increasing temperature is reproduced correctly by all except the H1, H2, and OH CT mechanisms.

4. All CT mechanisms are able to quantitatively reproduce the anodic branch of the experimental Tafel plot.

Table 3.6: *Investigated charge-transfer (CT) mechanisms and fitted model parameters.*

CT mechanism	Fitted parameter values		Discussion
H1	$k^0_{H1} = 2.5 \cdot 10^3$ mol/(cm·s), $E^{act}_{H1} = 175$ kJ/mol,	$D^0_{H_2O_{YSZ}} = 6.3 \cdot 10^{+3}$ cm^2/s, $D^0_{OH^-_{YSZ}} = 3.3 \cdot 10^{+3}$ cm^2/s	Diffusivities of OH^-_{YSZ} and H_2O increased by > 5 order of magnitude, probably too fast to be within certainty. Very high activation energy.
H2	$k^0_{H2} = 1.2 \cdot 10^{-2}$ mol/(cm·s), $E^{act}_{H2} = 113$ kJ/mol	$D^0_{H_2O_{YSZ}} = 7.3 \cdot 10^{-2}$ cm^2/s, $D^0_{OH^-_{YSZ}} = 6.3 \cdot 10^{-3}$ cm^2/s	Diffusivities of OH^-_{YSZ} and H_2O decreased by ~ 1 order of magnitude, likely within uncertainty. Very high activation energy.
H1+H2	$k^0_{H1} = 6.0 \cdot 10^2$ mol/(cm·s), $E^{act}_{H1} = 185$ kJ/mol, $k^0_{H2} = 8.0$ mol/(cm·s), $E^{act}_{H2} = 167$ kJ/mol	$D^0_{H_2O_{YSZ}} = 1.3 \cdot 10^{-3}$ cm^2/s, $D^0_{OH^-_{YSZ}} = 5.3 \cdot 10^{-3}$ cm^2/s	Diffusivities of OH^-_{YSZ} and H_2O decreased by > 1 order of magnitude, likely within uncertainty. Very high activation energy. Standard values for H_2O dissociation allow for parallel charge transfer steps
H1+H2 , no water dissoz.	$k^0_{H1} = 2.0 \cdot 10^2$ mol/(cm·s), $E^{act}_{H1} = 174$ kJ/mol, $k^0_{H2} = 4.2$ mol/(cm·s),$E^{act}_{H2} = 113$ kJ/mol,	$D^0_{H_2O_{YSZ}} = 3.3 \cdot 10^{+3}$ cm^2/s, $D^0_{OH^-_{YSZ}} = 3.3$ cm^2/s	Disabled H_2O dissociation (Fig. 3.4). Diffusivities of OH^-_{YSZ} and H_2O increased by 3-5 order of magnitude, probably to fast to be within uncertainty. Very high activation energy. H_2O dissociation probably too slow.
O1+O2	$k^0_{O1} = 2.4 \cdot 10^{-2}$ mol/(cm·s), $E^{act}_{O1} = 71$ kJ/mol, $k^0_{O2} = 2.5 \cdot 10^{-5}$ mol/(cm·s), $E^{act}_{O2} = 71$ kJ/mol	$D^0_{OH_{Ni}} = 1.0 \cdot 10^{-1}$ cm^2/s, $D^0_{O_{Ni}} = 8.0 \cdot 10^{-1}$ cm^2/s	Diffusivities ofOH_{Ni} and O_{Ni} increased by ~ 2 orders of magnitude, at the limit of uncertainty.
O3+O4	$k^0_{O3} = 7.3 \cdot 10^{-5}$ mol/(cm·s), $E^{act}_{O3} = 73$ kJ/mol, $k^0_{=O4} = 1.1 \cdot 10^{-4}$ mol/(cm·s), $E^{act}_{O4} = 73$ kJ/mol	$D^0_{O_{Ni}} = 5.0 \cdot 10^{-2}$ cm^2/s	Diffusivity of O_{Ni}increased by >5 orders of magnitude, probably too fast to be within uncertainty.
OH	$k^0_{OH} = 4.5 \cdot 10^{-4}$ mol/(cm·s), $E^{act}_{OH} = 73$ kJ/mol	$D^0_{OH_{Ni}} = 6.0$ cm^2/s, $D^0_{OH^-_{YSZ}} = 5.3$ cm^2/s	Diffusivities of OH_{Ni} and OH^-_{YSZ} increased by > 2 orders of magnitude, at the limit of uncertainty.
O5	$k^0_{O5} = 4.0 \cdot 10^{-4}$ mol/(cm·s), $E^{act}_{O5} = 74$ kJ/mol	$D^0_{O_{Ni}} = 1.0 \cdot 10^{+1}$ cm^2/s	Diffusivity of O_{Ni} increased by > 3 orders of magnitude, likely beyond uncertainty. Similar results if diffusivities of H_2O and OH on Ni are are increased to very high values.
H-Int	$k^0_{H-Int} = 4.5 \cdot 10^{-4}$ mol/(cm·s), $E^{act}_{OH} = 73$ kJ/mol	$D^0_{H^\bullet_{i\,YSZ}} = 0.6$ cm^2/s	Diffusivities of $H^\bullet_{i\,YSZ}$ increased by roughly 2 orders of magnitude. At the limit of uncertainty.

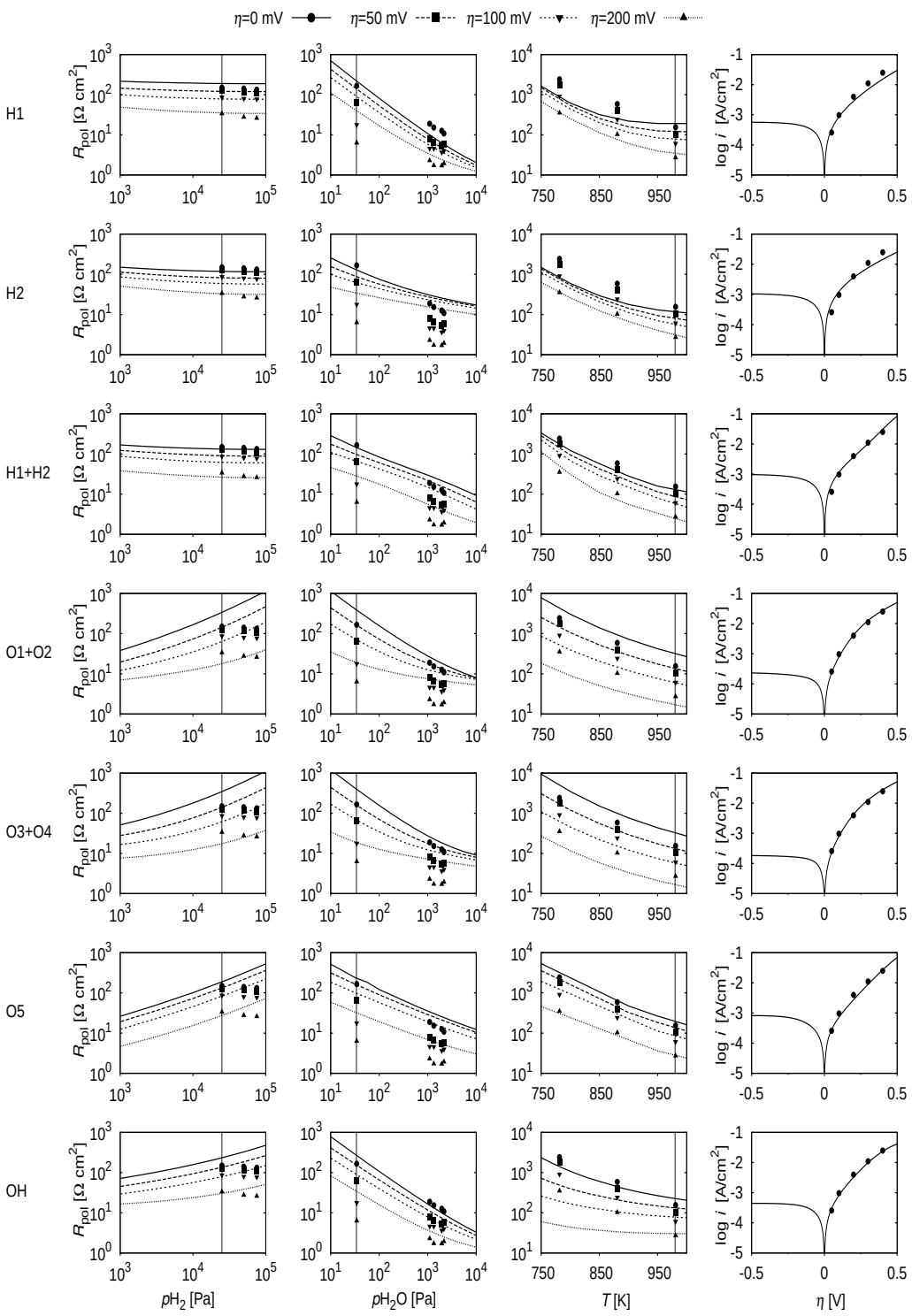

Figure 3.3: *Polarisation resistances and Tafel plots for the different CT mechanisms (see Fig. 3.1 and Tab. 3.6) based on the full reaction-diffusion model. For every CT mechanism, a set of four graphs in a row show the dependence of the polarisation resistance on hydrogen partial pressure, water partial pressure and temperature, as well as a Tafel plot. The vertical lines represent standard conditions (cf. Tab. 3.5). The calculations show that only a double hydrogen spillover (H1+H2) can reproduce the complete experimental trends.*

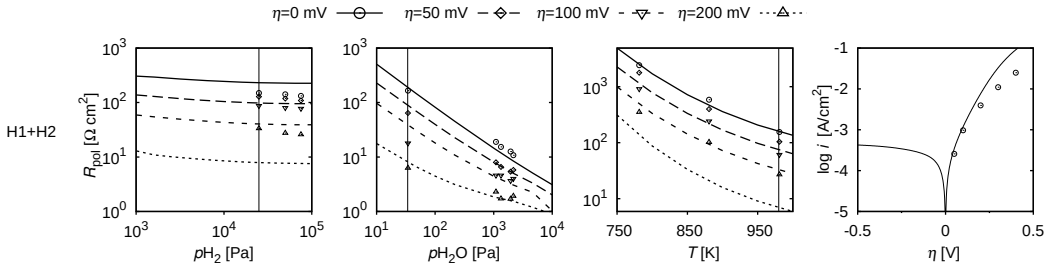

Figure 3.4: *Mechanism without water dissociation on YSZ: Polarisation curve and charge-transfer resistance for a double hydrogen spillover (cf. Fig. 3.1 a).*

5. All CT mechanisms show a low limiting current density on the cathodic branch. No experiments are available here. A more detailed analysis revealed that the limiting process is in all cases the diffusion of the spilling species. Note that the Tafel plots were taken at very low water partial pressure (standard conditions, Tab. 3.5).

Considering the complete data set, the overall best agreement between experiment and simulation is observed with the H1+H2 CT mechanism. The results from all CT mechanisms represent "best fits" of the charge-transfer kinetics and selected diffusion coefficients (cf. Tab. 3.6).

Influence of water dissociation on YSZ. As mentioned in the introduction, the mechanism describing the elementary reactions on the electrolyte surface is tentative. Goodwin has previously investigated hydrogen spillover (Reactions H1+H2) using a similar mechanism as presented in this paper, however without the inclusion of water dissociation on YSZ (Tab. 3.2, Reaction 2) [74]. In order to compare the present approach with the one presented by Goodwin, and in order to assess the importance of H_2O_{YSZ} dissociation, we have switched off this reaction and re-fitted charge transfer and diffusion coefficients (Tab. 3.6). Simulation results for this case are shown in Fig. 3.4. The simulations are qualitatively in good agreement with experimental data. However, the simulated Tafel slope is too high, as evident in the Tafel plot as well as the charge-transfer resistances under polarised conditions.

Contributions of surface diffusion. Spatial profiles of the surface coverages at $\eta = \pm 200$ mV are represented on a double logarithmic scale in Fig. 3.5. The upper panels show simulations for the best-matching hydrogen spillover, H1+H2 CT mechanism, and the lower panels for the oxygen spillover, O1+O2 CT mechanism. The latter mechanism was chosen for this comparison because it we judge it the most realistic oxygen spillover pathway from a chemical point of view. Simulations show strong concentration gradients close ($<10^{-8}$ m) to the TPB. For large distances from the TPB ($>10^{-7}$ m), the

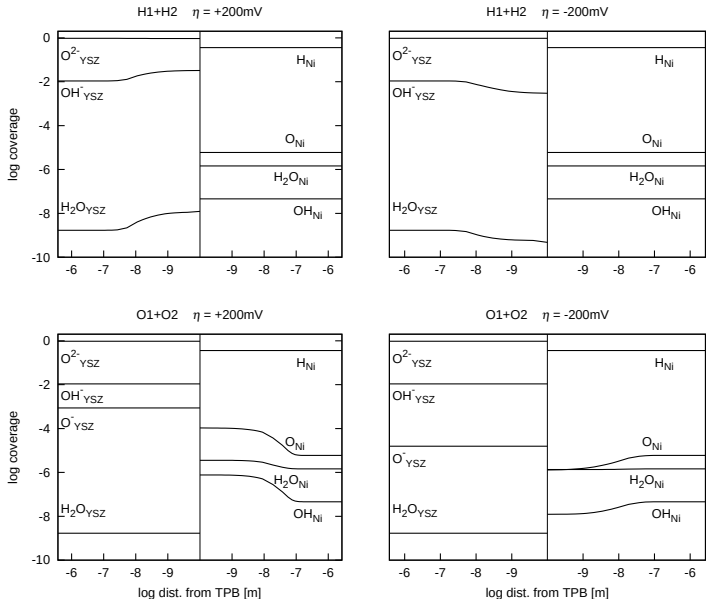

Figure 3.5: *Spatial variation of surface coverages at the polarised pattern anode. The vertical line represents the TPB. YSZ and Ni surfaces are represented left and right of the TPB, respectively.*

coverages reflect the adsorption/desorption equilibria. The figure shows that surface diffusion is slow compared to chemical kinetics: Spillover species undergo rapid chemical reactions before they can diffuse over large distances. In case of hydrogen spillover, there are almost no concentration gradients on the Ni surface. This is due to the fast diffusivity of H on Ni (Tab. 3.3). In case of oxygen spillover, all species except H show strong gradients on the Ni surface.

3.5.2 Sensitivity analysis

In order to identify the nature of the rate-determining process(es), a sensitivity analysis was performed for the best-matching CT mechanism (hydrogen spillover, H1+H2) at standard conditions (cf. Tab. 3.5). The target parameter for the analysis was the cell current i at overpotentials of $\eta = \pm 200$ mV as well as the polarisation resistance at $\eta = 0$ V. Each single model parameter P_i was consecutively increased by 10 % from its standard values P_i^0 to $P_i^+ = 1.1 \cdot P_i^0$. The resulting relative change of the cell current $\partial i = {}^{(i^+ - i^0)}/_{i^0}$ is related to the relative change of the parameter $\partial P_i = {}^{(P_i^+ - P_i^0)}/_{P_i^0} = 0.1$. The factor $f_{\mathrm{rel}} = {}^{\partial i}/_{\partial P_i}$ is the relative sensitivity of the current density with respect to changes in parameter P_i. A value of $f_{\mathrm{rel}}= 1$ means direct proportionality between the model parameter and the simulation target. A notable sensitivity of a model parameter (say, $f_{\mathrm{rel}} > 0.1$) means that the associated physicochemical process is rate-determining. At the same time, the parameter uncertainty propagates to the uncertainty of the simulation target; a sensitiv-

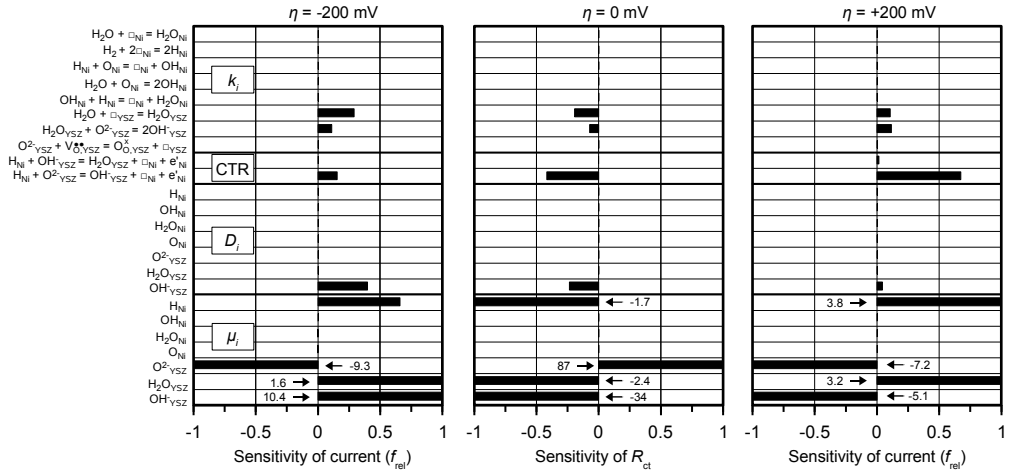

Figure 3.6: *Sensitivity of the current and the polarisation resistance on simulation parameters calculated for the H1+H2 hydrogen spillover mechanism at standard conditions (Tab. 3.5). The left and right panels show the relative sensitivity of the current i at $\eta = +200$ mV and $\eta = -200$ mV respectively. The center panel shows the relative sensitivity of the polarisation resistance R_{pol} at $\eta = 0$ mV. A relative sensitivity of 1 means proportionality between parameter and simulation target.*

ity analysis thus provides guidelines as for which parameters an independent validation is important. The results of the analysis are shown in Fig. 3.6. They are divided into four groups: rate coefficients for chemical reactions on the Ni and YSZ surfaces k_i, rate coefficients for the charge-transfer reactions (H1, H2), diffusion coefficients of all species D_i, and thermodynamic data of all species, where we choose the standard chemical potential $\mu_i = h_i - T \cdot s_i$ for the analysis.

Chemical kinetics. Only the influence of the pre-exponential factors is shown here. The activation energies show the identical trend, however with an increased sensitivity because they enter the reaction rate exponentially. The analysis shows that the heterogeneous surface chemistry on Ni is fast. There is almost no influence of the kinetic parameters related to the Ni surface. On the YSZ, the water adsorption/desorption reaction as well as the strongly related water dissociation reaction have a strong influence on the simulated current. Under anodic polarisation, water is formed on the YSZ surface and has to desorb into the gas phase. The analysis shows that this process is a bottleneck.

Charge-transfer kinetics. The charge-transfer reactions are directly connected to the electrical current. However, only the reaction H2 shows a notable sensitivity. The sensitivity is stronger for anodic polarisation than for cathodic polarisation. The second charge-transfer step H1 is fast and not rate-determining.

Surface diffusion. The only diffusion coefficient showing notable sensitivity is the one of the YSZ-adsorbed hydroxyl ion, $\mathrm{OH}^-_{\mathrm{YSZ}}$. As the charge-transfer

reaction H2 produces OH^-_{YSZ} at the TPB this species has to be converted into water to be desorbed into the gas phase. The water formation via reaction 2 (Tab. 3.2) cannot rapidly convert all hydroxyl ions OH^-_{YSZ}, causing a concentration gradient of OH^-_{YSZ} perpendicular to the TPB (cf. Fig. 3.5). Following this gradient, OH^-_{YSZ} species diffuse away from the TPB. The faster the OH^-_{YSZ} can diffuse, the more surface is available for their conversion, supporting a higher current.

Thermodynamic data. The standard chemical potential μ_i of the species participating in the charge-transfer reactions have the highest sensitivity of all investigated parameters. The influence of chemical potential is two-fold. First, because it is a direct measure of the stability of the adsorbed species, it influences the equilibrium coverage. Furthermore, differences in chemical potentials, that is, the Gibbs reaction enthalpy ΔG, influence the reverse reaction rate of the charge-transfer reaction (Tab. 3.3.2, Eq. 3.12) where μ_i enters in the exponent. Only the thermodynamic data of the species involved in the rate-determining steps show significant sensitivity, thus underlining the importance of these reactions to the system's performance.

Influence of polarisation. Comparing the analysis at overpotentials of -200, 0 and +200 mV shows essentially the same behaviour, with a slight variation of the relative importance of the rate-determining processes; i.e. at negative overpotentials surface diffusion on OH^-_{YSZ} outweights the CT reaction whereas at positive overpotentials the CT reactions dominates the behaviour. A change in the CT mechanism between anodic or cathodic polarisation is not identified.

3.5.3 Confined-region and fully-spreaded charge transfer

The coupling of chemical reactions to surface diffusion processes leads to strong concentration gradients over small distances close to the TPB (Fig. 3.5). Accurate numerical simulation of this situation requires a large number of grid points for finite-volume discretisation (cf. Section 3.3.1), which requires a relatively large computational effort. This is not a problem for the simple pattern geometry considered here, which can be described by a 1D model. However, application to porous electrodes or full cells requires 2D or even 3D simulations [28], which may result in very long simulation times. In this Subsection, we are investigating simplified models that allow increased calculation speed while still capturing the anode behaviour over the complete range of operating conditions. Two types of simplified models are investigated, (1) a "confined-region" charge-transfer model and (2) a "fully-spreaded" charge transfer model. In the "confined-region" charge transfer model, we assume that the surface can be divided into an electrochemically active TPB region extending a small distance from the TPB line onto both, Ni and YSZ surfaces, and electrochemically non-active regions further away from the TPB

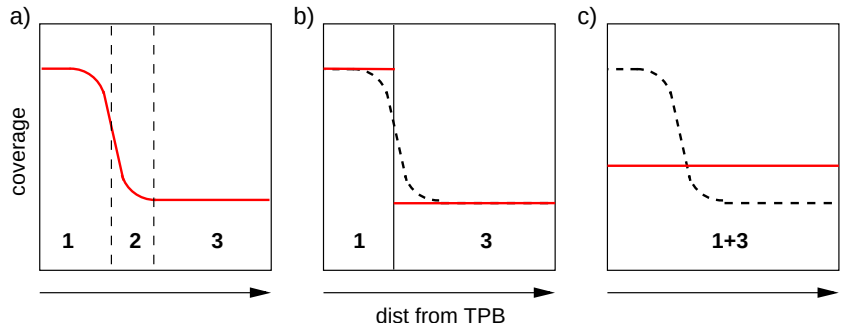

Figure 3.7: *Schematic representation of the different modelling approaches. The left border represents the TPB. a) Full reaction-diffusion model: The charge-transfer reaction is assumed to occur as "line reaction". b) Confined-region charge transfer: Confinement of charge-transfer reaction to a region close to the TPB introduces transport-like behaviour. c) Fully-spreaded charge transfer: Species production due to charge transfer occurs over the complete surface area.*

where only heterogeneous chemical reactions take place. This is illustrated in Fig. 3.7. Each surface (Ni and YSZ) is divided into two regions without species exchange through surface diffusion. Fig. 3.8 shows the simulation results using this reduced model for two CT mechanisms (H1+H2 and O1+O2). The confined region CT approach yields qualitatively the same results as the the full model. In the "fully-spreaded" charge transfer model, each surface (Ni and YSZ) is represented by one single region extending over the complete surface area. Species fluxes due to spillover reactions occurring at the TPB are assumed to be distributed over the complete available surface area. This corresponds to the assumption of infinitely fast diffusion. The results for this model are shown in Fig. 3.9. They are notably different from the results of the full model and the "confined-region" model. For the H1+H2 CT mechanism, the anodic Tafel slope is lower. Furthermore, for both CT mechanisms, the Tafel plots do not show a cathodic limiting current anymore. The results shown here indicate that the coupling of reaction with slow diffusion processes needs to be included in the models, either through a full reaction-diffusion approach or through a "confined-region" assumption.

3.5.4 Apparent Tafel slopes and rate-limiting steps

From electrochemical theory it follows that if a CT reaction was the rate limiting step the Tafel plot showed exponential behaviour for higher overpotentials. In Fig. 3.10 we compare the current-voltage curves for three different cases: (A) no water dissociation on YSZ (Tab. 3.2, Reaction 2), an approach previously employed by Goodwin [74]. (B) present work. (C) spreaded CT model where reactants and products of the CT reaction are spread all over the surface. The latter corresponds to the present work disregarding surface

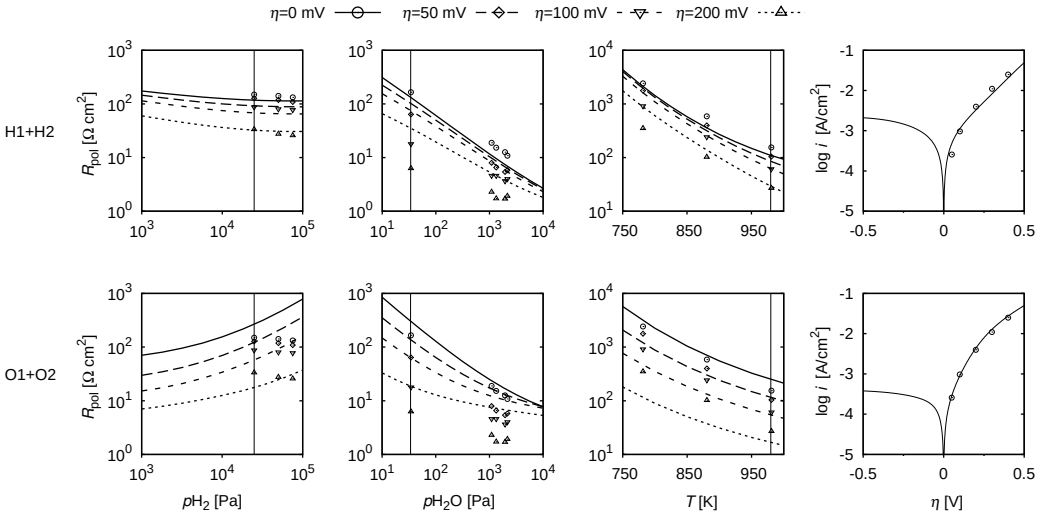

Figure 3.8: *Confined-region charge transfer model: Polarisation curves and charge-transfer resistances for double hydrogen spillover (cf. Fig. 3.1a) with* $d_{\mathrm{YSZ}} = 60$ nm,$d_{\mathrm{Ni}} = 10$ μm *and double oxygen spillover (Fig. 3.1b) with* $d_{\mathrm{YSZ}} = 10$ μm,$d_{\mathrm{Ni}} = 70$ nm.

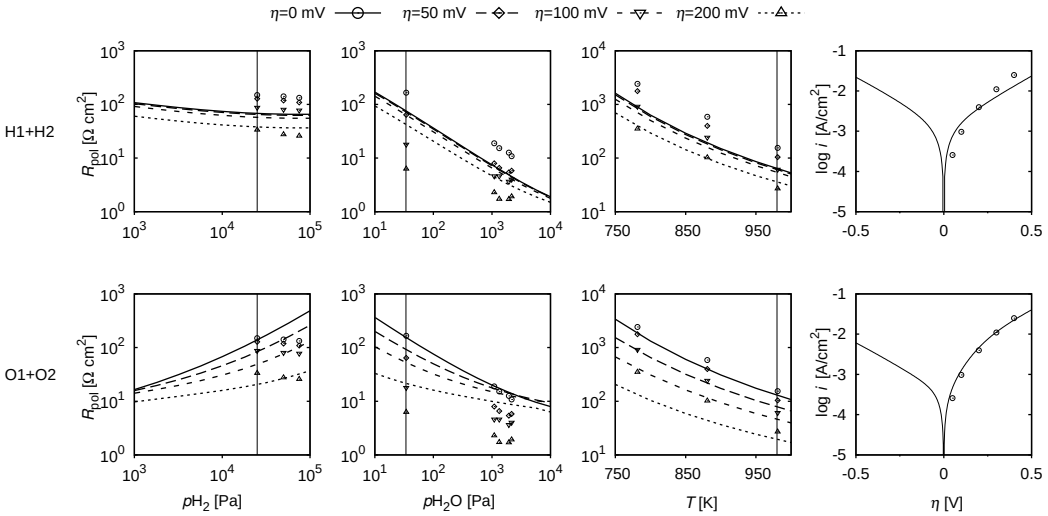

Figure 3.9: *Fully-spreaded charge transfer model: Polarisation curves and charge-transfer resistances for double hydrogen spillover (cf. Fig. 3.1a) and double oxygen spillover (Fig. 3.1 b).*

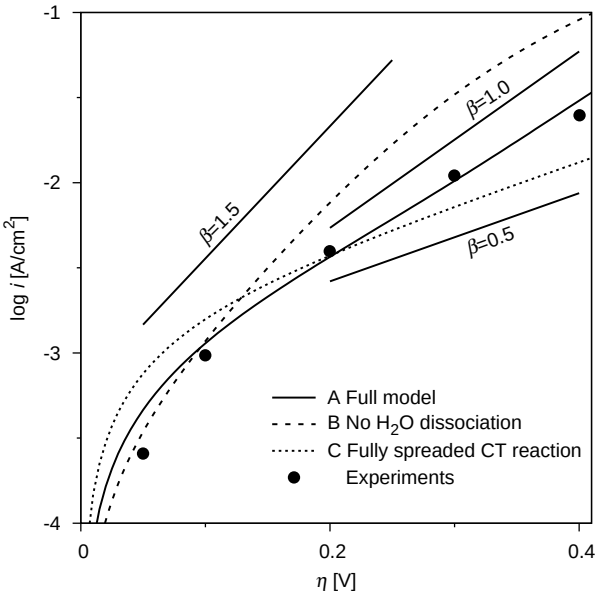

Figure 3.10: *Comparison of Tafel slopes for double hydrogen spillover (Fig. 3.1 a) at different model assumptions. A. Full reaction-diffusion model without* H_2O *dissociation on YSZ (Fig. 3.4). B. Full reaction-diffusion model (Fig. 3.3). C. Fully spreaded charge transfer model (Fig. 3.9). The numbers indicate the Tafel slopes.*

transport or to systems where surface transport is fast compared to other processes. The lines in the figure are labelled with the apparent Tafel slope $\beta \cdot {}^{(RT)}/_{F}$. The transfer coefficient β of the experimental data is close to unity which is in very good correspondence with our model predictions, whereas the simulations (A) and (C) predict too high or too low apparent Tafel slopes.

3.5.5 Interstitial charge transfer

During the interstitial charge-transfer reaction (Fig. 3.1 d), hydrogen from the gas phase (H_2) is being dissociatively adsorbed on the nickel surface and incorporated into the nickel bulk phase as an interstitial hydrogen atom (H^{x}_{iNi}). In the bulk nickel it diffuses to the interface area between the electrolyte and the electrode. At this 2D interface, the interstitial hydrogen atoms are transfered into interstitial protons ($H^{\bullet}_{iYSZ}$) in the electrolyte bulk, leaving their electrons in the electrode. The interstitial protons in the bulk electrolyte diffuse underneath the electrode to the uncovered electrolyte surface where they combine with surface adsorbed hydroxyl ions to form water which then desorbs into the gas phase.

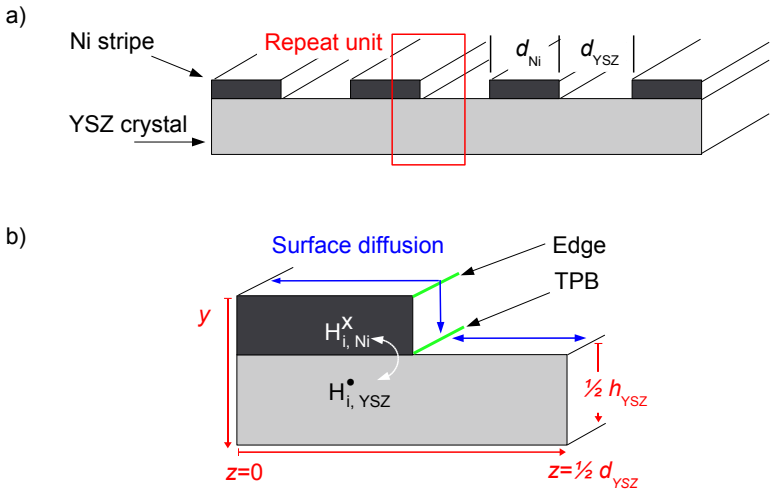

Figure 3.11: *Sketch of the modelling domain for simulations of interstitial hydrogen transfer.*

Model assumption. The calculations in this section are based on the same model assumption as described in Sec. 3.3, differing only in the assumed charge-transfer reaction. The surface-spillover reactions are now disabled and the charge-transfer takes place via the bulk-bulk interchange reaction. The model was extended to allow for a two-dimensional diffusion of the interstitial species and two bulk-surface exchange reactions. (Reactions No. 3 and 10 in Tab. 3.2). Figure 3.11 shows a sketch of the modelling domain. Surface diffusion is treated by the surface-adapted Fickian approach described previously for the top surfaces of both, the electrode and the uncovered electrolyte as well as on the vertical surface of the electrode stripe. The nickel-adsorbed species are assumed to diffuse "round the edge" as if it was a flat surface. The transport in the bulk electrode and bulk electrolyte is assumed to result only from gradients in the chemical potential thereby neglecting possible influences of electrical potentials on the diffusive flux of the charged interstitials. For the electrode, a very well conducting metal with a cross-section of about 1x10 microns this is a very good approximations as no gradient in the electrical potential is expected. For the electrolyte with its low conductivity the impact of this simplified approach may be more severe, especially for high currents. For the correct description of the bulk diffusion in the YSZ bulk material a detailed modelling of the electrical potential inside the electrolyte would be necessary (e.g., the formation of charged complexes and electrical double layers) which is beyond the scope of this thesis. However, assuming the chemical instead of the electrochemical potential to be the driving force of the bulk diffusion has no influence on the general validity of the model; it only quantitatively affects the diffusivities of the interstitial species.

Boundary conditions. Zero-flux boundary conditions for the interstitial species are assumed at $z = 0$, $z = {}^1/_s d_{\mathrm{YSZ}}$ and the center of the electrolyte layer, $y = {}^1/_2 (h_{\mathrm{YSZ}} + h_{\mathrm{Ni}})$.

Model parameters. The diffusion coefficients for the interstitial species are taken from literature (see Tab. 3.3). The molar enthalpy and entropy of the interstitial hydrogen species were derived from fits to solubility measurements of hydrogen in nickel and YSZ at different temperatures (for details see Appendix A). The kinetic parameters for the bulk-surface exchange reactions are, in analogy to the oxygen exchange reaction, estimated from bulk diffusion parameters and are listed in Tab. 3.2.

Results on polarisation resistance and IV curves. For the standard parameter set no agreement between experiment and simulation could be achieved. The pre-exponential factor for the charge transfer reaction $k^0_{\mathrm{H-Int}}$ and the diffusion coefficient of bulk hydrogen in YSZ $D^0_{\mathrm{H}^\bullet_{\mathrm{i}}\mathrm{YSZ}}$ had to be adjusted so the simulation results agree best with the experimental data. The values are given in Tab. 3.6. The resulting dependencies of the polarisation resistance on variation of the partial pressures of hydrogen, water and temperature are shown in Fig. 3.12. The results show that the interstitial hydrogen transfer reproduces the experimental trends well. The polarisation resistance hardly changes with the variation of hydrogen partial pressure. The dependence on the partial pressure of water gives the same trend as found in the experiment and the same holds for the temperature dependence. The current-voltage relation is very close to the theoretical predictions from the Tafel equation at high overpotentials, indicating the CT reaction as rate-determining step. As in all investigated cases the cathodic branch of the IV curve shows a limiting current due to the slow diffusion of the interstitial protons in the bulk electrolyte. The dependence of the polarisation resistance on the overpotential shows good qualitative agreement.

Species distribution in the bulk material. Figure 3.13 shows the spatially resolved activities a_i of the interstitial species in the bulk materials of the electrode and the electrolyte for polarisations of ±300 mV. The activation is defined as the actual molar concentration of a species normalised to its solubility limit, $a_i = {}^{c_i}/_{c_{\max}}$. The panel a) and b) in Fig. 3.13 correspond to the Ni electrodes, the panel c) and d) to the electrode bulk according to the sketch of the modelling domain in Fig. 3.11 b). Areas coloured white have concentrations equal to the value at thermodynamical equilibrium (open circuit), red areas show a decrease and blue areas an increase in concentration relative to open circuit. The concentration profile shown in Fig. 3.13 clearly show that the concentration throughout the electrodes hardly changes if current is drawn. Only very close to the TPB (right bottom corner of panel a) and

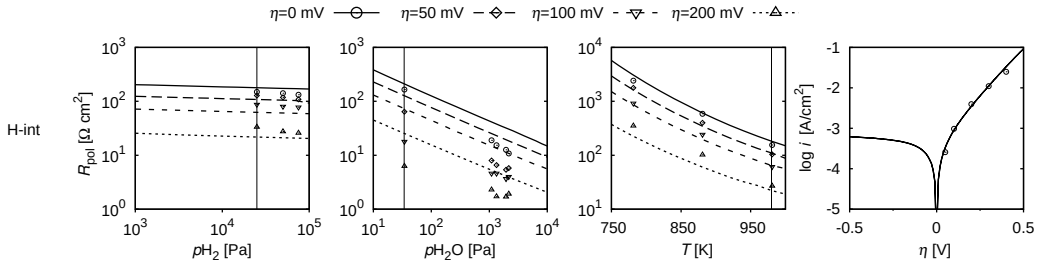

Figure 3.12: *Polarisation resistances and Tafel plot for the interstitial hydrogen transfer (see Fig. 3.1 d) and Tab. 3.6) based on the full reaction-diffusion model including bulk transport. The four graphs show the dependence of the polarisation resistance on hydrogen partial pressure, water partial pressure and temperature, as well as a Tafel plot. The vertical lines represent standard conditions (Tab. 3.5).*

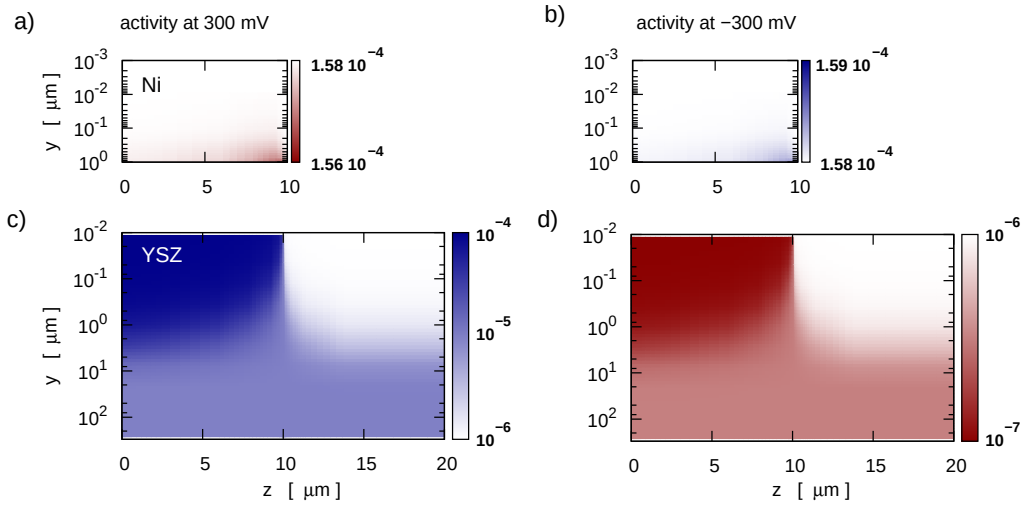

Figure 3.13: *Activity of interstitial species in the bulk electrolyte (b,d) and bulk nickel (a,c) for polarisations of ±300 mV.*

b) in Fig. 3.13) shows very small (below 1%) variation under polarisation. This is due to the small thickness of the electrode layer, a relatively hight diffusion coefficient compared to the interstitial hydrogen in the YSZ and the fact that hydrogen enters the bulk electrode not only via the top surface but also via the surface perpendicular to the electrolyte at $y = 10$ μm. The fast bulk-surface exchange at the top and vertical surface of the electrode stripe keeps the outermost bulk layers close to thermodynamical equilibrium with the gas phase. The concentrations in the bulk electrolyte however show variations of more than two orders of magnitude. The concentration far away from the TPB and close to the uncovered electrolyte surface are close to the values at thermodynamical equilibrium. This results from a fast bulk-surface exchange reaction which equilibrates the bulk with the gas phase. The concentration in the electrolyte underneath the middle of a nickel stripe (top left corner of the panels c) and d) in Fig. 3.13) are far away from the thermody-

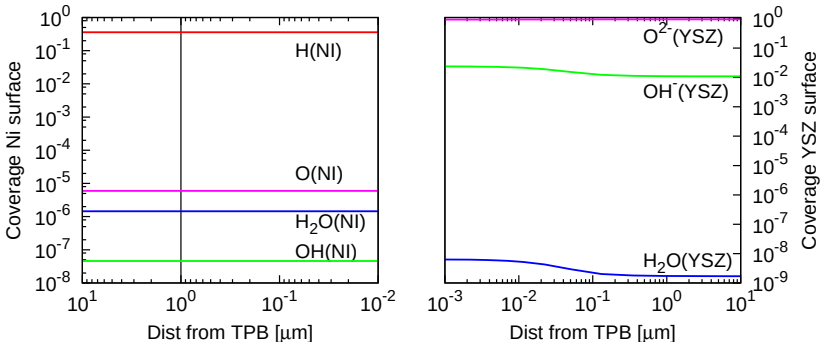

Figure 3.14: *Coverage of surface adsorbed species versus the distance from the TPB for the electrode (left) and the electrolyte (right) at a anodic polarisation of 300 mV. The vertical line indicates the edge of the electrode stipe. The part left of the edge is parallel to the electrolyte surface, the part right of the edge is perpendicular to the YSZ surface.*

namic equilibrium as no exchange with the surface is possible. Due to the no-flux conditions at the borders of the repeat unit the concentration inside the electrolyte increases with respect to open circuit conditions even at large distances ($y \approx {}^1\!/_2 h_{\mathrm{YSZ}}$) from the electrochemically active Ni/YSZ interface. The results for anodic and cathodic polarisation are similar; they show the same trends with opposing signs and, due to the lower overall current, a smaller variations between open circuit and the system under load.

Species distribution and fluxes on the surfaces. The surface coverages of electrode and electrolyte for an anodic polarisation of +300 mV are shown in Fig. 3.14. The nickel surface shows no noticeable change in coverage whereas on the YSZ surface the product species $\mathrm{OH}^-_{\mathrm{YSZ}}$ and water increase close to the TPB. Far away from the TPB the coverages of all species converge to their respective values at thermodynamical equilibrium. This is consistent with the distribution in the bulk. Figure 3.15 shows the fluxes over the surface of the horizontal and vertical surface of the nickel stripe (panel a), the fluxes over the uncovered electrolyte surface and the flux over the bulk-bulk interface via the CT reaction leading to the following insights:

- The rate of the protons being transferred from the bulk nickel to the bulk YSZ has a strong maximum close to the TPB (Fig. 3.15 c), where about 80% of current is generated by the CT reaction within 1 μm distance from the TPB.
- Most of the hydrogen needed for the CT reaction is supplied via the vertical nickel surface close to the TPB.
- The activity of the nickel surface shows a pronounced minimum close to the edge of the nickel stripe. This results from the configuration of the hydrogen sources distributed over the whole surface area and a

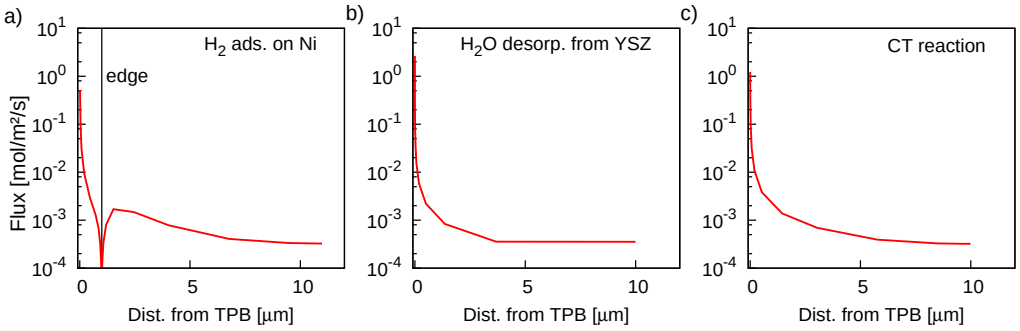

Figure 3.15: *Fluxes via the electrode/gas-phase (a), electrolyte/gas-phase (b) and electrode/electrolyte (c) interfaces at* $\eta = 300$ mV. *The vertical line in panel a marks the edge of the nickel stripe.*

point-like sink for protons close to the TPB. This two-dimensional geometrical configuration results in two optimal points for adsorption and incorporation of hydrogen. The first being close to the sink which keeps diffusion paths small, the second, indicated by the maximum at about 8 μm. Consequently the surface close to the edge is an unfavourable for hydrogen incorporation, hence the minimum in surface activity at $z = 2$ μm.

- The surface of the YSZ electrolyte shows high activity close to the TPB which decreases with increasing distance to the electrochemically active region.

- Although the fluxes over the interfaces show pronounced maxima close to the TPB the whole are of all interfaces is active; for the nickel electrode the horizontal surface account for about 30% of the total amount of hydrogen needed for current generation.

Conclusion. The presented agreement between simulation and experiment could only be achieved by increasing the diffusivity of interstitial hydrogen in YSZ bulk by about two orders of magnitude. Given the simplification inflicted on the transport process (no grain boundary diffusion is included, neglecting of complex-formation inside the YSZ bulk, neglecting of the electrical potential when assessing gradients for diffusion), this uncertainty is within the a physically meaningful range.

A non-zero hydrogen concentration inside the bulk electrolyte and a finite mobility of $H^{\bullet}_{i\,YSZ}$ would cause the protons to proceed to the cathode side where usually low concentrations of water and hydrogen are present. Assuming the cathode gas was dry (pure oxygen, 0% water) a very low concentration of interstitial hydrogen would follow for the bulk electrolyte close to the cathode surface. This would result in a concentration gradient inside the electrolyte from the concentration at thermodynamical equilibrium at the anodic side to

approximately zero close to the cathode surface. If we assume purely diffusive transport, an electrolyte thickness of one mm (h_{YSZ}=1 mm) and a surface area of 1 cm^2 a rate of about 20 $^{\mathrm{pmol}}/_{\mathrm{s}}$ would result; this quantity that should be detectable in the cathode "exhaust" gas after allowing an accumulation time of several hours but not in the current or open circuit voltage as the leaking current due to "short-circuiting" of the cell over the protonic current would be in the range of μA.

3.6 Discussion

3.6.1 Electrochemistry of hydrogen oxidation on Ni anodes

Of all investigated CT mechanisms based on surface-spillover, only one yielded qualitative agreement over all experimental conditions, that is, the hydrogen spillover mechanism H1+H2. The fitted charge-transfer kinetics shows a relatively high activation energy of 174 kJ/mol. This high value is not expected for a reaction involving a light species as the hydrogen atom, but may be explained with the probably unfavourable geometry of the phase boundary at an atomic scale. Quantum chemical calculations have estimated an activation energy of 140 kJ/mol [76]. The fitted diffusion coefficients are within the estimated uncertainty of the literature values.

Simulations as well as experiments show a strong dependence of electrode kinetics on gas-phase H_2 and H_2O partial pressures. As shown by Bessler et al. [27], this is because the resulting change of the equilibrium (Nernst) potential directly alters charge-transfer kinetics. The present results based on a full reaction-diffusion model show the same qualitative trends as the simplified model where charge transfer was assumed to be the only rate-determining step [27] and thus fully support their interpretation. Thus, although in the full model charge transfer is only rate co-determining, it represents the dominant cause of the gas-concentration dependence. In this context it should be noted that the main criterion favouring hydrogen spillover over oxygen or hydroxyl spillover mechanisms is their different dependence on H_2 partial pressure.

3.6.2 Apparent Tafel slopes

The experimentally observed apparent transfer coefficient β is around 1 (Fig. 3.10; note that the experiments do not show an extended linear region in the Tafel plot). This is considerably larger than what would follow from system dominated by one single charge-transfer reaction, yielding $\beta = {}^1/_2$. The simulation results reveal two possible reasons for a larger overall Tafel slope. Firstly, coupling of charge transfer to another rate-determining process

(diffusion or surface reaction) can cause an increase of the Tafel slope. This is evident when comparing the full model (Fig. 3.10 A) with fully-spreaded charge-transfer model (Fig. 3.10 B). In the latter case, the complete surface area is available for reaction, and there is no co-determining process apart from the charge-transfer reaction. This results in a simulated transfer coefficient $\beta = 1/2$, corresponding to the electrochemical theory. Secondly, it can be shown analytically that two sequential (consecutive) symmetrical charge-transfer steps cause an overall anodic transfer coefficient of $\beta = 3/2$ if the second step is rate-determining [30]. This is evident when further comparing with the results obtained without H_2O_{YSZ} dissociation (and, consequently, without the reverse reaction, $OH^-_{YSZ} + O^{2-}_{YSZ}$ recombination) (Fig. 3.10 A). In the latter case, H_2O_{YSZ} formation *must* occur through both consecutive hydrogen spillover reactions (H1 and H2), resulting in $\beta = 3/2$. When H_2O_{YSZ} dissociation is active and sufficiently fast, either one of the hydrogen spillover reactions (H1 or H2) is sufficient, resulting in lower Tafel slopes.

This discussion reveals an important ambiguity concerning the interpretation of polarisation behaviour: The observation of Tafel behaviour does not necessarily imply a charge-transfer-limited reaction, and observed Tafel slopes of $> 1/2 \cdot (RT)/F$ do not necessarily mean the presence of consecutive charge-transfer steps. In the present study, this leads to an ambiguity concerning the anode mechanism: Qualitatively identical results where obtained from the H1+H2 pathway by either assuming slow surface diffusion and including H_2O_{YSZ} dissociation into the mechanism, or by assuming fast surface diffusion and excluding H_2O_{YSZ} dissociation. Both assumptions are chemically reasonable and may be argued for. A key experiment for clarifying this issue would be the measurement of H_2O dissociation over YSZ surfaces, for example using isotope labelling studies.

3.6.3 Recommendations for further studies

We have compiled here a complete set of model parameters for the Ni/YSZ system which can be readily used for further studies. However, the surface diffusion coefficients still are order-of-magnitude estimates and the kinetics of the heterogeneous surface chemistry on the YSZ is not sufficiently validated. In this respect, this study can give directions as to which theoretical and experimental investigations should be performed in future in order clarify the mechanistic details of the hydrogen oxidation reaction at SOFC anodes.

(1) The high sensitivity of the simulation results towards a variation of thermodynamic data and diffusion coefficients shows the need for a reliable data base. More detailed information about the thermodynamic, kinetic and transport data of species and reactions need to be obtained in particular on the YSZ surface. This is possible with experiments from the surface science and materials science context (e.g., thermogravimetry, temperature-programmed

desorption, *in situ* surface optical spectroscopy such as infrared reflection-absorption spectroscopy and sum frequency generation, isotope exchange studies) and with theoretical approaches (e.g., quantum chemical calculations with density-functional theory, molecular dynamics simulations).

(2) The charge-transfer on the reactive electrolyte pathways (Fig. 3.1 e) was not included in this study and should be additionally treated in quantitative modelling studies.

(3) Experimental data is available only for a limited range of operating conditions. In particular, no experiments where performed under cathodic polarisation, and water partial pressure was only varied over a small range. Furthermore, the experimental data show considerable sample-to-sample variation (cf. Tab. 3.4). We believe that additional electrochemical experiments with model anodes are required, including a careful validation of reproducibility. Especially SiO_2-free reaction chambers in combination with single crystal electrolytes are desirable in order to eliminate the experimentally proven SiO_2 contaminations at Ni/YSZ three-phase boundaries [21, 116, 117]. The measurements should include pre-test, post-test and, if possible, in situ analysis of potential impurity segregation and structural integrity.

3.7 Conclusions

We have presented a quantitative elementary kinetic modeling study of the hydrogen oxidation reaction at Ni/YSZ patterned anodes. The model describes the coupling of surface reactions and surface diffusion with charge transfer through spillover reactions. It allows the prediction of macroscopic electrode behaviour as well as its interpretation in terms of rate-determining processes. Results were compared to patterned anode experiments published before. The main conclusions are summarised as follows.

- An extensive set of thermodynamic, kinetic, and transport parameters was compiled from various literature sources, forming the base for elementary kinetic modeling approaches.
- Calculations were performed for seven different charge-transfer mechanisms, including various combinations of hydrogen spillover, oxygen spillover, and hydroxyl spillover reactions. Only a mechanism involving two spillover reactions of hydrogen from the Ni surface to oxide ions and hydroxyl ions on the YSZ surface (Fig. 3.1a, reactions H1 and H2) yielded agreement with the complete experimental data set.
- A sensitivity analysis revealed four rate-determining processes for this mechanism: Hydrogen spillover to oxide ions, water association on YSZ, water desorption from YSZ, and surface diffusion of YSZ-adsorbed hydroxyl ions.

- Gas-phase H_2 and H_2O concentrations have a strong influence on electrode kinetics through a variation of the equilibrium (Nernst) potential.
- Surface diffusion is a key process contributing to the electrochemical behaviour at the three-phase boundary. The electrochemically active surface area is confined to narrow widths <100 nm from the TPB, resulting from the interaction of fast surface reactions with slow surface diffusion. Surface concentrations close to the three-phase boundary are predicted to differ from thermodynamical equilibrium by up to 2 orders of magnitude.

The investigations furthermore allow to establish recommendations for further investigations. Beside the need for reliable and more detailed experimental data, a thorough refinement of the parameters used in this work is required to improve quantitative model predictions over a wider range of conditions. A continued concerted effort of theory and experiments is proposed in order to unambiguously elucidate the mechanism of the hydrogen oxidation reaction at SOFC anodes.

Chapter 4

Direct flame fuel cell

4.1 Introduction

In the course of designing fuel cells for specific applications, there is always a trade off between efficiency, ease of handling, fault tolerance and cost. As increasing the efficiency is –in most cases– related to a more efficient conversion of the fuel, it is at the expense of system complexity. This drives up the costs and makes the system more prone to errors and less stable. Yet increasing efficiency can as well mean reducing the system complexity and thus creating a simple, cheap and easily set-up device. As solid oxide fuel cells (SOFC) are very tolerant in matters of fuel, temperature, pressure and to some extent sulfur content, they are a good base to develop such an as-simple-as-possible energy conversion device.

The driving force for energy conversion in a fuel cell is a gradient in the chemical potential of the oxidant and/or the fuel. To establish this gradient the anode and cathode gas streams are usually separated from each other. This makes the system complex. Even if no fuel processing is necessary, high temperature sealing techniques are needed and means of thermal management have to be built into the system. The separation of gas streams may be omitted by using specialised catalyst materials for the anode and cathode, making them selectively catalysing either the fuel or the oxidant. These systems are known as single chamber fuel cells and have been widely investigated [118–120]. But still, these systems are kept inside a chamber and some effort has to be made to constantly supply heat and fuel. Consequently one could think of an even simpler fuel cell setup if one was to find an environment where gradients in oxygen concentration and high temperatures are an inherent feature. Yet nowadays, when heat is usually produced by the combustion of hydrocarbon fuels, such an "environment" is found literally everywhere. In such a "no-chamber" setup the chemical gradient will be built up by a fuel-rich combustion of a hydrocarbon fuel on the anode side of the SOFC where the combustion process consumes nearly all of the oxygen and additionally

acts as a fuel reformer and heat source for the SOFC. The SOFC would run on excess hydrogen and CO from the combustion; therefore the flame would have to be slightly fuel rich at least. Using rich flames for fuel conversion and heat supply for SOFCs was demonstrated by several authors [121–123] mostly using catalytic combustion. Applying this idea to a freely burning flame was first published by Horiuchi et al. and named "direct flame fuel cell" or DFFC [124]. There are a number of advantages to this approach:

- Fuel versatility. Because intermediate flame species are very similar for all kinds of hydrocarbon fuels (mostly partially oxidised C_1 and C_2 species, hydrogen and water), the DFFC is very fuel-flexible. Horiuchi et al. demonstrated electrochemical power generation from exhaust gases of various gaseous, liquid, and solid fuels [13, 124].
- Simple setup. The anode is simply placed into the exhaust gases of a flame, and the cathode breathes ambient air.
- Rapid start-up. The flame heat release brings the fuel cell rapidly to its operating temperature.

However, also a number of drawbacks are associated with the DFFC type setup:

- Low efficiency. An inherent property of the DFFC is that a part of the fuel's chemical energy is consumed in the flame and is therefore not available to generate electrical power. This reduces the overall electrical efficiency.
- Materials stress. The operating environment of a flame induces significant thermal stress to the SOFC. This may lead to a rapid degradation of fuel cell performance or even fractures.

Clearly, the DFFC system will not be suitable for large-scale power production. There are, however niche markets where it could offer the ideal , including powering small electrical devices with low power consumption as they are used for controlling combustion processes of central heating or with gas-driven off-grid devices like refrigerators, gas stoves or independent vehicle heaters. It may even be used to produce electricity from engine exhausts [14]. The investigation was part of a collaborative project between H. Kronemayer and D. Barzan from the PCI in Heidelberg responsible for the experimental characterisation, M. Horiuchi inventor of the DFFC idea and contact person from Shinko Electric Industies Co. Ltd. , who is the industry partner and funder of this research project responsible for microstructural characterisation and cell production. Our research group was responsible for modelling and data analysation. Before and during the course of the project a number of publications where put forth on the proof of concept [13, 124], the experimental characterisation [125] and modelling results [126].

In the remainder of this Chapter we will develop a computational model for the DFFC system and perform a parameter optimisation based on model predictions. We will first set up a detailed model (Sec. 4.2.1 and Sec. 4.2.2) comprising all relevant physical processes governing the system performance. In the following simulation targets will be specified (Sec. 4.3) which will allow us to validate our model predictions against experimental data (Sec. 4.4.3). The model will then be used to find optimal working conditions and design parameters in Sec. 4.4.5.

4.2 Model

Kronemayer et al. electrochemically characterised the DFFC system for three hydrocarbon fuels (methane, propane and butane) applying different fuel-to-air ratios and gas outflow velocities. In the experiments a SOFC was placed in the exhaust of a flame-flame burner. Once the system reached steady state, current-voltage curves were measured by drawing current from the fuel cell. The experiments identified the cell temperature to be of key importance for the system and stated that the cell voltage depends almost linearly on the current [125]. The power density was found to have a maximum at around 900 K independent of the fuel used but strongly coupled to the temperature. Figure 4.1 shows the experimental setup (a) along with a sketch of the modelling domain (b). Experimentally only the cathode temperature and the current-voltage relation (IV curve) of the fuel cell were accessible, whereas important parameters for the prediction of fuel cell performance are the gas compositions of anode and cathode, the temperature distribution throughout the cell as well as material related parameters of the fuel cell (e.g. resistivities of the used materials, porosity of the electrodes, etc.). Consequently the model has to comprise two main parts which we focus on in the remainder of this section: Firstly a geometrically constrained flame has to be modelled to determine gas-phase compositions and temperature at the surface of the fuel cell. Secondly the energy-conversion capabilities and the thermal management of the fuel cell have to simulated to predict the power output of the system. Depending on the focus of the analysis, different level of model detail will be used. Whenever possible the model complexity will be reduced to enable faster computation. To ensure adequate reproduction of crucial system properties the reduced models are compared to the results of the full model. In this Section we the full model which accounts for all the relevant processes governing the system performance will be developed. Details on the model reductions will be given in Section 4.4. A summary of the governing equations is given in Tab. 4.1 at the end of this Section.

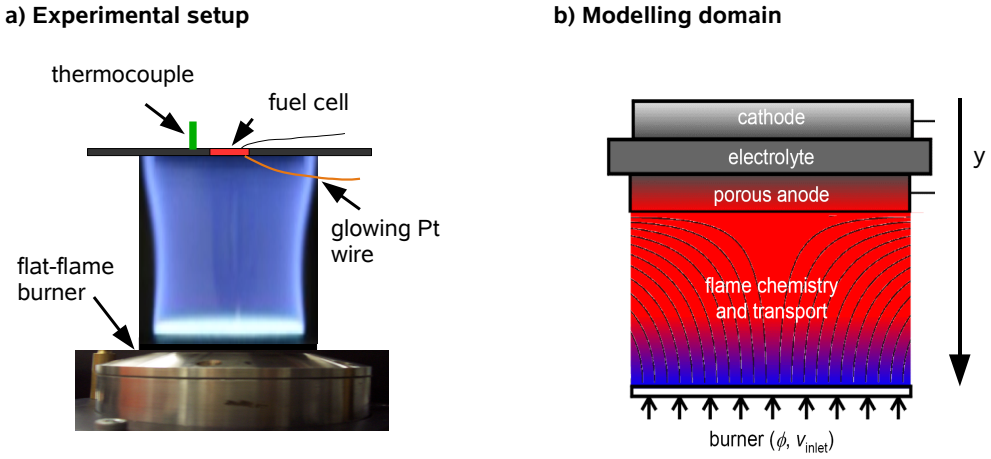

Figure 4.1: *Experimental setup and modelling domain.*

4.2.1 Gas phase

In the experimental setup a flat-flame burner was used to produce a laminar burner-stabilised flat flame with a diameter of 45 mm at the anodic side of the SOFC. The SOFC with a diameter of 13 mm was centred over the burner matrix. Methane and ambient air with mass flows $\dot{m}_{CH_4}$ and $\dot{m}_{air}$ are mixed in the mixing chamber of the burner to yield different equivalence ratios ϕ. The equivalence ratio $\phi = {}^{r}/_{r_{stoich}}$ is defined as the ratio of fuel to oxidiser flow rates $r = {}^{\dot{m}_{fuel}}/_{\dot{m}_{Ox}}$ to the stoichiometric ratio r_{stoich}. After ignition a stable flame develops between the burner and the SOFC. As the spatial dimension of the fuel cell is small compared to the flame diameter, a reactive non-isothermal stagnation point flow is assumed (Eq. 4.1-4.6). This assumption allows to use a exact solution of the Navier-Stokes equations in 1D which accounts for the full coupling of heat and mass transport in the anode gas phase. Although this assumption is strictly valid only for very small distances between burner outlet and fuel cell it was used because of its simplicity which enabled us to use detailed reaction mechanisms for the combustion chemistry. The combustion chemistry is described by a set of homogeneous gas-phase reactions consisting of 220 reactions between 36 species (see Appendix B.2.1). This mechanism was compiled based on GRI-Mech 3.0 [127], a mechanism optimised for the simulation of natural gas combustion. The use of methane instead of natural gas allows the restriction of the reaction mechanism to cover hydrocarbon species smaller than C_3H_4 [54]. For the cathode a constant non reactive gas atmosphere of $N_2 : O_2 = 79 : 21$ was assumed. The pressure was set to $p_{tot,std} = 1$ bar.

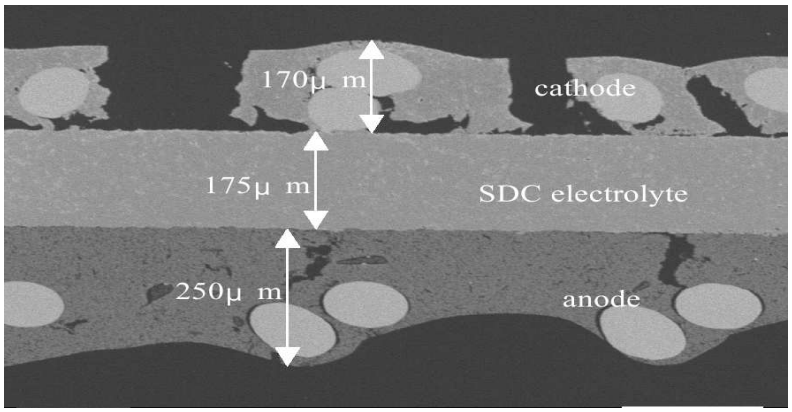

Figure 4.2: *Cross-section of the SOFC used in the experiments from Kronemayer et al. Picture courtesy of Shinko Electric Industies Co. Ltd. .*

4.2.2 Fuel cell

Electrolyte. According to the manufacturer Shinko Electric Industies Co. Ltd. , the electrolyte used in the experiments from Kronemayer et al. was prepared from a samarium-doped ceria (SDC, $Ce_{0.8}\,Sm_{0.2}\,O_{2-\delta}$) of 175 μm thickness and a diameter of 13 mm. After firing at 1300 °C for 5 hours a dense SDC layer is formed (Fig. 4.2), consequently there is no gas transport within or through the electrolyte.

Over the whole range of experimental conditions SDC is a mixed ionic and electronic conductor offering two parallel pathways for charge transport: Transport of ionic charge by movement of oxygen vacancies through the lattice structure and charge transport by electrons in the conduction band. In both cases a direct proportionality of voltage and current is assumed. The constants of proportionality, the ionic and electronic resistivity, are functions of temperature (Eq. 4.39, 4.40). The temperature dependence of the ionic conductivity was measured by the cell manufacturer using AC impedance measurements in air between $500 - 770$ K. For the electronic conductivity as well as additional data for the ionic conductivity at higher temperatures fits of Eq. 4.39 and Eq. 4.40 to published experimental data were performed (Appendix B.1). The overall ohmic loss in the electrolyte is calculated from the sum of electronic and ionic current (Eq. 4.37). The dense electrolyte has a very small surface compared to the porous structure of the electrodes. We therefore treat the electrolyte as chemically inactive.

Electrodes. The cathode and anode were screen-printed onto the electrolyte disc. The cathode paste consisted of a 1:1 weight-ratio-mixture of SDC and SSC (samarium strontium cobaltite, $Sm_{0.5}\,St_{0.5}\,CoO_3$). The anode paste was a mixture of 5 wt% Rh_2O_3, 57 wt% of 8 mol%-Li-doped NiO and 38 wt% SDC. Platinum meshes with attached platinum wires were embedded

in the pastes for current collection. After assembling the cell was fired for one hour at 1200 °C. Fig. 4.2 shows a micrograph of the cross-section of the MEA structure as fabricated.

The electrodes consist of three phases: the porous gas phase and the two solid phases of the mixed-conducting electrolyte and electronically conducting electrode. The intersection of the three phases form the three phase boundary (TPB). The electrode microstructure is designed highly porous to obtain a high surface-to-volume ratio and for maximum performance. Chemistry within the electrode layers is dominated by surface effects. Therefore we treat the gas phase as chemically non reactive. Gas transport in the pores is described by coupled Stefan-Maxwell multi-component diffusion and Darcy porous flow (Eqs. 4.7-4.12). A detailed elementary kinetic model is used to describe the heterogeneous surface chemistry (Eq. 4.13). The reaction mechanism used to calculate the chemical source terms for the electronically conducting phase of the anode was developed for partial oxidation of methane on nickel surfaces [128]. It consists of 42 reactions between 6 gas-phase species and 12 surface species (see Appendix B.2.2). As the reaction mechanism for the heterogeneous chemistry on the surface of the anodic mixed-conducting phase is unknown, the reaction mechanism developed for YSZ (Tab. 3.2 No. 1,2,4) is used.

The charge transfer reactions (CTR) on anode and cathode are assumed to take place at the TPB distributed over the whole volume of the electrodes. Two different approaches were used: For the anode the elementary kinetic approach developed in Ch. 3 is applied using the H1 CT mechanism (Eqs. 4.23-4.26). For the cathode we make use of the modified Butler-Volmer ansatz (Eqs. 4.27-4.28) developed by Zhu et al. [35].

The modelled aspects of the thermal management of the fuel cell comprise the heat production by heterogeneous chemistry in the anode, joule heating in the whole fuel cell, heat conduction through the entire SOFC as well as radiative and convective heat transport at the electrode surfaces (Eqs. 4.14-4.17).

Connecting wires. In the experiments the SOFC was connected via a platinum wire to the measuring device. The wire had a diameter of 0.3 mm and a total length of $l_{\text{con}} = 60$ cm. The wire was directly attached to the SOFC surface and assumed to have the same (high) temperature as the SOFC. The temperature dependence of this resistance is modelled via Eq. 4.42. If adds to the over all ohmic resistance of the system and will be shown to have large influence on the system.

Summarised model equations

Process	Model equation	Eq.
Reactive stagnation point flow		
Mass continuity	$\frac{\partial \rho}{\partial t} = -\frac{\partial(\rho v_y)}{\partial y} - 2\rho V$	(4.1)
Radial momentum	$\frac{\partial(\rho V)}{\partial t} = -\frac{\partial(\rho v_y V)}{\partial y} - \frac{\partial}{\partial y}\left(\mu \frac{\partial V}{\partial y}\right) - \rho V^2 - \Lambda$	(4.2)
Species conservation	$\frac{\partial(\rho Y_i)}{\partial t} = -\frac{\partial(\rho v_y Y_i)}{\partial y} - \frac{\partial j_i^{\mathrm{diff}}}{\partial y} + \dot{s}_i^V M_i$	(4.3)
Energy conservation	$\frac{\partial(\rho c_{\mathrm{P}} T)}{\partial t} = -\frac{\partial(\rho v_y c_{\mathrm{P}} T)}{\partial y} + \frac{\partial}{\partial y}\left(\lambda_{\mathrm{q}} \frac{\partial T}{\partial y}\right) - \sum_{i \in S_{\mathrm{g}}} c_{\mathrm{P},i} j_i^{\mathrm{diff}} \frac{\partial T}{\partial y} - \sum_{i \in S_{\mathrm{g}}} \dot{s}_i^V h_i$	(4.4)
Radial pressure	$\frac{\partial \Lambda}{\partial y} = 0$	(4.5)
Species production by homogeneous chemistry	$\dot{s}_i^V = \sum_m \nu_{i,m} \left(k_{\mathrm{f},m} \prod_{j \in R_{\mathrm{f},m}} c_j^{\nu_j'} - k_{\mathrm{r},m} \prod_{j \in R_{\mathrm{r},m}} c_j^{\nu_j''} \right)$	(4.6)
Porous gas-phase transport		
Mass transport	$\frac{\partial(\epsilon c_i)}{\partial t} = -\frac{\partial J_i^{\mathrm{diff}}}{\partial y} - \frac{\partial J_i^{\mathrm{flow}}}{\partial y} + \dot{s}_i^V$	(4.7)
Knudsen diffusion	$J_i^{\mathrm{diff}} = -c_i \overline{D_i} \frac{\partial X_i}{\partial x}$	(4.8)
Darcy flow	$J_i^{\mathrm{flow}} = -X_i c_{\mathrm{g}} \frac{B}{\mu} \frac{\partial p}{\partial y}$	(4.9)
Mixture averaged diffusion coefficient	$\overline{D_i} = (1 - X_i) \left(\sum_{j \in S_{\mathrm{g}}, j \neq i} X_j / D_{ij}^{\mathrm{eff}} \right)^{-1}$	(4.10)
Bosanquet diffusion coefficients	$D_{ij}^{\mathrm{eff}} = D_{ji}^{\mathrm{eff}} = \frac{\epsilon}{\tau} \frac{1}{2} \left(\frac{1}{1/D_i^{\mathrm{K}} + 1/D_{ij}} + \frac{1}{1/D_j^{\mathrm{K}} + 1/D_{ij}} \right)$	(4.11)
Kozeny-Carman relation	$B = \frac{\epsilon^2 d_{\mathrm{P}}^2}{72 \cdot \tau (1-\epsilon)^2}$	(4.12)
Volumetric gas-phase production rate	$\dot{s}_i^V = \sum_{k \in S_{\mathrm{N}}} A_k^V \dot{s}_i{}^A$	(4.13)
Heat transport MEA		
Energy conservation	$\frac{\partial(\rho c_{\mathrm{P}} T)}{\partial t} = \frac{\partial}{\partial y}\left(\lambda_{\mathrm{q}} \frac{\partial T}{\partial y}\right) + \dot{s_q}$	(4.14)
Heat sources	$\dot{s_q} = \sigma_{\mathrm{elyt}}^i \left(\frac{\partial \phi_{\mathrm{elyt}}}{\partial y} \right)^2 + \sum_{i \in S_{\mathrm{g}}, S_{\mathrm{s}}} \dot{s}_i^V h_i$	(4.15)
Heat transfer coefficient	$\alpha = Nu \cdot \frac{\lambda_{\mathrm{q}}^{\mathrm{air}}}{L_{\mathrm{char}}}$	(4.16)
Surface heat radiation	$j_q^{\mathrm{elec}} = \alpha \left(T_{\mathrm{elec}} - T_{\mathrm{gas}} \right) + \sigma_{\mathrm{SB}} \epsilon_{\mathrm{q}} \left(T_{\mathrm{elec}}^4 - T_{\mathrm{ref}}^4 \right)$	(4.17)

Process	Model equation	Eq.
Heterogeneous chemistry model		
Surface coverages	$\theta_i = \frac{c_i}{\Gamma_k}$	(4.18)
Chemistry source terms	$\dot{s}_i^{\mathrm{A}} = \sum_m \nu_{i,m} \left(k_{\mathrm{f},m} \prod_{j \in R_{\mathrm{f},m}} c_j^{\nu_j'} - k_{\mathrm{r},m} \prod_{j \in R_{\mathrm{r},m}} c_j^{\nu_j''} \right)$	(4.19)
Forward reaction rate constant	$k_{\mathrm{f},m} = k_{\mathrm{f},m}^0 \cdot T^{\beta_m} \cdot \exp\left(-\frac{E_{\mathrm{f},m}^{\mathrm{act}}}{RT}\right)$	(4.20)
Reverse reaction rate constant	$k_{\mathrm{r},m} = k_{\mathrm{f},m} \cdot \exp\left(\frac{\Delta G_m}{RT}\right)$	(4.21)
Gibbs free reaction enthalpy	$\Delta G_m = \sum_{i \in R_{\mathrm{f},m}} \nu_{i,m}' \left(h_i - T \cdot s_i\right) - \sum_{i \in R_{\mathrm{r},m}} \nu_{i,m}'' \left(h_i - T \cdot s_i\right)$	(4.22)
Electrochemistry anode		
Forward charge transfer reaction rate constant	$k_{\mathrm{f,ct}} = k_{\mathrm{f,ct}}^0 \exp\left(-\frac{E_{\mathrm{f,ct}}^{\mathrm{act}}}{RT}\right) \exp\left(\alpha \frac{zF}{RT} \cdot \Delta\phi_{\mathrm{an}}\right)$	(4.23)
Reverse charge transfer reaction rate constant	$k_{\mathrm{r,ct}} = k_{\mathrm{f,ct}} \exp\left(\frac{\Delta G_m}{RT}\right) \exp\left(-\left(1-\alpha\right) \frac{zF}{RT} \cdot \Delta\phi_{\mathrm{an}}\right)$	(4.24)
Total volumetric current	$i_{\mathrm{tot}}^V = \sum_{j \in \mathrm{CTRs}} i_j^V$	(4.25)
Faradaic current of single charge-transfer reaction	$i_{\mathrm{CTR}}^{\mathrm{V}} = zFl_{\mathrm{TPB}}^{\mathrm{V}} \left(k_{\mathrm{f}} \prod_{j \in \mathrm{R_{f,ct}}} \theta_j^{\nu_j'} - k_{\mathrm{r}} \prod_{j \in \mathrm{R_{r,ct}}} \theta_j^{\nu_j''} \right)$	(4.26)
Electrochemistry cathode		
Exchange current density	$i_{\mathrm{ca}}^0 = i_{\mathrm{ca}}^* \exp\left(-\frac{E_{\mathrm{cath}}^{\mathrm{act}}}{RT}\right) \left(\frac{p_{\mathrm{O_2}}^{\mathrm{ca}}}{p_{\mathrm{O_2}}^*}\right)^{1/4} \left(1 + \frac{p_{\mathrm{O_2}}^{\mathrm{ca}}}{p_{\mathrm{O_2}}^*}\right)^{-1/2}$	(4.27)
Faraday current cathode	$i_{\mathrm{ca}} = i_{\mathrm{ca}}^0 \cdot \left[\exp\left(\beta_{\mathrm{a}} \frac{zF}{RT} \eta_{\mathrm{ca}}\right) - \exp\left(-\beta_{\mathrm{c}} \frac{zF}{RT} \eta_{\mathrm{ca}}\right)\right]$	(4.28)
Electrical properties of the MEA		
Potential SOFC	$E(i) = \phi_{\mathrm{elde,cath}} - \phi_{\mathrm{elde,an}}(i)$	(4.29)
Potential steps anode	$\Delta\phi_{\mathrm{an}} = \phi_{\mathrm{elde,an}} - \phi_{\mathrm{elyt,an}}$	(4.30)
Potential steps cathode	$\Delta\phi_{\mathrm{cath}} = \phi_{\mathrm{elde,ca}} - \phi_{\mathrm{elyt,ca}}$	(4.31)
Overpotential	$\eta = \Delta\phi - \Delta\phi_{\mathrm{equil}}$	(4.32)
Potential distribution electrode	$\frac{\partial}{\partial y}\phi_{\mathrm{elde}} = 0$	(4.33)

Process	Model equation	Eq.
Potential distribution dense electrolyte	$\frac{\partial}{\partial y}\left(\sigma_{\mathrm{elyt}}\frac{\partial}{\partial y}\phi_{\mathrm{elyt}}\right)=0$	(4.34)
Potential distribution composite electrode	$\frac{\partial}{\partial y}\left(\sigma_{\mathrm{elyt}}f_{\sigma}\frac{\partial}{\partial y}\Delta\phi_{\mathrm{an}}\right)=-i_{\mathrm{tot}}^{\mathrm{V}}$	(4.35)
Total current	$i=\int i_{\mathrm{tot}}^{\mathrm{V}}\,dy+i_{\mathrm{el}}$	(4.36)
Ionic current density	$i_{\mathrm{elyt}}=-\sigma_{\mathrm{elyt}}^{\mathrm{eff}}\frac{\partial}{\partial y}\phi_{\mathrm{elyt}}=-\sigma_{\mathrm{elyt}}f_{\sigma}\frac{\partial}{\partial y}\phi_{\mathrm{elyt}}$	(4.37)
Electronic current of mixed ionic and electronic conducting electrolyte	$i_{\mathrm{el}}=-i_{\mathrm{elyt}}\frac{\sigma_{\mathrm{elyt}}^{\mathrm{e}}(p_{\mathrm{O_2}}^{\mathrm{ca}},T)}{\sigma_{\mathrm{elyt}}^{\mathrm{i}}(T)}\exp\left(\frac{\eta_{\mathrm{ca}}F}{RT}\right)\cdot\frac{\exp(EF/RT)-1}{1-\exp\left(\left(-i_{\mathrm{elyt}}L_{\mathrm{elyt}}F\right)/\left(RT\sigma_{\mathrm{elyt}}^{\mathrm{i}}\right)\right)}$	(4.38)
Electrolyte electronic conductivity	$\sigma_{\mathrm{elyt}}^{\mathrm{e}}(p_{\mathrm{O_2}}^{\mathrm{cath}},T)=\left(\frac{p_{\mathrm{O_2}}^{\mathrm{cath}}}{p^0}\right)^{-1/4}\cdot\frac{a_0^{\mathrm{elyt}}}{T}\cdot\exp\left(\frac{b_0^{\mathrm{elyt}}}{T}\right)$	(4.39)
Electrolyte ionic conductivity	$\sigma_{\mathrm{elyt}}=\frac{A_\sigma}{T}\cdot\exp\left(-\frac{E_\sigma}{RT}\right)$	(4.40)
Resistance of Pt wire	$R_{\mathrm{a}}=\rho_{\mathrm{con}}\cdot\frac{l_{\mathrm{con}}}{A_{\mathrm{con}}}$	(4.41)
Resistivity of the Pt wire	$\rho_{\mathrm{con}}=\rho_{\mathrm{con}}^0\cdot(1+\alpha_{\mathrm{con}}\cdot(T-T_0))$	(4.42)

4.3 Simulation targets for model validation

To validate the model, simulation targets have to be defined. The simulation targets have to be experimentally available physical data which the model has to predict correctly after an adjustment of model parameters. If the model is able to reproduce the chosen experimental findings it is validated. It may then be assumed that model predictions outside the experimentally covered conditions, are also correct. Experimentally the cell temperature on the cathode surface (T_{cath}) and current-voltage characteristics (IV curves) were recorded for a variety of equivalence ratios ϕ and temperatures (realised by varying the burner-SOFC distances d). These flame conditions are summarised in Tab. 4.2. The key features of the system identified experimentally:

1. *Linearity of the IV curves*: The IV curves for all investigated flame conditions show a characteristic linear shape which deviates from the theoretically expected non-linear current-voltage relation.

2. *OCV*: The OCV is lower than the theoretically predicted values from thermodynamics.

3. P_{max}: The power output of the SOFC is small compared to the fuel available for electrochemical conversion by the SOFC.

4. T_{cath}: Temperatures measured with a surface thermocouple at the cathode side of the fuel cell when it is placed inside the flame exhaust gas are low compared to flame temperatures measured without the SOFC.

As the only input parameters of our simulations are the composition of the fuel depicted by the equivalence ratio ϕ, the inlet velocity of the premixed fuel v_{inlet}, and the distance between burner outlet and anodic surface of the fuel cell d, all of features listed above can be directly predicted by the model described in Sec. 4.2 and are ideal for model validation. Clearly, given the complexity of the system and the level of detail it is modelled at, a large number of parameters enter the simulations (see Tab. 4.3 at the end of the chapter) and not all of them are known exactly. This is either because they cannot be derived by other means than simulation (e.g., the reaction rates of the charge-transfer reactions), or because published data is not exactly applicable to the experimental conditions or the materials used (e.g., the cathodic emissivity or the electronic conductivity of the SDC electrolyte), or simply because they were deemed unimportant (e.g., the length of the contact wire being exposed to the hot flame exhausts). The missing or uncertain parameters have to be adjusted within physically reasonable ranges so the model correctly reproduces the experimental results. The results of the model validation will be discussed in Sec. 4.4.3.

Table 4.2: *Overview over the different flame conditions used in this study. Std. marks the standard condition used for comparison between full model and reduced models.*

No.	ϕ	v_{inlet} [cm/s]	d [cm]	No.	ϕ	v_{inlet} [cm/s]	d [cm]
1	1.1	10	2	7	1.3	10	2
2	1.1	20	2	8	1.3	20	2
3	1.1	30	2	9	1.3	30	2
4	1.2	10	2	10	1.4	10	2
5	1.2	20	2	11	1.4	20	2
6	1.2	30	2	Std.	1.2	10	1

4.4 Results and discussion

In this Section we will first analyse the DFFC system using the model described in Sec. 4.2. This is the most detailed level of modelling presented here and is therefore called the "full model ". Based on the insight gained, two simplified models will be developed in Sec. 4.4.2 which will then be used for validation (Sec. 4.4.3) and optimisation (Sec. 4.4.5).

4.4.1 Results of the full model

Simulations using the full model were carried out for one representative flame condition (Std. in Tab. 4.2). This condition was chosen because in the experiment it yielded a stable flame for all investigated fuels. Simulations were carried out for both, an unpolarised and a polarised cell. Figure 4.3 shows the calculated current-voltage curve and power density (a) and the spatially resolved temperature profile (b) in comparison with the experimental data. The profiles of major gas-phase species (c), selected carbon radicals (e), OH radicals and the radial and axial gas velocities (d) are plotted versus the distance from the cathode surface for an unpolarised SOFC. The boundary conditions for the burner outlet (temperature and axial velocity) are set according to the experimental conditions (water-cooled burner sinter matrix and gas outflow velocity).

Cell at OCV. If no external load is connected to the fuel cell (open circuit or OCV condition) and the system has reached a steady state, a time-independent species and temperature profile will develop in the gas phase between burner and anode surface showing only spatial variations. We observe that the temperature distribution within the fuel cell (Fig. 4.3 b) is almost uniform (simulated difference between anode and cathode surface: 3 K). This results from the high heat conductivity of 5-10 W/mK combined

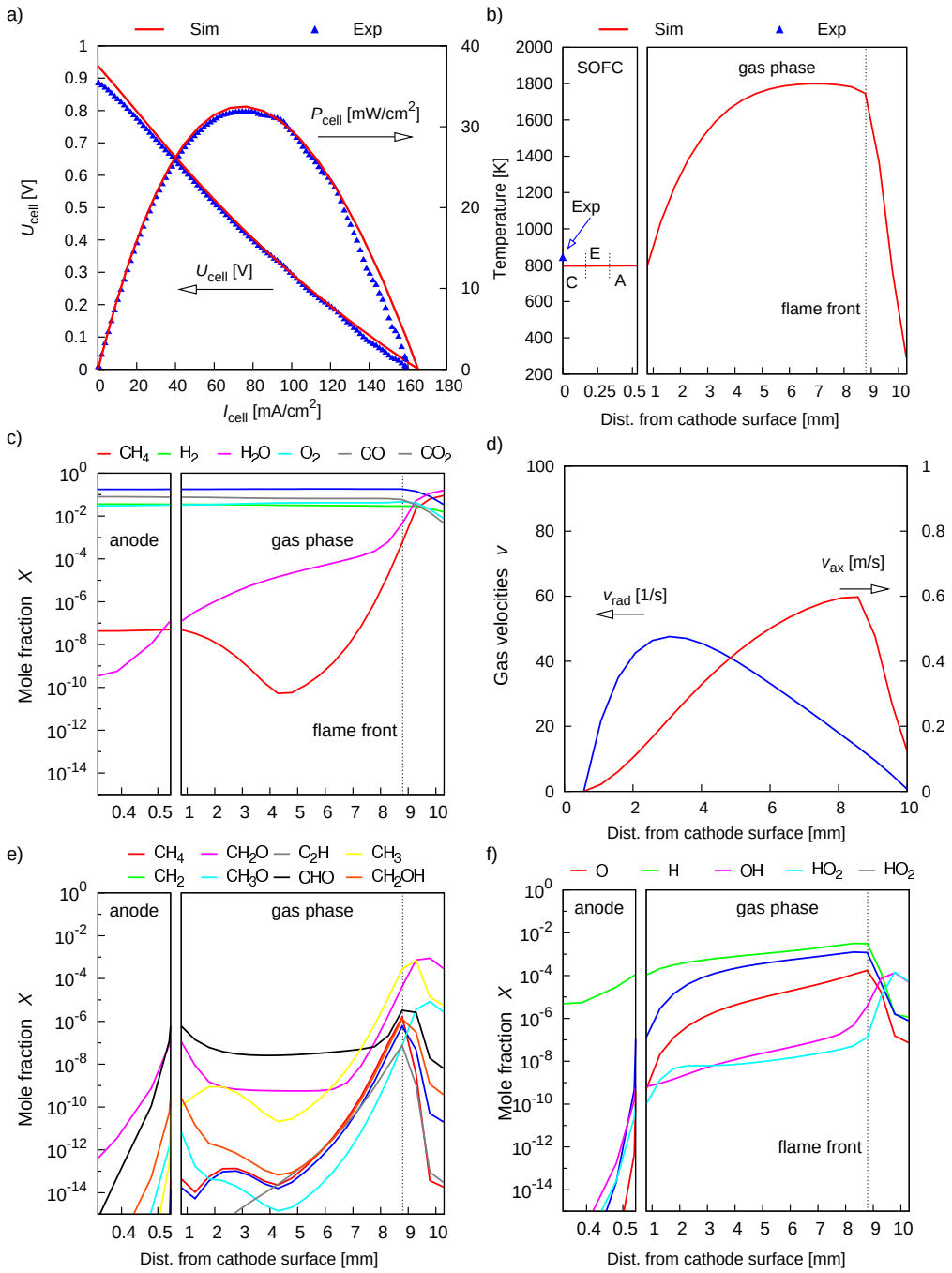

Figure 4.3: *Simulation results of the full model for the DFFC system calculated at standard conditions (Tab. 4.2, Std.) a) IV-curve and power density compared to experimental data. b) Temperature profile in the gas phase and the solid phases of cathode (C), electrolyte (E) and anode (A). c) Major gas-phase species in the porous gas phase of the anode and the free gas phase between burner and anode. d) Radial and axial velocities in the gas phase. e+f) Radical species in porous gas phase of the anode and the free gas phase between burner and anode surface.*

with the the small thickness of the SOFC compared to the gas phase which is several mm thick and has a heat conductivity of around 0.025 W/mK. The DFFC system produces heat via the combustion chemistry. The peak temperature of the flame is about 1900 K which is about 300 K lower compared to an adiabatic flame of the same equivalence ratio. The fuel cell influences the flame thermally as it deposes the system of thermal energy resulting in a lower peak temperature compared to adiabatic flame conditions. Heat is lost via three mechanisms: (1) Heat conduction and convection away from the cathode surface; (2) heat conduction from the gas phase to the cooled burner matrix; (3) radiation from both SOFC surfaces. Thus, the SOFC and the flame are thermally strongly coupled. The species profiles in the gas phase (Fig. 4.3 c,e,f) are highly nonlinear, resulting from the coupled transport, reaction kinetics, and thermodynamical properties. For example, when going from the burner outlet towards the SOFC, the methane mole fraction strongly decreases to 10^{-10} as it is consumed through gas-phase flame chemistry. As the gas mixture rapidly cools down on its way towards the anode, further reactions establish a value around 10^{-5} which is close to the equilibrium concentration. Other main species (H_2O, H_2, CO, CO_2) show only little variation once behind the flame front. The radical species peak at the flame front, which is typical for flames and then follow their respective kinetic and thermodynamic properties when the gas cools down. The flame, judged by the concentration profiles of oxygen and methane, extends roughly about 1 cm from the burner outlet in the direction of the fuel cell which is in good agreement with free flames [54]. The concentration of the radical species strongly decreases inside the porous structure of the anode as they undergo heterogeneous reactions with the catalytically active anode surface forming stable gas-phase species.

Cell under load. When current is drawn from the cell, oxygen from the cathode is transported through the electrolyte and used to oxidise the fuel on the anode side. In principle any species at the anode side that can be oxidised may serve as a fuel. To determine the main electrochemically active species of the DFFC system, calculations of the SOFC under electrical load (150 mA) are compared to OCV conditions. The value of 150 mA was chosen because it is the maximum current which could be drawn from the cell experimentally at the standard conditions and hence the effect on surface coverage and gas-phase concentration will be strongest. Figure 4.4 shows the concentration profiles of the gas-phase species inside the porous anode and in the gas volume between the anode and the burner outlet for selected species at OCV (0 mA) and at 150 mA electrical load. Methane and oxygen (Figure 4.4 a) rapidly decrease from the their inlet concentrations at $\phi = 1.2$ close to the burner outlet. As they are consumed by the flame, radical species are produced (OH, H, CH). Polarisation shows hardly any effect on the concentration of any of the species (note the logarithmic scale). All flame radicals have an overall low concentration inside the porous anode. In Fig. 4.4 b) the electrochemically

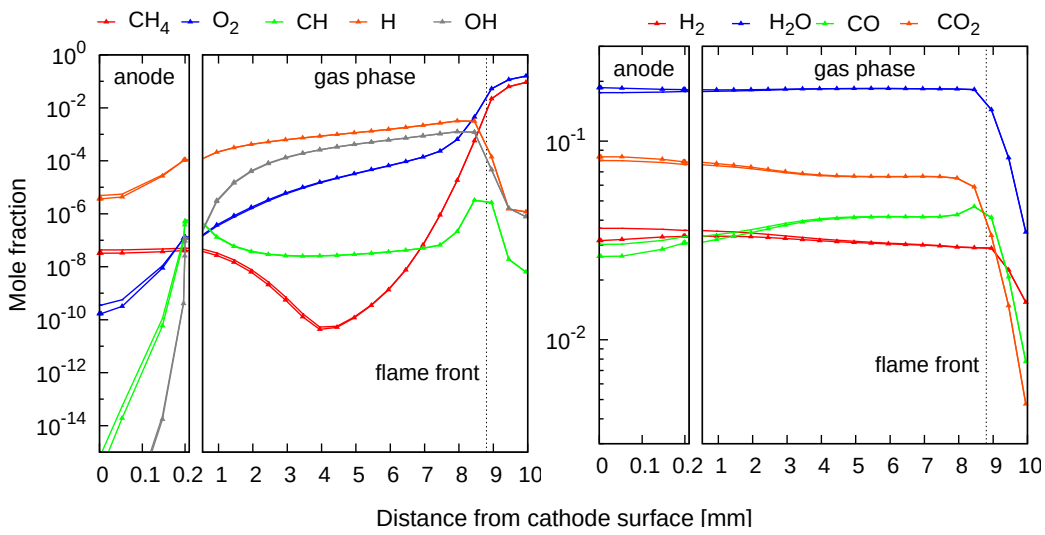

Figure 4.4: *Comparison of concentration profiles of selected gas-phase species in the porous anode and the gas phase calculated for OCV (solid lines) and for 150 mA electrical load (lines with symbols). The profiles are given in two plots for visibility.*

active species are plotted. Hydrogen and CO show lower concentrations when the cell is polarised than for OCV. This is caused by their electrochemical conversion into water and CO_2. The lowest concentration of the fuel species CO and H_2 can be found close to the electrolyte, steadily increasing in the direction of the anode/gas interface. The concentrations of all species under polarisation converge against their respective values at OCV when approaching the flame front. From this it becomes obvious that the fuel cell cannot even come close to consume the amount of fuel supplied by the flame, and most of the fuel leaves the system unused. Another consequence of this observation is that the products of the electrochemical conversion taking place inside the SOFC do not influence the process; the combustion flame and the SOFC are chemically decoupled.

In Fig. 4.5 the surface coverages of the electrochemically active species are plotted versus the distance from the dense electrolyte. The surface coverages show the same trend as the gas concentrations; when current is drawn from the cell the coverage of CO and H decreases whereas the coverages of CO_2 and water increase over the whole length of the porous anode. All species show the highest change of coverage close to the dense electrolyte and converge to their coverages at OCV when getting closer to the anode/gas interface. This indicates that the electrochemical reactions are confined in a thin layer close to the dense electrolyte. The difference between coverages at OCV and under polarisation in absolute values are small as ad- and desorption reactions are fast compared to the electrochemical conversion. Both fuel species, CO and H, undergo electrochemical reactions close to the dense electrolyte where oxygen is supplied by the electrolyte. The coverage of CO_2 is highest at the

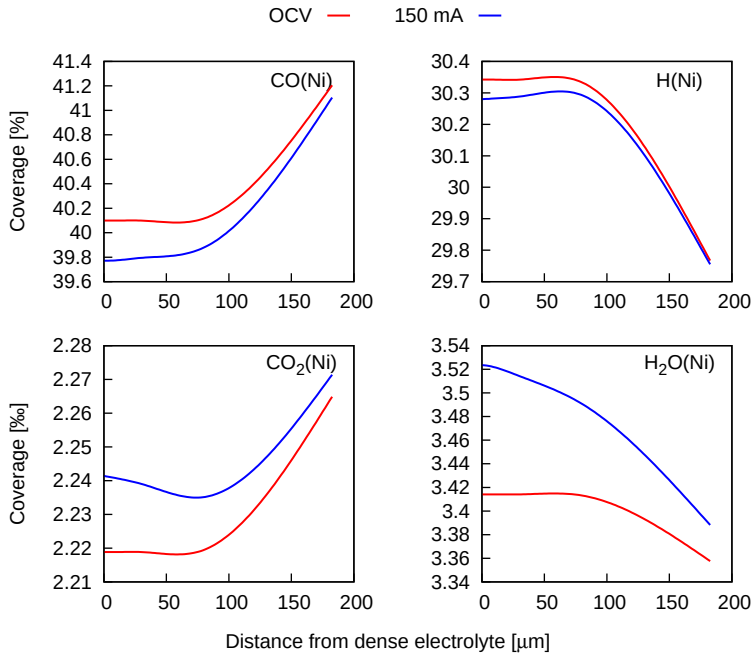

Figure 4.5: *Coverages of nickel surface in the porous anode for OCV condition and at 150 mA electrical load.*

electrode/gas interface. This may be due to the higher CO_2 concentration in the gas phase which causes a higher surface coverage, but as well by CO_2 formation by surface-bound CO and oxygen adsorbing from the gas phase.

4.4.2 Model reduction

The full model used in the previous Section is detailed but computationally costly and therefore is not suitable for parameter studies or optimisation. As the performance of a SOFC is determined by the spatial distribution of species and temperature throughout the system, we set up two reduced models: One to simulate the IV characteristics (IV model) and a second to describe the heat management throughout the cell (thermal model).

IV model. The simulation of the flame is by far the most time-consuming aspect of the model, so the first question has to be to which detail the gas-phase chemistry has to be accounted for. As discussed in Section 4.4.1, the flame and the SOFC are chemically decoupled. Neither the flame is influenced by the products of the fuel cell nor does the gas-phase composition close to the SOFC change significantly if current is drawn. For the IV calculations we will exploit this and assume a constant composition of the gas atmosphere just above the SOFC anode. To account for the different burner operating conditions and the accordingly different gas compositions, the concentration

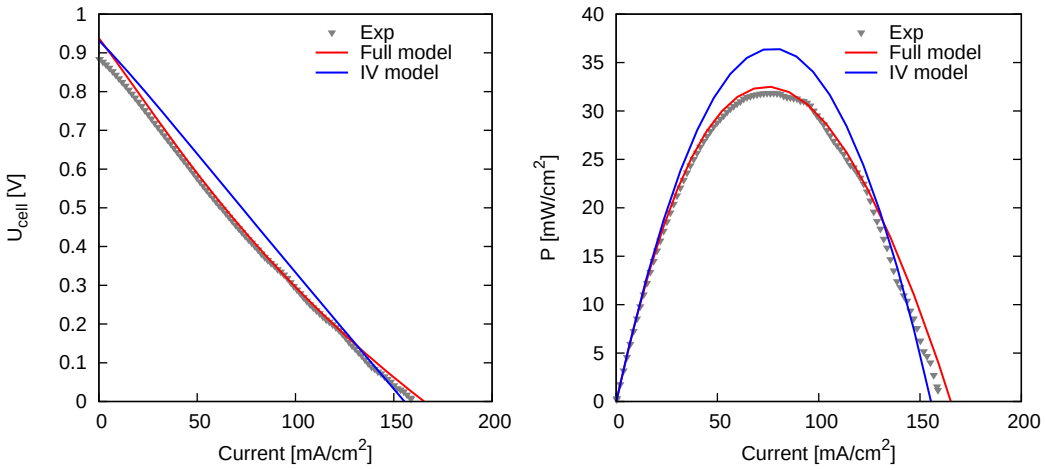

Figure 4.6: *Comparison of calculated (IV model and full model) and measured current-voltage and current-power relations. Left: Current-voltage relation (IV-curve). Right: current-power relation.*

of gas-phase species is set to the respective values calculated using the full model. In the gas phase of the flame species up to C_3H_7 are present. The calculated abundance of the higher hydrocarbons in the vicinity of the SOFC anode is far below ppm and may safely be neglected. The simulations using the full model predict a temperature variation of only 3 K between the flame-facing anodic side of the SOFC the cathode surface which is in contact with ambient air. Compared to the temperature gradient of roughly 1000 K between burner and anode surface the temperature gradient inside the fuel cell is negligible. Consequently the temperature is set fix to the experimentally determined value of the cathode surface. Throughout the cell isothermal conditions are assumed and heat production within the SOFC is not accounted for. To compare the predictions of the full model with the reduced IV model the current-voltage curves and the power density versus the electrical current are shown together with the experimental results in Fig. 4.6 for standard conditions (Tab. 4.2). The OCV and maximum power density of the two models agree within less then 10% which is an excellent agreement given the strong simplifications made. The linearity of the IV curve and its slope, the other key features of the DFFC system, are almost identical as well. As the main features are mapped correctly by the simplified approach, the IV model will be used in the following for model validation and parameter studies. The calculation of an IV curve with 100 equidistant points between open circuit and maximum current takes roughly 6 hours using the full model. This could be reduced to about 10 minutes when calculations are performed with the IV model.

Thermal model. It became evident from the experiments that the system's performance was tightly coupled to the cell temperature. Generally, to set

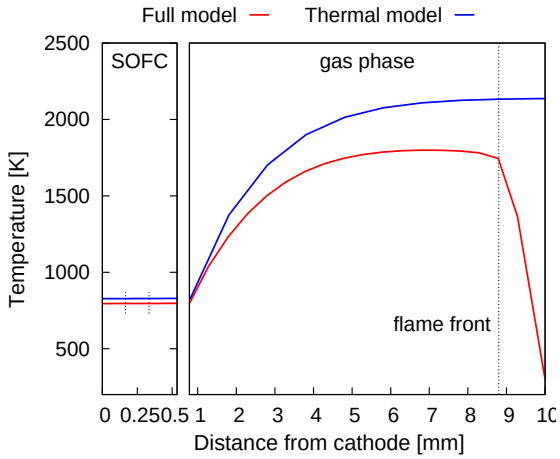

Figure 4.7: *Comparison of simulated temperature distributions throughout the system. Calculations performed with the full model and the reduced thermal model at the standard condition.*

up a simplified model for simulation of the temperature distribution throughout the system, the same considerations as for the IV model can be applied, namely the reduction of the complexity induced by the combustion process. The flame supplies heat to the system and converts the methane-air mixture into the flame exhaust gas containing partially oxidised species serving as the fuel for the SOFC. For the thermal model only the peak temperature, the velocity as well as the heat and mass transport properties of the gas phase and the fuel cell are of importance. Analysing the temperature profile in Fig. 4.3 b) shows that the temperature peaks close to the flame front and decreases rapidly as the system is deprived of thermal energy by the fuel cell. As the flame front is very close to the burner outlet, instead of simulating the combustion process itself, we can assume boundary conditions at the burner outlet similar to conditions just behind the flame front. For the temperature, the gas velocity and the species concentrations we use the respective values for an adiabatic flame of the same equivalence ratio. The gas phase between the burner and the anode surface is treated non-reactive. For the fuel cell, only diffusive heat transport in the direction perpendicular to the surface as well as heat production/consumption by the heterogeneous chemistry inside the porous anode are taken into account. Figure 4.7 shows the two temperature distributions calculated by the full model and the thermal model. The initial temperature of the thermal model at the burner outlet is equal to the adiabatic flame temperature and therefore about 1800 K higher than the temperature from the full model where the boundary condition of the cooled burner matrix fixes the temperature to 293 K. The peak temperature of the is about 200 K lower than the peak temperature (inlet temperature) of the thermal model. This agrees to theoretical considerations: the adiabatic flame temperature is the highest temperature the flame is capable of for the respective flame condition and the fuel cell partly deprives the system of its thermal

energy as it is placed into the exhaust gas thus lowering the peak temperature. For the thermal model the adiabatic temperature is set as a boundary condition to the problem so the fuel cell has no influence on it. The temperature calculated using the thermal model decreases in the same manner as for the full model resulting in an anodic surface temperature within 5% of the values derived from the full model. The temperature difference $\Delta T = T_{\mathrm{an}} - T_{\mathrm{cath}}$ between anode and cathode are almost identical (difference smaller than 1%). The two important features, anode surface temperature and temperature difference ΔT thus are reproduced well by the simplified thermal model so it will be used for model validation in the remainder of this Section.

4.4.3 Model validation

The SOFC used in the direct flame setup of the system was experimentally characterised by current-voltage dependencies giving access to the open circuit voltage (OCV) and the maximum power output (P_{max}) of the cell. The parameters as well as the temperature on the cathode side of the SOFC were measured for a variety of fuel-air ratios ϕ and gas inlet velocities v_{inlet} (see Tab. 4.2).

IV model. Figure 4.8 shows how the predictions of the IV model compare to the measured current-voltage dependencies. Each graph in the figure shows the experimental data (black symbols) and the simulation (green) for one flame condition. The Figure shows that for all flame conditions simulation and experiment show a nearly linear relation between current and cell voltage. This indicates that the system is, even at high currents, not limited by transport processes. The model predictions show a good agreement with the experiment except for three flame conditions ($\phi = 1.1$, $v_{\mathrm{inlet}} = 0.1\,\mathrm{m/s}$; $\phi = 1.1$, $v_{\mathrm{inlet}} = 0.2\,\mathrm{m/s}$ and $\phi = 1.2$, $v_{\mathrm{inlet}} = 0.1\,\mathrm{m/s}$). To allow for a better comparison of the target variables, the maximum power output P_{max} and the OCV versus the flame conditions are shown in Fig. 4.9. Both, the predicted and experimentally measured OCV decrease for constant equivalence ratio with increasing fuel inlet velocities. An increasing inlet velocity corresponds to an increasing SOFC temperature and thus, a better electronic conductivity of the electrolyte. This increases the short-circuiting of the fuel cell by the electronic current through the electrolyte resulting in a lower OCV. Generally the OCV is over predicted. This is not a problem of the reduced IV model as the full model shows this behaviour as well (Fig. 4.6). Two reasons for this systematic over prediction are possible. Firstly, in the experimental setup the flame exhaust may alter the cathodic gas composition as it flows around the sample holder. This would result in lower OCV due to a lower concentration of oxygen. Calculations assuming an oxygen concentration of about 1% instead of 21% resulted in a correct prediction of the OCV. However it is deemed unlikely that the exhaust would alter the cathode gas composition to such an extent without a flame developing on

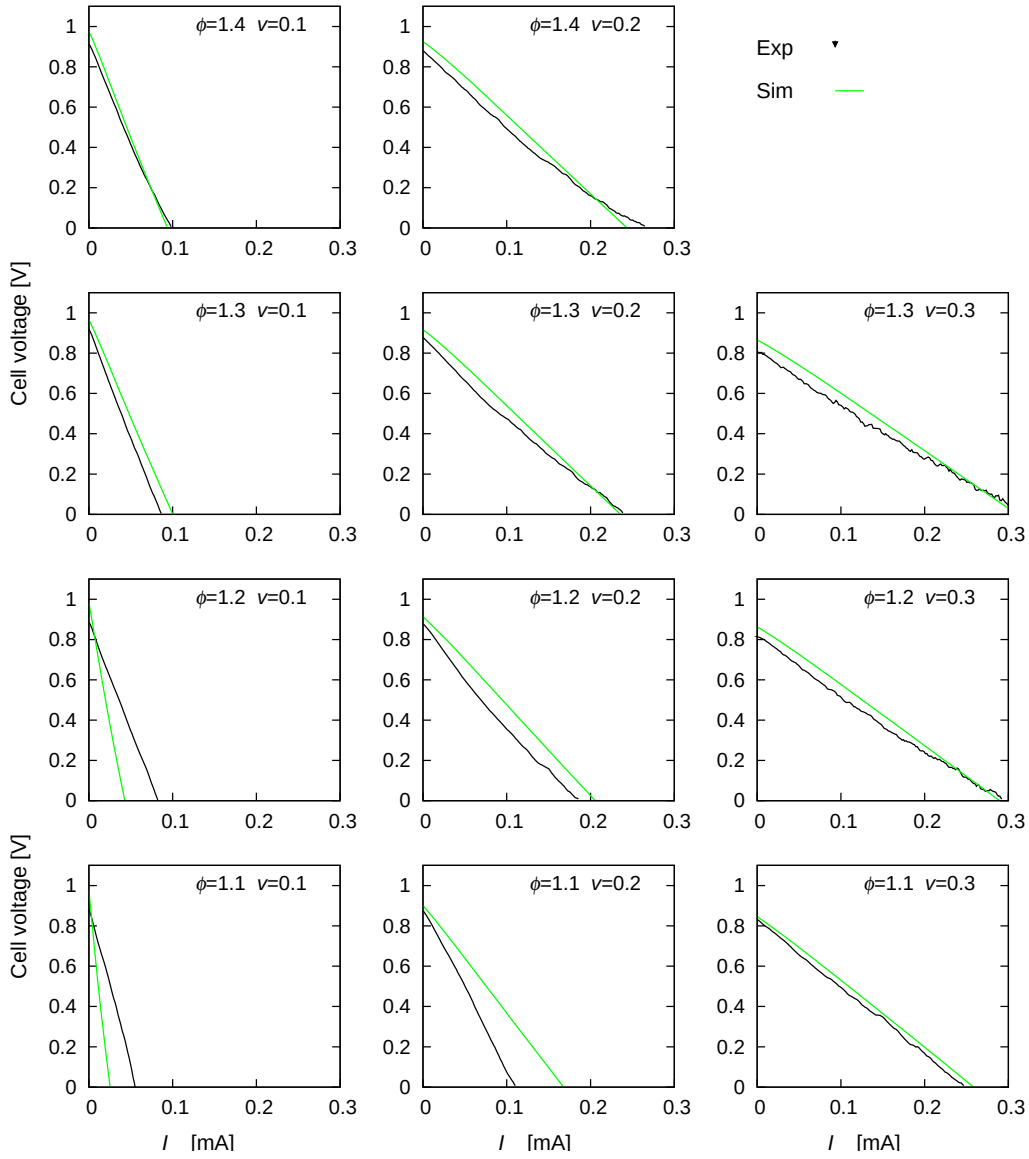

Figure 4.8: *Comparison of simulated and experimental current-voltage curves for all investigated flame conditions (see Tab. 4.2).*

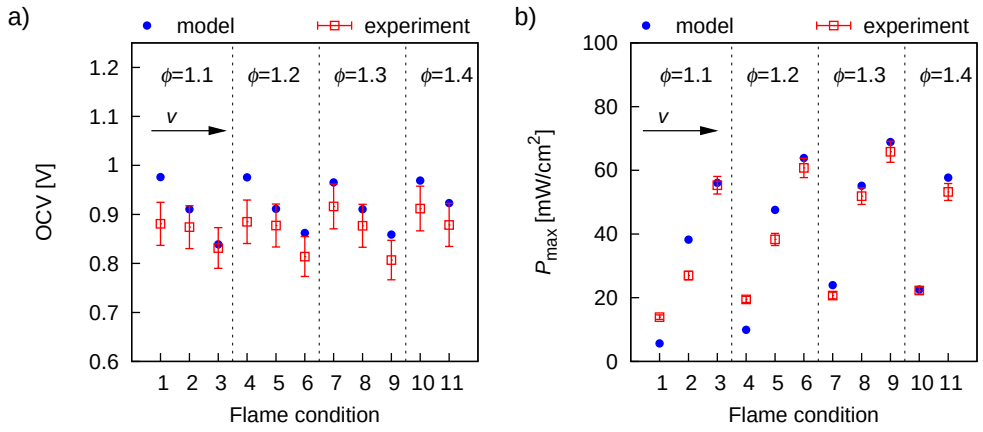

Figure 4.9: *Validation of the IV model against the experimental target parameters OCV and maximum power density $P_{\max}$ (no flame, isothermal cell). The flame condition are specified in Tab. 4.2*

the cathode side. Secondly, the electrolyte layer may not be completely gas-tight allowing the cross-over of fuel and oxidiser thereby lowering the OCV. Especially after several thermo cycles during start-up and shut-down micro-cracks might be introduced in the electrolyte by thermal stress. Thirdly, the electronic conductivity of the electrolyte could be estimated too low. The coefficients for the calculation of the electronic conductivity depend on the composition of the SDC. Literature data had to be extrapolated to the exact material composition used in the experiments. In the experiments the OCV seems to convergence against a certain limit at lower inlet velocities at equivalence ratios of 1.1 and 1.2 whereas for higher ϕ is the OCV decreases linearly with increasing inlet velocity (Fig. 4.9 a). The simulations do not show such an additional dependence of the OCV on the equivalence ratio but an always linear trend for the OCV inverse proportional to the inlet velocity and the temperature. Experiment and simulation agree in showing a constant OCV for constant inlet velocities under a variation of equivalence ratio. With respect to the maximum power output shown in Fig. 4.9 b) the model predictions and experimental data are in good agreement. Both show an increase of system performance with increasing velocity and, for constant velocities, with increasing equivalence ratio. Generally an increase in inflow velocity of the premixed fuel results in an increase of the temperature of the SOFC. As most processes inside the SOFC like electrochemical reactions and ionic resistivity are thermally activated, a performance increase with increasing temperature is expected. Figure 4.8 shows that the flame conditions 1,2,4 and 5 have the worst agreement with the experiment. Looking at the trends in Fig. 4.9, the flame conditions do not differ systematically so consequently no conclusion with respect to the origin of the mismatch could be drawn.

Thermal model. In Fig. 4.10 measured data from the surface thermocouple are compared to the predicted cathode temperatures for all investigated

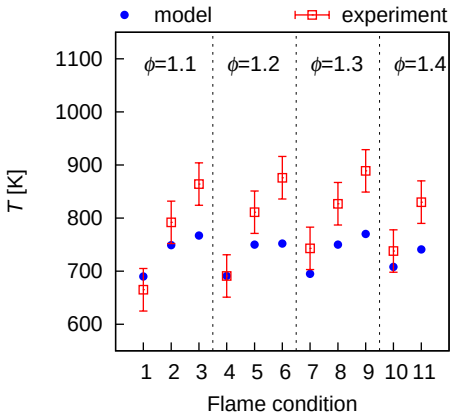

Figure 4.10: *Validation of thermal model by comparing the calculated cell temperature at the cathode side with thermocouple measurements on the cathode surface. The flame condition are specified in Tab. 4.2.*

flame conditions. The experimental data show a clear trend: The temperature on the cathode surface increases strongly with increasing inlet velocity and slightly with increasing equivalence ratio. The increasing temperature with increasing equivalence ration is not observed in freely burning flames investigated with the same experimental setup and is contradictory to combustion theory where temperatures decrease the more the equivalence ratio differs from unity [54]. In the simulation this is inherently reproduced as the adiabatic flame temperature which is used as boundary condition for the inlet directly follows from combustion theory. The simulation predicts a saturation-like behaviour of the temperature with increasing inflow velocity whereas the experimental data show a steady increase. The predictions of the reduced model are self-consistent: High inlet velocities lead to a high thermal dissipation of the system by the fuel cell as the regions of high temperature move closer to the fuel cell. Although some qualitative trends are predicted correctly by the reduced model, a correct description of the thermal management of the system must be based on the simulation of the combustion process coupled to the fuel cell. This underlines the close thermal coupling of SOFC and the flame.

To validate the predicted system performance with respect to temperature, calculations using the IV model were performed for temperatures ranging from 500 K to 1500 K and are compared to experimental data. With a flat flame-burner no temperatures higher than roughly 1000 K could be achieved, so in order to have experimental reference data we additionally used data from experiments with a porous burner which allows for temperatures up to 1400 K. The experiments with the porous burner where performed by in the course of the cooperation with Shinko Electric Industies Co. Ltd. [129]. The resulting peak power and the predicted OCV for the different temperatures are shown in Fig. 4.11 together with the theoretical value $\mathrm{OCV}_{\mathrm{Nernst}}$ calculated from the Nernst equation under the assumption of a thermally equilibrated

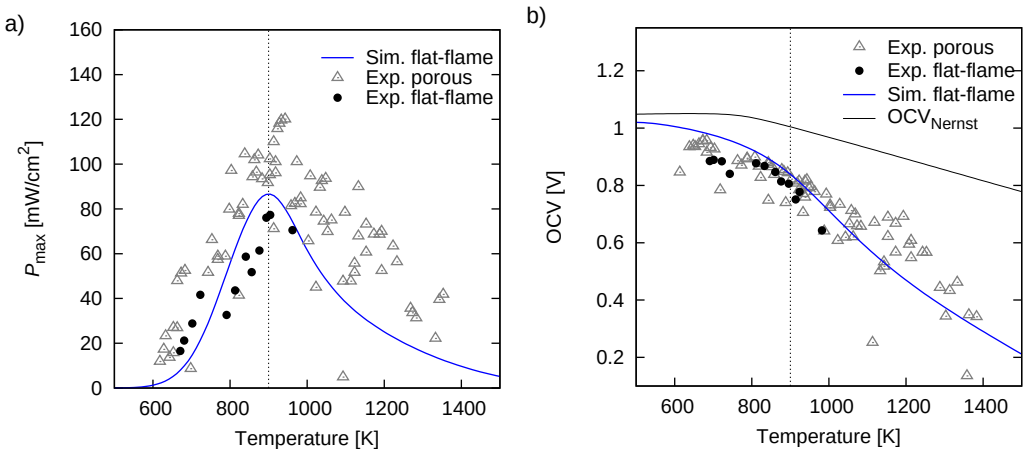

Figure 4.11: *Open circuit voltage (OCV) and peak power $P_{\max}$ versus cell temperature. Simulations performed for standard conditions using the IV model. The vertical lines denote the temperature of maximum peak power. Experimental data from porous burner were performed with different cells and are added to show the trends for higher temperatures.*

gas phase. The figure shows that theoretical, simulated and experimentally measured values for OCV all decrease with temperature. The Nernst voltage is the upper boundary and the experimental values as well as the simulated OCVs show a stronger temperature dependence as theoretically predicted. This is due to the fact that in the DFFC system the electrolyte is electronically conducing whereas for the theoretical calculations a completely gas-tight and perfectly insulating electrolyte is assumed. The higher the temperature the stronger the influence of the electronic conductivity become as it is thermally activated. Consequently, the model-predicted OCV converges against the Nernst voltage for lower temperatures. The power density (Fig. 4.11 b) has a pronounced maximum between 900 K for the flat-flame burner and 940 K for the porous burner which corresponds well with the model predictions. The optimal working temperature T_{peak} for the system is derived by our simulations is 900 K where a power output of around 80 mW at 0.45 V can be expected.

4.4.4 Analysis of loss processes

The performance of a fuel cell is governed by the underlying elementary physico-chemical processes (i.e. mass and charge transport or the kinetics of the electrochemical reactions). The experiments show a maximum in system performance for temperatures 900 K and 940 K. Consequently, at this temperature the power loss of the whole system is minimal. The modelling approach used in this theses allows to determine the contributions of each individual processes to the overall performance loss and can therefore give directions for system optimisation. Figure 4.12 shows the absolute and rel-

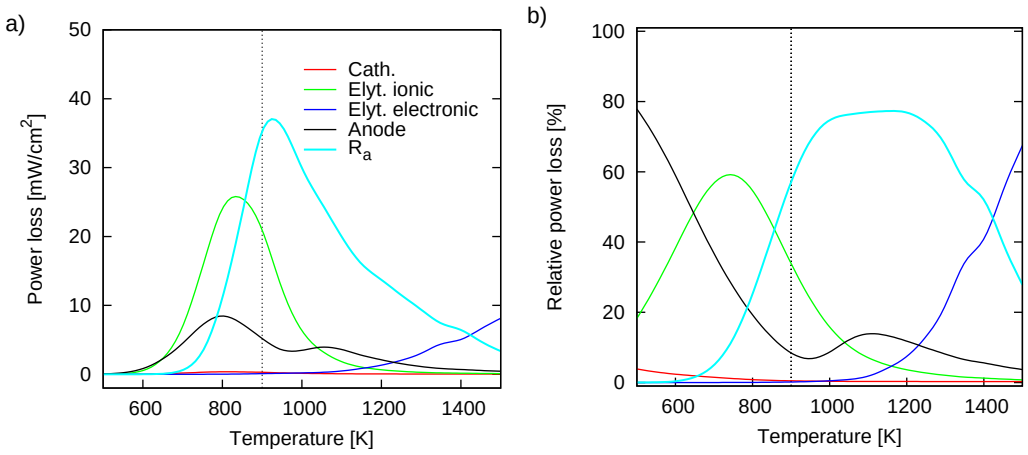

Figure 4.12: *Calculated power losses of individual parts of the fuel cell versus the operating temperature. Simulations performed with the IV model for standard conditions. The vertical line denotes the temperature of maximum peak power (see Fig. 4.11).*

ative power losses versus the cell temperature. Four main contributions can be identified:

- The largest contribution results from the connection wires (R_a). In the experiments these were two thin platinum wires attached to the current collector embedded into the electrodes. The platinum wire has a temperature-dependent resistivity described by Eq. 4.42. The losses of the wires follow Ohm's law so they are proportional to the cell voltage. At high temperatures, the power loss due to the contact wires is approximately equal to the total peak power of the system. This clearly is a design error.

- The second largest part, amounting to one third of the power output from the system, is due to ohmic losses in the dense electrolyte. As current is drawn from the cell oxygen ions have to move from the cathode through the lattice structure of the dense electrolyte. The transport is hindered by the finite mobility of the oxygen ions inside the lattice structure. This usually is termed ionic resistivity of the electrolyte. The movement of the ions is a thermally activated process so the ionic resistivity decreases with increasing temperature according to Eq. 4.40. The ionic conductivity is a material specific parameter. Changing the electrolyte material is one way to improve the system performance, another is decreasing its thickness. The thinner the dense electrolyte layer, the lower the power loss resulting from the ionic conductivity (Eq. 4.37) – a good starting point for optimisation.

- The polarisation losses of the anode represent the third largest part and reduces the power of the system by about 10%. Possible causes are

transport limitations in the porous anode or simply a slow electrochemical reaction. The shape of the IV curves in Fig. 4.8 is approximately linear in the cell voltage, a first indication that no transport limitations are expected. Transport becomes more important the further fuel or reaction products have to be transported and the higher the current density of the cell becomes. Thus, even when for the current system transport is not limiting it may well become important if other components of the system are improved.

- Losses due to the electronic conductivity of the electrolyte play only a minor role. The electrolyte material used (samarium-doped ceria) is a mixed conducting electrolyte. This causes, in addition to the losses resulting from the transport of oxygen ions, a power loss by "short-circuiting" the anode and the cathode via the electrolyte. Consequently the electronic conductivity reduces the OCV and the cell voltage in general. The electronic conductivity is again a material property. It is temperature dependent as described by Eq. 4.39. More importantly, the overall electronic current depends strongly on the cell polarisation (Eq. 4.38): It decreases with increasing polarisation. Although it has a strong impact on the OCV, the influence on the actual operating point is therefore rather small. By extending the electrochemically active region, electrodes with mixed conducting electrolyte phases perform better than purely ionically conducting ones. To reduce the negative effect on the cell voltage either a pure ionic conducting material is used for the dense electrolyte or an additional functional layer is applied between the dense electrolyte and the porous electrode. With respect to the small impact on the system the electronic conductivity will not be subject to optimisation.

Beside the guidelines for system optimisation the analysis shows, that the losses resulting from the connecting wires together with losses due to the ionic resistance strongly dominate the performance of the DFFC system for temperatures between 700 K and 1200 K. As both are proportional to the cell voltage this predominance it the main reason for the "ohmic" behaviour of the current-voltage curves. The relative losses (Fig. 4.12 b) show that short-circuiting of the fuel cell via the electronic current of the electrolyte becomes relevant only at high temperatures. It does not significantly influence the system performance in the temperature range of the experiments.

4.4.5 Model-based optimisation

The DFFC system is intended to produce electrical energy, so in this Section we will try to improve the system with respect to maximum power output. Usually the application a fuel cell is designed for will impose certain constraints on the system such as minimal required voltage or a maximum

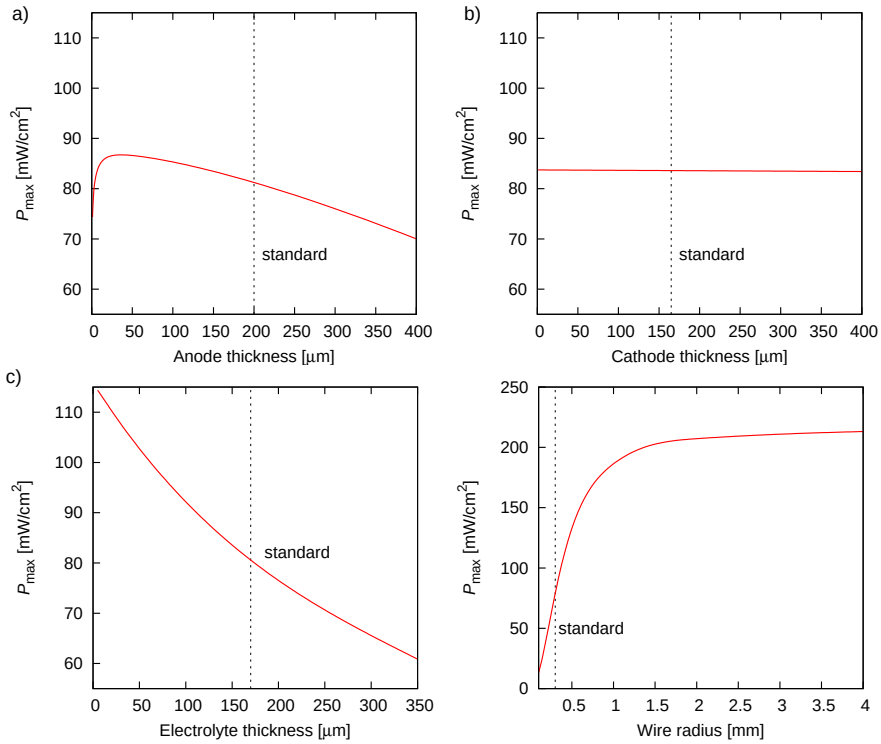

Figure 4.13: *Maximum power density of the system predicted by the IV model versus the different thickness of anode (a), cathode (b), electrolyte layer (c) and radius of the connecting wires. The vertical lines indicate the SOFC parameters used in the experimental characterisation.*

temperature. As we do not have any specific application in mind, we simply optimise the cell for maximum power output at $T = T_{\text{peak}}$. Optimisation must be seen within the context of the production process which usually means that existing processes should be altered as little as possible. Variation of layer thickness is a design parameter which matches this criterium, even more as thinner layers will be more cost effective. Figure 4.13 shows the maximum power versus the thickness of the anode, cathode and electrolyte layers. Figure 4.13 a) shows that the anode layer has an optimal thickness of around 20 microns. Reducing the anode thickness first results in an increase of power density as the ohmic losses decrease and the layer is still thick enough to fully support the electrochemical conversion. Further reducing the layer thickness is at the expense of system performance as the electrochemically active region cannot convert as much fuel anymore. The thickness of the cathode has almost no influence on the systems performance. This corresponds to the the conclusions drawn in the previous section, where the cathodic contribution to the power loss of the system were insignificant. Although this leaves no room for performance improvement, it may well be valuable information. Thin anode and electrolyte layers will need a support to ensure mechanical stability. As a thicker cathode layer up to 1 mm has no negative effect on the performance, the cathode may be used as a support layer. The influence of

the electrolyte layer thickness shown in Fig. 4.13 c) shows no maximum, consequently thinner electrolyte layers always reduced the losses. This of course is true only if the layer will still be gas-tight which sets a limit to the reduction of the layer thickness. The radius of the connecting wires (Fig. 4.13 d) should be as big as possible a doubling of the wire radius results in four times larger peak power density as it enters the resistivity quadratically (Eq. 4.41). With increasing thickness of the wires other loss processes become more and more dominant so a further increase of the radius has no positive effects on the power output. There are a number of system parameters which could be used to improve performance. Additional calculation which are not shown here for the sake of brevity were performed for the cathodic emissivity of the SOFC (this increases the SOFC temperature) as well as for the porosity of the anode layer. Neither of these parameters resulted in a noteworthy change of performance.

4.5 Conclusions

In this chapter a computational model was described allowing for the simulation and optimisation of a direct flame fuel cell system. First a very detailed full model was set up. The detailed model comprises of an elementary kinetic description of a premixed methane-air flame, a stagnation-point flow description of the coupled heat and mass transport within the gas phase, an elementary kinetic description of the electrochemistry of the SOFC anode, a global description of the SOFC cathode as well as diffusive heat, mass and charge transport throughout the whole SOFC. The full model allowed to identify H_2 and CO as fuel species and gave indications were model simplifications where appropriate. Two simplified models were designed: The IV model for performance studies and the thermal model for studies on the thermal management. As the predictions of the reduced models were in excellent agreement with the results of the detailed model, the reduced models were exclusively used for model validation and system optimisation. The validation of the IV model with the experimentally determined values for OCV, $P_{\max}$ and their respective dependence on temperature and flame condition showed that all key features of the system were predicted very well. The validation of the thermal model revealed an oversimplification; reliable studies on the thermal management of the system require the inclusion of the combustion process. Using the IV model, studies on the temperature dependence of system performance resulted in the determination of an optimum working temperature of the system. The quantification of the individual contributions of the different loss processes and their associated constituents of the SOFC allowed for the determination of an optimal anode thickness and the identification of the cathode as possible support layer. It was shown that the connecting wires dominate the system performance. For the design of the system an electrolyte layer as thin as possible and a better wiring of the SOFC during

characterisation where shown to be of great importance for further studies. If the experimental setup is improved power densities of about 200 $^{mW}/_{cm^2}$ can be expected. Although not detected for the studied cell design, higher power densities may introduce transport limitations or increase the importance of the cathode and fuel utilisation. Given the simplicity of the system and a potential power density of 200 $^{mW}/_{cm^2}$ if wiring and electrolyte thickness are optimised, further studies seem appropriate.

Tabulated model parameters

Table 4.3: *Summarised model parameters. a) Values fitted to experimental data provided by Shinko Electric Industies Co. Ltd. b) Parameter was adjusted by fitting to experimental data of Kronemayer et al. [125]. c) Estimated from REM pictures provided by Shinko Electric Industies Co. Ltd. d) Estimated. e) Estimated from percolation theory [29]. f) Material data sheet from manufacturer. g) From the experimental setup.*

Parameter	Value	Unit	Ref.
Porous gas-phase transport			
d_{an}	175	μm	c)
ϵ^{an}	37%	-	c),e)
τ^{an}	3.5	-	d)
d_{cath}	250	μm	c)
ϵ^{cath}	0.3	-	c)
τ^{cath}	4	-	d)
Electric parameters			
A_{cell}	1.3	cm^2	g)
a_0^{elyt}	$7.3 \cdot 10^{11}$	$\frac{K}{(\Omega \cdot m \cdot Pa^{1/4})}$	[15]
b_0^{elyt}	$2.7 \cdot 10^{-4}$	K	[15]
E_σ	77.2	kJ	[29]
A_σ	$5.2 \cdot 10^7$	$^1/_K$	[29]
d_{elyt}	170	μm	c)
l_{con}	0.6	cm	g)
A_{con}	0.28	mm^2	f)
α_{con}	$3.8 \cdot 10^{-3}$	$^1/_K$	f)
ρ_{con}^0	110	$\frac{(\Omega \cdot mm^2)}{m}$	f)

Parameter	Value	Unit	Ref.
Electrochemistry			
β	0.5	-	[34]
E_{cath}^{act}	88.6	$\frac{kJ}{mol}$	[34]
i_{ca}^*	$5.9 \cdot 10^{17}$	$\frac{A}{m^3}$	[34]
$p(O_2)$	21.3	kPa	g)
$l_{TPB}^{V,an}$	$1 \cdot 10^{12}$	$^m/_{m^3}$	e)
k_{H1}^0	135	$\frac{mol}{s}$	b)
E_{H1}^{act}	185	$\frac{kJ}{mol}$	b)
E_{el}^{act}	200	$\frac{kJ}{mol}$	[35]
$p_{cath}^{O_2}$	$4.9 \cdot 10^8$	atm	[35]
Heat management			
L_{char}	0.012	m	g)
Nu	1	-	[130]
λ_q^{air}	0.058	$^W/_{(mK)}$	[130]
λ_q^{elyt}	5	$^W/_{(mK)}$	c)
λ_q^{an}	8	$^W/_{(mK)}$	c)
λ_q^{cat}	10	$^W/_{(mK)}$	c)
ϵ_q^{ca}	0.75	-	[131]
ϵ_q^{an}	0.75	-	[131]

Chapter 5

Summary

In this thesis a model for the prediction of fuel cell performance on the cell level was developed. The model is able to quantitatively predict macroscopic current-voltage characteristics of SOFCs based solely on fundamental physicochemical processes. The model was used in a fundamental study of elementary charge-transfer processes on model electrodes as well as for system optimisation of a full SOFC coupled to a flame.

Modelling framework. In the modelling approach, chemical reactions are resolved into elementary steps and reaction kinetics are based on transition state theory. The detailed reaction kinetics applied for the gas phase and the surfaces of electrolyte and electrode resolve the tight coupling of the functional constituents of an SOFC. The generation of electrical current is based on the kinetic description of elementary charge-transfer reactions occurring at the interfaces of electrode and electrolyte. Transport phenomena occurring over length scales ranging from micrometer to centimeter are described by fundamental conservation principles of mass, charge and energy. The formulation of the model based on fundamental processes allows to apply the model to a wide range of experimental setups, cell designs and operating conditions. In this thesis the model was was applied to elementary kinetic studies and system optimisation.

Ni/YSZ model anodes. In Ch. 3 a detailed investigation of elementary charge-transfer kinetics and related transport processes was performed. Model predictions from a variety of different charge-transfer mechanisms proposed in literature were compared to experimental data from a Ni/YSZ model-anode setup. It could be shown that the most probable charge-transfer reaction is based on the transport of hydrogen from the electrode to the electrolyte. For the first time a full kinetic description of the interface processes was performed without a priori assuming a rate-limiting process. The results showed that indeed, the charge-transfer reaction is one of the rate limiting

process, putting the widely-spread assumption on a firm base. However, the results showed that, in contrast to a broad consensus, surface transport and the kinetics of heterogeneous surface chemistry do influence the polarisation behaviour of SOFCs. In fact, the simulations predict a limiting current under cathodic polarisation meaning that surface diffusion and heterogeneous kinetics on the electrolyte may even dominate the behaviour under certain conditions.

Direct flame fuel cell. Using the elementary kinetic charge-transfer step identified in the studies on model anodes, a system study of a full SOFC coupled to a flame was performed in Ch. 4. The system was first analysed using a detailed model accounting for full thermal and chemical coupling of a rich methane/air flame to a mixed-conductor based SOFC. The results identified H_2 and CO as electrochemically active species and showed tight thermal coupling, but an only weak chemical coupling of flame and fuel cell. Two reduced models were set up and successfully validated against a wide range of operating conditions. Using the reduced models the main loss process was identified to be the contact resistance of the wiring (accounting for about 60% of the overall losses) followed by the ionic conductivity of the electrolyte (30%). The electronic conductivity of the electrolyte was predicted to play a minor role at typical operating conditions, but was predicted to become the dominant process at temperatures beyond 1400 K. Based on a parameter variation an improved cell design was proposed where a thin electrolyte and a better contact strategy should be applied. The simulations predict a potential increase of cell power density of 80% based on these improvements.

Conclusion. The main focus of this work was to identify the elementary processes governing SOFC performance on a cell level. Based on the elementary kinetic study on model anodes, hydrogen spillover reactions were found to be the most probable pathway for charge-transfer in Ni/YSZ materials systems and that surface diffusion and kinetics on the electrolyte are rate-co-limiting. In the studies on direct flame fuel cells it was shown that a hydrogen spillover reaction may even account for the oxidation of carbon monoxide via water-gas-shift-reactions. In the DFFC system study the wiring of the cell caused the main performance loss and impeded a more detailed analysation.

Ongoing research. For both, model anodes and DFFC system, guidelines for further experiments were given. In case of the Ni/YSZ system, further validation of the model parameters (diffusion coefficients on the surfaces, thermodynamic properties of surface species) and experimental characterisation under cathodic polarisation and a focus on the dependence of the polarisation behaviour on the partial pressure of hydrogen are subject to a current research project of our research group. To continue studies on the direct flame

fuel cell, the proposed improvements of the cell design will first have to be realised by our industry partner.

Acknowledgments

First and foremost, I would like to thank my supervisors. I thank Priv. Doz. Wolfgang Bessler for his excellent scientific mentorship. I thank Prof. Annemarie Pucci who showed great interest in my projects over the last three years and offered me the possibility to do my PhD within the faculty of Physics.

I would like to thank the researches in the field: Dr. Anja Bieberle-Hütter for providing the experimental data base on model anodes, Helmut Kronemayer and Daniel Barzan who did a great job characterising the DFFC.

I greatly acknowledge the help and the patient support I got from my working colleagues at the IWR, Dr. Stefan Gewies, Jens Marquetand, Nicolas Bayer-Botero, Christian Hellwig and all members of the "reacting flows" research group.

This thesis was financially supported by Shinko Eletric Industries, Nagano, Japan, Deutsche Forschungsgemeinschaft (DFG, German Research Foundation) grant no. BE 3819/1-1 and by Prof. Warnatz.

Finally, I thank my family for all their comprehension: Vielen, vielen Dank an euch, Lela, Zoë und Caja, für euer Lächeln, eure Zuneigung und euer Verständnis.

Appendix A

Thermodynamic data of interstitial species

In this Appendix the derivation of the thermodynamic data of the interstitial species is described.

A.1 Hydrogen in YSZ

In 1968 Wagner et al. determined the solubility of interstitial protons in YSZ ($H^{\bullet}_{i\,YSZ}$). Assuming a global reaction of the form

$$H_2O_{gas} + V^{\bullet\bullet}_{O\,YSZ} \rightleftharpoons 2\,H^{\bullet}_{i\,YSZ} + O^{X}_{O\,YSZ}\ , \tag{A.1}$$

it is possible to extract thermodynamic data from concentration measurements of $H^{\bullet}_{i\,YSZ}$ versus temperature. From mass-action kinetics and the above mentioned global reaction, it follows that,

$$\exp\left(-\frac{\Delta G}{RT}\right) = \frac{a\left(H^{\bullet}_{i\,YSZ}\right)^2 \cdot a\left(O^{X}_{O\,YSZ}\right)}{a\left(H_2O_{gas}\right) \cdot a\left(V^{\bullet\bullet}_{O\,YSZ}\right)} \quad . \tag{A.2}$$

Solving this equation for the activity of $H^{\bullet}_{i\,YSZ}$ we get

$$a\left(H^{\bullet}_{i\,YSZ}\right) = \sqrt{\exp\left(-\frac{\Delta G}{RT}\right) \cdot \frac{a\left(V^{\bullet\bullet}_{O\,YSZ}\right)}{a\left(O^{X}_{O\,YSZ}\right)} \cdot a\left(H_2O_{gas}\right)} \quad . \tag{A.3}$$

The free enthalpy of reaction ΔG can be written as

$$\Delta G = 2 \cdot \Delta G\left(H^{\bullet}_{i\,YSZ}\right) + \Delta G\left(O^{X}_{O\,YSZ}\right) - \Delta G\left(H_2O\right) - \Delta G\left(V^{\bullet\bullet}_{O\,YSZ}\right) \quad . \tag{A.4}$$

Replacing ΔG in Eq. A.2 with this relation yields, after some algebraic manipulation, the relation,

$$\Delta G\left(\mathrm{H}^{\bullet}_{\mathrm{i\,YSZ}}\right) = -\frac{RT}{2}\cdot\ln\left(\frac{a\left(\mathrm{H}^{\bullet}_{\mathrm{i\,YSZ}}\right)^{2}\cdot a\left(\mathrm{O}^{\mathrm{X}}_{\mathrm{O\,YSZ}}\right)}{a\left(\mathrm{H_2O_{gas}}\right)\cdot a\left(\mathrm{V}^{\bullet\bullet}_{\mathrm{O\,YSZ}}\right)}\right) \tag{A.5}$$

$$+\frac{1}{2}\cdot\left(\Delta G\left(\mathrm{H_2O_{gas}}\right)+\Delta G\left(\mathrm{V}^{\bullet\bullet}_{\mathrm{O\,YSZ}}\right)-\Delta G\left(\mathrm{O}^{\mathrm{X}}_{\mathrm{O\,YSZ}}\right)\right) \tag{A.6}$$

Using the temperature dependent values for $a\left(\mathrm{H}^{\bullet}_{\mathrm{i\,YSZ}}\right)$ measured by Wagner et al. [93] and the above relation, allows for the determination of $\Delta S\left(\mathrm{H}^{\bullet}_{\mathrm{i\,YSZ}}\right)$ and $\Delta H\left(\mathrm{H}^{\bullet}_{\mathrm{i\,YSZ}}\right)$ via

$$\Delta G = \Delta H - T\cdot\Delta S \quad .$$

The numerical values are:

$$\begin{aligned}\Delta S\left(\mathrm{H}^{\bullet}_{\mathrm{i\,YSZ}}\right) &= 64.5\,\frac{\mathrm{J}}{\mathrm{mol}}\\ \Delta H\left(\mathrm{H}^{\bullet}_{\mathrm{i\,YSZ}}\right) &= 16.4\,\frac{\mathrm{kJ}}{\mathrm{mol}} \quad .\end{aligned}$$

In this calculations the enthalpy of formation of bulk vacancies is set to zero ($\Delta H\left(\mathrm{O}^{\mathrm{X}}_{\mathrm{O\,YSZ}}\right)\equiv 0$) to be consistent with the description of the free surface sites.

The doping of ZrO_2 with YO_3 results in a stabilization of the cubic phase. Assuming a CaF_2 face-centered cubic structure and an accommodation of an interstitial proton at the octahedral site of a unit cell, we can calculate the maximum concentration $c^{\mathrm{sat}}_{\mathrm{H}^{\bullet}_{\mathrm{i\,YSZ}}}$ of $\mathrm{H}^{\bullet}_{\mathrm{i\,YSZ}}$ solvable in YSZ via

$$c^{\mathrm{sat}}_{\mathrm{H}^{\bullet}_{\mathrm{i\,YSZ}}} = \frac{1}{4}\cdot\rho_{\mathrm{YSZ}}\ ,$$

were $\rho_{\mathrm{YSZ}} = 0.05\ {}^{\mathrm{mol}}/_{\mathrm{cm^3}}$ is the molar density of YSZ. This yields a density of intersitital hydrogen in YSZ of:

$$\rho_{\mathrm{H}^{\bullet}_{\mathrm{i\,YSZ}}} = 1.25\cdot 10^{4}\,\frac{\mathrm{mol}}{\mathrm{m^3}} \quad .$$

.

A.2 Hydrogen in nickel

Interstitial hydrogen in nickel $\mathrm{H}^{\mathrm{x}}_{\mathrm{i\,Ni}}$ is located at the octahedral site [92]. Consequently, the maximum ratio of interstitial hydrogen to lattice nickel is 1:4. Given the molar volume of a nickel single crystal $\overline{v_{\mathrm{Ni}}} = 6.59\,{}^{\mathrm{cm^3}}/_{\mathrm{mol}}$ the maxi-

mum concentration of $H^{x}_{i\,Ni}$ in nickel is :

$$c^{sat}_{H^{x}_{i\,Ni}} = 3.8 \cdot 10^{4}\,\frac{mol}{m^{3}} \quad .$$

To determine the thermodynamic properties of $H^{x}_{i\,Ni}$ solved in nickel, data from McLellan et al. [92] were analysed. McLellan et al. equilibrated polycrystalline nickel samples in a pure hydrogen atmosphere at standard pressure. They quenched the sample and measured the amount hydrogen solved in the bulk. The repetition of this measurement at different temperatures yields the relation of hydrogen solved in nickel versus the temperature. If we assume the global reaction

$$H_{2,gas} \rightleftharpoons 2\,H^{x}_{i\,Ni} \quad ,$$

mass-action kinetics predict for the thermodynamic equilibrium the equality

$$-\Delta G = RT \cdot \ln\left(\frac{a\,(H^{x}_{i\,Ni})^{2}}{a\,(H_{2,gas})}\right) \quad .$$

Solving this equation for the activity of interstitial hydrogen and fitting the resulting function to the experimental data, yields the molar formation entropy and enthalpy of $H^{x}_{i\,Ni}$ with respect to $H_{2,gas}$ at standard conditions:

$$\Delta S_{H^{x}_{i\,Ni}} = 43\,\frac{J}{mol} \quad ; \Delta H_{H^{x}_{i\,Ni}} = 36\,\frac{kJ}{mol} \quad .$$

Appendix B

DFFC supplementary information

B.1 Ionic conductivity of the SDC electrolyte

To extend the temperature range of the experimentally derived data for the ionic conductivity of SDC provided by Shinko Electric Industies Co. Ltd. and to literature data by Jung et al. [132] Fig. B.1 shows a comparison between two experimental data sets and an analytical fit.

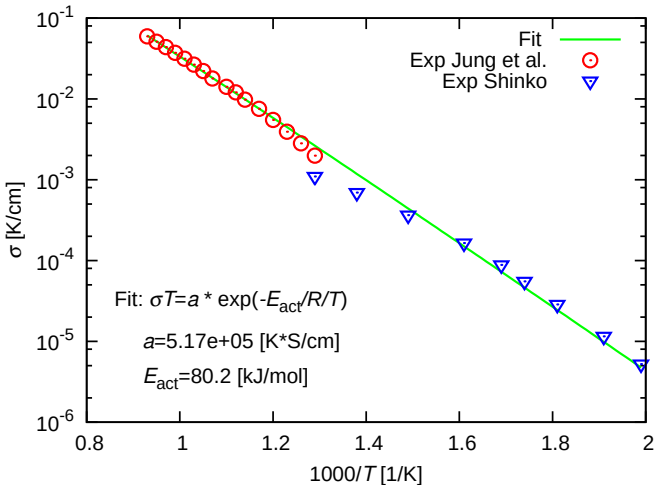

Figure B.1: *Comparison between fitted model equation for the ionic conductivity of SDC, experimental data of Shinko Electric Industies Co. Ltd. and literature data [132].*

B.2 Tabulated reaction mechanism

B.2.1 DFFC gas-phase mechanisms

The following GRI-Mech 3.0 mechanism is used for the flame chemistry [127]. It includes hydrocarbons up to a chain length of C_3 and can be used to simu-

late methane, ethane, propane, and natural gas combustion. The mechanism also includes nitrogen species and reactions (such as NO) that allow the simulation of nitric oxide pollutant formation; because we are not interested in this, we have excluded all nitrogen reactions. The remaining mechanism consists of 219 reactions between 36 species. This table contains the reaction equation, the preexponential factor, the temperature exponent, and the activation energy, as well as Troe pressure-dependent factors. See [50, 127] for details.

Reaction									k^0	β	E^{act}
O	+	O	+	M001	⇌	O2	+	M001	1.200E+017	-1.000	0.000
O	+	H	+	M002	⇌	OH	+	M002	5.000E+017	-1.000	0.000
O	+	H2	⇌	H	+	OH			3.870E+004	2.700	26.209
O	+	HO2	⇌	OH	+	O2			2.000E+013	0.000	0.000
O	+	H2O2	⇌	OH	+	HO2			9.630E+006	2.000	16.747
O	+	CH	⇌	H	+	CO			5.700E+013	0.000	0.000
O	+	CH2	⇌	H	+	HCO			8.000E+013	0.000	0.000
O	+	CH2(S)	⇌	H2	+	CO			1.500E+013	0.000	0.000
O	+	CH2(S)	⇌	H	+	HCO			1.500E+013	0.000	0.000
O	+	CH3	⇌	H	+	CH2O			5.060E+013	0.000	0.000
O	+	CH4	⇌	OH	+	CH3			1.020E+009	1.500	36.006
O	+	CO	+	M003	⇌	CO2	+	M003	1.800E+010	0.000	9.986
		LOW		6.020E+014		0.000		12.560			
		TROE		0.5000		1.E30		1.E30	1.E30		
O	+	HCO	⇌	OH	+	CO			3.000E+013	0.000	0.000
O	+	HCO	⇌	H	+	CO2			3.000E+013	0.000	0.000
O	+	CH2O	⇌	OH	+	HCO			3.900E+013	0.000	14.821
O	+	CH2OH	⇌	OH	+	CH2O			1.000E+013	0.000	0.000
O	+	CH3O	⇌	OH	+	CH2O			1.000E+013	0.000	0.000
O	+	CH3OH	⇌	OH	+	CH2OH			3.880E+005	2.500	12.979
O	+	CH3OH	⇌	OH	+	CH3O			1.300E+005	2.500	20.934
O	+	C2H	⇌	CH	+	CO			5.000E+013	0.000	0.000
O	+	C2H2	⇌	H	+	HCCO			1.350E+007	2.000	7.955
O	+	C2H2	⇌	OH	+	C2H			4.600E+019	-1.410	121.208
O	+	C2H2	⇌	CO	+	CH2			6.940E+006	2.000	7.955
O	+	C2H3	⇌	H	+	CH2CO			3.000E+013	0.000	0.000
O	+	C2H4	⇌	CH3	+	HCO			1.250E+007	1.830	0.921
O	+	C2H5	⇌	CH3	+	CH2O			2.240E+013	0.000	0.000
O	+	C2H6	⇌	OH	+	C2H5			8.980E+007	1.920	23.823
O	+	HCCO	⇌	H	+	CO	+	CO	1.000E+014	0.000	0.000
O	+	CH2CO	⇌	OH	+	HCCO			1.000E+013	0.000	33.494
O	+	CH2CO	⇌	CH2	+	CO2			1.750E+012	0.000	5.652
O2	+	CO	⇌	O	+	CO2			2.500E+012	0.000	200.129
O2	+	CH2O	⇌	HO2	+	HCO			1.000E+014	0.000	167.472
H	+	O2	+	M004	⇌	HO2	+	M004	2.800E+018	-0.860	0.000
H	+	O2	+	O2	⇌	HO2	+	O2	2.080E+019	-1.240	0.000
H	+	O2	+	H2O	⇌	HO2	+	H2O	1.126E+019	-0.760	0.000
H	+	O2	+	N2	⇌	HO2	+	N2	2.600E+019	-1.240	0.000
H	+	O2	+	AR	⇌	HO2	+	AR	7.000E+017	-0.800	0.000
H	+	O2	⇌	O	+	OH			2.650E+016	-0.671	71.347
H	+	H	+	M005	⇌	H2	+	M005	1.000E+018	-1.000	0.000
H	+	H	+	H2	⇌	H2	+	H2	9.000E+016	-0.600	0.000
H	+	H	+	H2O	⇌	H2	+	H2O	6.000E+019	-1.250	0.000
H	+	H	+	CO2	⇌	H2	+	CO2	5.500E+020	-2.000	0.000
H	+	OH	+	M006	⇌	H2O	+	M006	2.200E+022	-2.000	0.000
H	+	HO2	⇌	O	+	H2O			3.970E+012	0.000	2.809
H	+	HO2	⇌	O2	+	H2			4.480E+013	0.000	4.472
H	+	HO2	⇌	OH	+	OH			8.400E+013	0.000	2.659
H	+	H2O2	⇌	HO2	+	H2			1.210E+007	2.000	21.771
H	+	H2O2	⇌	OH	+	H2O			1.000E+013	0.000	15.072
H	+	CH	⇌	C	+	H2			1.650E+014	0.000	0.000
H	+	CH2	+	M007	⇌	CH3	+	M007	6.000E+014	0.000	0.000
		LOW		1.040E+026		-2.760		6.699			
		TROE		0.5620		91.0		5836.0	8552.0		
H	+	CH2(S)	⇌	CH	+	H2			3.000E+013	0.000	0.000
H	+	CH3	+	M008	⇌	CH4	+	M008	1.390E+016	-0.534	2.244

Reaction									k^0	β	E^{act}
		LOW		2.620E+033		-4.760		10.216			
		TROE		0.7830		74.0		2941.0	6964.0		
H	+	CH4	⇌	CH3	+	H2			6.600E+008	1.620	45.385
H	+	HCO	+	M009	⇌	CH2O	+	M009	1.090E+012	0.480	-1.089
		LOW		2.470E+024		-2.570		1.779			
		TROE		0.7824		271.0		2755.0	6570.0		
H	+	HCO	⇌	H2	+	CO			7.340E+013	0.000	0.000
H	+	CH2O	+	M010	⇌	CH2OH	+	M010	5.400E+011	0.454	15.072
		LOW		1.270E+032		-4.820		27.340			
		TROE		0.7187		103.0		1291.0	4160.0		
H	+	CH2O	+	M011	⇌	CH3O	+	M011	5.400E+011	0.454	10.886
		LOW		2.200E+030		-4.800		23.279			
		TROE		0.7580		94.0		1555.0	4200.0		
H	+	CH2O	⇌	HCO	+	H2			5.740E+007	1.900	11.480
H	+	CH2OH	+	M012	⇌	CH3OH	+	M012	1.055E+012	0.500	0.360
		LOW		4.360E+031		-4.650		21.269			
		TROE		0.6000		100.0		90000.0	10000.0		
H	+	CH2OH	⇌	H2	+	CH2O			2.000E+013	0.000	0.000
H	+	CH2OH	⇌	OH	+	CH3			1.650E+011	0.650	-1.189
H	+	CH2OH	⇌	CH2(S)	+	H2O			3.280E+013	-0.090	2.554
H	+	CH3O	+	M013	⇌	CH3OH	+	M013	2.430E+012	0.515	0.209
		LOW		4.660E+041		-7.440		58.950			
		TROE		0.7000		100.0		90000.0	10000.0		
H	+	CH3O	⇌	H	+	CH2OH			4.150E+007	1.630	8.055
H	+	CH3O	⇌	H2	+	CH2O			2.000E+013	0.000	0.000
H	+	CH3O	⇌	OH	+	CH3			1.500E+012	0.500	-0.461
H	+	CH3O	⇌	CH2(S)	+	H2O			2.620E+014	-0.230	4.480
H	+	CH3OH	⇌	CH2OH	+	H2			1.700E+007	2.100	20.390
H	+	CH3OH	⇌	CH3O	+	H2			4.200E+006	2.100	20.390
H	+	C2H	+	M014	⇌	C2H2	+	M014	1.000E+017	-1.000	0.000
		LOW		3.750E+033		-4.800		7.955			
		TROE		0.6464		132.0		1315.0	5566.0		
H	+	C2H2	+	M015	⇌	C2H3	+	M015	5.600E+012	0.000	10.048
		LOW		3.800E+040		-7.270		30.229			
		TROE		0.7507		98.5		1302.0	4167.0		
H	+	C2H3	+	M016	⇌	C2H4	+	M016	6.080E+012	0.270	1.172
		LOW		1.400E+030		-3.860		13.900			
		TROE		0.7820		207.5		2663.0	6095.0		
H	+	C2H3	⇌	H2	+	C2H2			3.000E+013	0.000	0.000
H	+	C2H4	+	M017	⇌	C2H5	+	M017	5.400E+011	0.454	7.620
		LOW		6.000E+041		-7.620		29.182			
		TROE		0.9753		210.0		984.0	4374.0		
H	+	C2H4	⇌	C2H3	+	H2			1.325E+006	2.530	51.246
H	+	C2H5	+	M018	⇌	C2H6	+	M018	5.210E+017	-0.990	6.615
		LOW		1.990E+041		-7.080		27.989			
		TROE		0.8422		125.0		2219.0	6882.0		
H	+	C2H5	⇌	H2	+	C2H4			2.000E+012	0.000	0.000
H	+	C2H6	⇌	C2H5	+	H2			1.150E+008	1.900	31.527
H	+	HCCO	⇌	CH2(S)	+	CO			1.000E+014	0.000	0.000
H	+	CH2CO	⇌	HCCO	+	H2			5.000E+013	0.000	33.494
H	+	CH2CO	⇌	CH3	+	CO			1.130E+013	0.000	14.352
H	+	HCCOH	⇌	H	+	CH2CO			1.000E+013	0.000	0.000
H2	+	CO	+	M019	⇌	CH2O	+	M019	4.300E+007	1.500	333.269
		LOW		5.070E+027		-3.420		353.157			
		TROE		0.9320		197.0		1540.0	10300.0		
OH	+	H2	⇌	H	+	H2O			2.160E+008	1.510	14.361
OH	+	OH	+	M020	⇌	H2O2	+	M020	7.400E+013	-0.370	0.000
		LOW		2.300E+018		-0.900		-7.118			
		TROE		0.7346		94.0		1756.0	5182.0		
OH	+	OH	⇌	O	+	H2O			3.570E+004	2.400	-8.834
OH	+	HO2	⇌	O2	+	H2O			1.450E+013	0.000	-2.093
OH	+	H2O2	⇌	HO2	+	H2O			2.000E+012	0.000	1.788
OH	+	H2O2	⇌	HO2	+	H2O			1.700E+018	0.000	123.134
OH	+	C	⇌	H	+	CO			5.000E+013	0.000	0.000
OH	+	CH	⇌	H	+	HCO			3.000E+013	0.000	0.000
OH	+	CH2	⇌	H	+	CH2O			2.000E+013	0.000	0.000
OH	+	CH2	⇌	CH	+	H2O			1.130E+007	2.000	12.560
OH	+	CH2(S)	⇌	H	+	CH2O			3.000E+013	0.000	0.000
OH	+	CH3	+	M021	⇌	CH3OH	+	M021	2.790E+018	-1.430	5.568
		LOW		4.000E+036		-5.920		13.147			
		TROE		0.4120		195.0		5900.0	6394.0		

Reaction									k^0	β	E^{act}
OH	+	CH3	⇌	CH2	+	H2O			5.600E+007	1.600	22.692
OH	+	CH3	⇌	CH2(S)	+	H2O			6.440E+017	-1.340	5.933
OH	+	CH4	⇌	CH3	+	H2O			1.000E+008	1.600	13.063
OH	+	CO	⇌	H	+	CO2			4.760E+007	1.228	0.293
OH	+	HCO	⇌	H2O	+	CO			5.000E+013	0.000	0.000
OH	+	CH2O	⇌	HCO	+	H2O			3.430E+009	1.180	-1.871
OH	+	CH2OH	⇌	H2O	+	CH2O			5.000E+012	0.000	0.000
OH	+	CH3O	⇌	H2O	+	CH2O			5.000E+012	0.000	0.000
OH	+	CH3OH	⇌	CH2OH	+	H2O			1.440E+006	2.000	-3.517
OH	+	CH3OH	⇌	CH3O	+	H2O			6.300E+006	2.000	6.280
OH	+	C2H	⇌	H	+	HCCO			2.000E+013	0.000	0.000
OH	+	C2H2	⇌	H	+	CH2CO			2.180E-004	4.500	-4.187
OH	+	C2H2	⇌	H	+	HCCOH			5.040E+005	2.300	56.522
OH	+	C2H2	⇌	C2H	+	H2O			3.370E+007	2.000	58.615
OH	+	C2H2	⇌	CH3	+	CO			4.830E-004	4.000	-8.374
OH	+	C2H3	⇌	H2O	+	C2H2			5.000E+012	0.000	0.000
OH	+	C2H4	⇌	C2H3	+	H2O			3.600E+006	2.000	10.467
OH	+	C2H6	⇌	C2H5	+	H2O			3.540E+006	2.120	3.643
OH	+	CH2CO	⇌	HCCO	+	H2O			7.500E+012	0.000	8.374
HO2	+	HO2	⇌	O2	+	H2O2			1.300E+011	0.000	-6.824
HO2	+	HO2	⇌	O2	+	H2O2			4.200E+014	0.000	50.242
HO2	+	CH2	⇌	OH	+	CH2O			2.000E+013	0.000	0.000
HO2	+	CH3	⇌	O2	+	CH4			1.000E+012	0.000	0.000
HO2	+	CH3	⇌	OH	+	CH3O			3.780E+013	0.000	0.000
HO2	+	CO	⇌	OH	+	CO2			1.500E+014	0.000	98.808
HO2	+	CH2O	⇌	HCO	+	H2O2			5.600E+006	2.000	50.242
C	+	O2	⇌	O	+	CO			5.800E+013	0.000	2.412
C	+	CH2	⇌	H	+	C2H			5.000E+013	0.000	0.000
C	+	CH3	⇌	H	+	C2H2			5.000E+013	0.000	0.000
CH	+	O2	⇌	O	+	HCO			6.710E+013	0.000	0.000
CH	+	H2	⇌	H	+	CH2			1.080E+014	0.000	13.021
CH	+	H2O	⇌	H	+	CH2O			5.710E+012	0.000	-3.161
CH	+	CH2	⇌	H	+	C2H2			4.000E+013	0.000	0.000
CH	+	CH3	⇌	H	+	C2H3			3.000E+013	0.000	0.000
CH	+	CH4	⇌	H	+	C2H4			6.000E+013	0.000	0.000
CH	+	CO	+	M022	⇌	HCCO	+	M022	5.000E+013	0.000	0.000
		LOW		2.690E+028		-3.740		8.106			
		TROE		0.5757		237.0		1652.0	5069.0		
CH	+	CO2	⇌	HCO	+	CO			1.900E+014	0.000	66.118
CH	+	CH2O	⇌	H	+	CH2CO			9.460E+013	0.000	-2.156
CH	+	HCCO	⇌	CO	+	C2H2			5.000E+013	0.000	0.000
CH2	+	O2	→	OH	+	H	+	CO	5.000E+012	0.000	6.280
CH2	+	H2	⇌	H	+	CH3			5.000E+005	2.000	30.271
CH2	+	CH2	⇌	H2	+	C2H2			1.600E+015	0.000	50.007
CH2	+	CH3	⇌	H	+	C2H4			4.000E+013	0.000	0.000
CH2	+	CH4	⇌	CH3	+	CH3			2.460E+006	2.000	34.625
CH2	+	CO	+	M023	⇌	CH2CO	+	M023	8.100E+011	0.500	18.882
		LOW		2.690E+033		-5.110		29.705			
		TROE		0.5907		275.0		1226.0	5185.0		
CH2	+	HCCO	⇌	C2H3	+	CO			3.000E+013	0.000	0.000
CH2(S)	+	N2	⇌	CH2	+	N2			1.500E+013	0.000	2.512
CH2(S)	+	AR	⇌	CH2	+	AR			9.000E+012	0.000	2.512
CH2(S)	+	O2	⇌	H	+	OH	+	CO	2.800E+013	0.000	0.000
CH2(S)	+	O2	⇌	CO	+	H2O			1.200E+013	0.000	0.000
CH2(S)	+	H2	⇌	CH3	+	H			7.000E+013	0.000	0.000
CH2(S)	+	H2O	+	M024	⇌	CH3OH	+	M024	4.820E+017	-1.160	4.794
		LOW		1.880E+038		-6.360		21.101			
		TROE		0.6027		208.0		3922.0	10180.0		
CH2(S)	+	H2O	⇌	CH2	+	H2O			3.000E+013	0.000	0.000
CH2(S)	+	CH3	⇌	H	+	C2H4			1.200E+013	0.000	-2.386
CH2(S)	+	CH4	⇌	CH3	+	CH3			1.600E+013	0.000	-2.386
CH2(S)	+	CO	⇌	CH2	+	CO			9.000E+012	0.000	0.000
CH2(S)	+	CO2	⇌	CH2	+	CO2			7.000E+012	0.000	0.000
CH2(S)	+	CO2	⇌	CO	+	CH2O			1.400E+013	0.000	0.000
CH2(S)	+	C2H6	⇌	CH3	+	C2H5			4.000E+013	0.000	-2.303
CH3	+	O2	⇌	O	+	CH3O			3.560E+013	0.000	127.614
CH3	+	O2	⇌	OH	+	CH2O			2.310E+012	0.000	85.055
CH3	+	H2O2	⇌	HO2	+	CH4			2.450E+004	2.470	21.688
CH3	+	CH3	+	M025	⇌	C2H6	+	M025	6.770E+016	-1.180	2.738
		LOW		3.400E+041		-7.030		11.564			
		TROE		0.6190		73.2		1180.0	9999.0		

Reaction									k^0	β	E^{act}
CH3	+	CH3	⇌	H	+	C2H5			6.840E+012	0.100	44.380
CH3	+	HCO	⇌	CH4	+	CO			2.648E+013	0.000	0.000
CH3	+	CH2O	⇌	HCO	+	CH4			3.320E+003	2.810	24.535
CH3	+	CH3OH	⇌	CH2OH	+	CH4			3.000E+007	1.500	41.617
CH3	+	CH3OH	⇌	CH3O	+	CH4			1.000E+007	1.500	41.617
CH3	+	C2H4	⇌	C2H3	+	CH4			2.270E+005	2.000	38.519
CH3	+	C2H6	⇌	C2H5	+	CH4			6.140E+006	1.740	43.752
HCO	+	H2O	⇌	H	+	CO	+	H2O	1.500E+018	-1.000	71.176
HCO	+	M026	⇌	H	+	CO	+	M026	1.870E+017	-1.000	71.176
HCO	+	O2	⇌	HO2	+	CO			1.345E+013	0.000	1.675
CH2OH	+	O2	⇌	HO2	+	CH2O			1.800E+013	0.000	3.768
CH3O	+	O2	⇌	HO2	+	CH2O			4.280E-013	7.600	-14.779
C2H	+	O2	⇌	HCO	+	CO			1.000E+013	0.000	-3.161
C2H	+	H2	⇌	H	+	C2H2			5.680E+010	0.900	8.344
C2H3	+	O2	⇌	HCO	+	CH2O			4.580E+016	-1.390	4.250
C2H4	+	M027	⇌	H2	+	C2H2	+	M027	8.000E+012	0.440	363.289
		LOW		1.580E+051		-9.300		409.469			
		TROE		0.7345		180.0		1035.0	5417.0		
C2H5	+	O2	⇌	HO2	+	C2H4			8.400E+011	0.000	16.224
HCCO	+	O2	⇌	OH	+	CO	+	CO	3.200E+012	0.000	3.576
HCCO	+	HCCO	⇌	CO	+	CO	+	C2H2	1.000E+013	0.000	0.000
O	+	CH3	⇀	H	+	H2	+	CO	3.370E+013	0.000	0.000
O	+	C2H4	⇌	H	+	CH2CHO			6.700E+006	1.830	0.921
O	+	C2H5	⇌	H	+	CH3CHO			1.096E+014	0.000	0.000
OH	+	HO2	⇌	O2	+	H2O			5.000E+015	0.000	72.557
OH	+	CH3	⇀	H2	+	CH2O			8.000E+009	0.500	-7.348
CH	+	H2	+	M037	⇌	CH3	+	M037	1.970E+012	0.430	-1.549
		LOW		4.820E+025		-2.800		2.470			
		TROE		0.5780		122.0		2535.0	9365.0		
CH2	+	O2	⇀	H	+	H	+	CO2	5.800E+012	0.000	6.280
CH2	+	O2	⇌	O	+	CH2O			2.400E+012	0.000	6.280
CH2	+	CH2	⇀	H	+	H	+	C2H2	2.000E+014	0.000	46.009
CH2(S)	+	H2O	⇀	H2	+	CH2O			6.820E+010	0.250	-3.915
C2H3	+	O2	⇌	O	+	CH2CHO			3.030E+011	0.290	0.046
C2H3	+	O2	⇌	HO2	+	C2H2			1.337E+006	1.610	-1.608
O	+	CH3CHO	⇌	OH	+	CH2CHO			2.920E+012	0.000	7.570
O	+	CH3CHO	⇀	OH	+	CH3	+	CO	2.920E+012	0.000	7.570
O2	+	CH3CHO	⇀	HO2	+	CH3	+	CO	3.010E+013	0.000	163.913
H	+	CH3CHO	⇌	CH2CHO	+	H2			2.050E+009	1.160	10.069
H	+	CH3CHO	⇀	CH3	+	H2	+	CO	2.050E+009	1.160	10.069
OH	+	CH3CHO	⇀	CH3	+	H2O	+	CO	2.343E+010	0.730	-4.660
HO2	+	CH3CHO	⇀	CH3	+	H2O2	+	CO	3.010E+012	0.000	49.919
CH3	+	CH3CHO	⇀	CH3	+	CH4	+	CO	2.720E+006	1.770	24.786
H	+	CH2CO	+	M038	⇌	CH2CHO	+	M038	4.865E+011	0.422	-7.348
		LOW		1.012E+042		-7.630		16.136			
		TROE		0.4650		201.0		1773.0	5333.0		
O	+	CH2CHO	⇀	H	+	CH2	+	CO2	1.500E+014	0.000	0.000
O2	+	CH2CHO	⇀	OH	+	CO	+	CH2O	1.810E+010	0.000	0.000
O2	+	CH2CHO	⇀	OH	+	HCO	+	HCO	2.350E+010	0.000	0.000
H	+	CH2CHO	⇌	CH3	+	HCO			2.200E+013	0.000	0.000
H	+	CH2CHO	⇌	CH2CO	+	H2			1.100E+013	0.000	0.000
OH	+	CH2CHO	⇌	H2O	+	CH2CO			1.200E+013	0.000	0.000
OH	+	CH2CHO	⇌	HCO	+	CH2OH			3.010E+013	0.000	0.000
CH3	+	C2H5	+	M039	⇌	C3H8	+	M039	9.430E+012	0.000	0.000
		LOW		2.710E+074		16.820		54.701			
		TROE		0.1527		291.0		2742.0	7748.0		
O	+	C3H8	⇌	OH	+	C3H7			1.930E+005	2.680	15.558
H	+	C3H8	⇌	C3H7	+	H2			1.320E+006	2.540	28.286
OH	+	C3H8	⇌	C3H7	+	H2O			3.160E+007	1.800	3.910
C3H7	+	H2O2	⇌	HO2	+	C3H8			3.780E+002	2.720	6.280
CH3	+	C3H8	⇌	C3H7	+	CH4			9.030E-001	3.650	29.952
CH3	+	C2H4	+	M040	⇌	C3H7	+	M040	2.550E+006	1.600	23.865
		LOW		3.000E+063		14.600		76.074			
		TROE		0.1894		277.0		8748.0	7891.0		
O	+	C3H7	⇌	C2H5	+	CH2O			9.640E+013	0.000	0.000
H	+	C3H7	+	M041	⇌	C3H8	+	M041	3.613E+013	0.000	0.000
		LOW		4.420E+061		13.545		47.549			
		TROE		0.3150		369.0		3285.0	6667.0		
H	+	C3H7	⇌	CH3	+	C2H5			4.060E+006	2.190	3.726
OH	+	C3H7	⇌	C2H5	+	CH2OH			2.410E+013	0.000	0.000
HO2	+	C3H7	⇌	O2	+	C3H8			2.550E+010	0.255	-3.948

Reaction									k^0	β	E^{act}
HO2	+	C3H7	⇀	OH	+	C2H5	+	CH2O	2.410E+013	0.000	0.000
CH3	+	C3H7	⇌	C2H5	+	C2H5			1.927E+013	-0.320	0.000

B.2.2 DFFC electrode surface mechanism

The elementary kinetic reaction mechanisms used for describing nickel surface reactions is based on the work of Hecht et al. [36], consisting of 42 reactions between 6 gas-phase (H_2, CO, H_2O, CO_2, CH_4, O_2) and 12 surface-adsorbed species. This mechanism is given in the following (taken from [36]). For the present study, it was extented by adsorption reactions of all other radical species present in the gas-phase mechanism. They were assigned a sticking probability of unity, which is a reasonable assumption for radical species.

Reaction									k^0	β	E^{act}
STICK											
H2	+	NI(NI)	+	NI(NI)	⇀	H(NI)	+	H(NI)	0.010E-00	0.0	0.0
STICK											
O2	+	NI(NI)	+	NI(NI)	⇀	O(NI)	+	O(NI)	0.010E-00	0.0	0.0
STICK											
CH4	+	NI(NI)	⇀	CH4(NI)					8.000E-03	0.0	0.0
STICK											
H2O	+	NI(NI)	⇀	H2O(NI)					1.000E-01	0.0	0.0
STICK											
CO2	+	NI(NI)	⇀	CO2(NI)					1.000E-05	0.0	0.0
STICK											
CO	+	NI(NI)	⇀	CO(NI)					5.000E-01	0.0	0.0
STICK											
OH	+	NI(NI)	⇀	OH(NI)					1.000E-00	0.0	0.0
STICK											
CH	+	NI(NI)	⇀	CH(NI)					1.000E-00	0.0	0.0
STICK											
O	+	NI(NI)	⇀	O(NI)					1.000E-00	0.0	0.0
STICK											
H	+	NI(NI)	⇀	H(NI)					1.000E-00	0.0	0.0
STICK											
HCO	+	NI(NI)	+	NI(NI)	⇀	CH(NI)	+	O(NI)	1.000E-00	0.0	0.0
STICK											
CH3	+	NI(NI)	⇀	CH3(NI)					1.000E-00	0.0	0.0
H(NI)	+	H(NI)	⇀	NI(NI)	+	NI(NI)	+	H2	3.000E+21	0.0	77.8
O(NI)	+	O(NI)	⇀	NI(NI)	+	NI(NI)	+	O2	1.300E+22	0.0	355.2
H2O(NI)			⇀	H2O	+	NI(NI)			3.000E+13	0.0	45.0
CO(NI)			⇀	CO	+	NI(NI)			3.500E+13	0.0	133.4
CO2(NI)			⇀	CO2	+	NI(NI)			1.000E+13	0.0	21.7
CH4(NI)			⇀	CH4	+	NI(NI)			1.000E+13	0.0	25.1
H(NI)	+	O(NI)	⇀	OH(NI)	+	NI(NI)			5.000E+22	0.0	83.7
OH(NI)	+	NI(NI)	⇀	H(NI)	+	O(NI)			3.000E+20	0.0	37.7
H(NI)	+	OH(NI)	⇀	H2O(NI)	+	NI(NI)			3.000E+20	0.0	33.5
H2O(NI)	+	NI(NI)	⇀	H(NI)	+	OH(NI)			5.000E+22	0.0	106.4
OH(NI)	+	OH(NI)	⇀	H2O(NI)	+	O(NI)			3.000E+21	0.0	100.8
H2O(NI)	+	O(NI)	⇀	OH(NI)	+	OH(NI)			3.000E+21	0.0	224.2
C(NI)	+	O(NI)	⇀	CO(NI)	+	NI(NI)			3.000E+22	0.0	97.9
CO(NI)	+	NI(NI)	⇀	C(NI)	+	O(NI)			2.500E+21	0.0	169.0
CO(NI)	+	O(NI)	⇀	CO2(NI)	+	NI(NI)			1.400E+20	0.0	121.6
CO2(NI)	+	NI(NI)	⇀	CO(NI)	+	O(NI)			3.000E+21	0.0	115.3
CH4(NI)	+	NI(NI)	⇀	CH3(NI)	+	H(NI)			3.700E+21	0.0	61.0
CH3(NI)	+	H(NI)	⇀	CH4(NI)	+	NI(NI)			3.700E+21	0.0	51.0
CH3(NI)	+	NI(NI)	⇀	CH2(NI)	+	H(NI)			3.700E+24	0.0	103.0
CH2(NI)	+	H(NI)	⇀	CH3(NI)	+	NI(NI)			3.700E+21	0.0	44.0
CH2(NI)	+	NI(NI)	⇀	CH(NI)	+	H(NI)			3.700E+24	0.0	100.0
CH(NI)	+	H(NI)	⇀	CH2(NI)	+	NI(NI)			3.700E+21	0.0	68.0
CH(NI)	+	NI(NI)	⇀	C(NI)	+	H(NI)			3.700E+21	0.0	21.0
C(NI)	+	H(NI)	⇀	CH(NI)	+	NI(NI)			3.700E+21	0.0	172.8

Reaction							k^0	β	E^{act}
CH4(NI)	+	O(NI)	⇀	CH3(NI)	+	OH(NI)	1.700E+24	0.0	80.3
CH3(NI)	+	OH(NI)	⇀	CH4(NI)	+	O(NI)	3.700E+21	0.0	24.3
CH3(NI)	+	O(NI)	⇀	CH2(NI)	+	OH(NI)	3.700E+24	0.0	120.3
CH2(NI)	+	OH(NI)	⇀	CH3(NI)	+	O(NI)	3.700E+21	0.0	15.1
CH2(NI)	+	O(NI)	⇀	CH(NI)	+	OH(NI)	3.700E+24	0.0	158.4
CH(NI)	+	OH(NI)	⇀	CH2(NI)	+	O(NI)	3.700E+21	0.0	36.8
CH(NI)	+	O(NI)	⇀	C(NI)	+	OH(NI)	3.700E+21	0.0	30.1
C(NI)	+	OH(NI)	⇀	CH(NI)	+	O(NI)	3.700E+21	0.0	145.5

Appendix C

Nusselt index law

The heat flux from a heated wall with temperature T_{wall} and a surface area A to a fluid with temperature T_{fluid} can be calculated by

$$\frac{\partial}{\partial t} Q_{\text{wall}} = A \cdot \alpha \cdot (T_{\text{wall}} - T_{\text{fluid}}) \,,$$

where α can follows from the Nusselt index law,

$$\alpha = Nu \cdot \frac{\lambda}{L} \,,$$

where Nu is the Nusselt number, L is the characteristic length and λ represents the heat conduction coefficient of the undisturbed fluid. For purely natural convection, $Nu = 1$. Consequently, the cooling rate, resulting from natural convection on the cathode side, with respect to ambient air, can be calculated by:

$$\frac{\partial}{\partial t} Q_{\text{wall}} = -\lambda \cdot \frac{A}{L} \cdot (T_{\text{wall}} - T_{\text{fluid}})$$

where $\lambda \approx 5.848 \cdot 10^{-2} \frac{\text{W}}{\text{m} \cdot \text{K}}$ is the heat conductivity of air, $L \approx 1.2 \cdot 10^{-2}\text{m}$ is the characteristic length, roughly equal to the diamtre, and T are the temperatures given in Kelvin [130].

Appendix D

List of symbols

Symbol	Unit	Meaning
A_k^{V}	$\mathrm{m^2/m^3}$	Volume-specific surface area of electrode component k
A_{cell}	$\mathrm{cm^2}$	Cell surface area
A_σ	$\mathrm{K/\Omega\,m}$	Preexponential factor of ionic conductivity
a_i		Activity of species i
a_0^{elyt}	$\mathrm{K/(\Omega{\cdot}m{\cdot}Pa^{1/4})}$	Preexponential factor electronic conductivity of the electrolyte
B	$\mathrm{m^2}$	Permeability of the porous electrode
b_0^{elyt}	$\mathrm{1/K}$	Temperature coefficient of electronic conductivity of the electrolyte
c_i	$\mathrm{mol/m^2}$	Surface concentration of species i
c_i	$\mathrm{mol/m^3}$	Gas-phase concentration of species i
c^{g}	$\mathrm{mol/m^3}$	Total gas-phase concentration
c_{q}	$\mathrm{J/K{\cdot}kg}$	Mass-specific heat capacity
d	m	Gap distance in stagnation-point flow
d	m	Pattern width
d_{P}	m	Average particle diameter
D_i	$\mathrm{m^2/s}$	Diffusion coefficient of species i
$\overline{D}_i$	$\mathrm{m^2/s}$	Mixture-averaged diffusion coefficient of species i
D_{ij}	$\mathrm{m^2/s}$	Binary diffusion coefficient of species i and j
D_{ij}^{eff}	$\mathrm{m^2/s}$	Effective binary diffusion coefficient
D_i^{K}	$\mathrm{m^2/s}$	Knudsen diffusion coefficient of species i
d_{elyt}	m	Thickness of the electrolyte layer

Symbol	Unit	Meaning
$E_{\mathrm{f,r}}^{\mathrm{act}}$	$^{\mathrm{J}}/_{\mathrm{mol}}$	Activation energy of chemical reaction (forward and reverse)
E	V	Cell voltage
E_σ	$^{\mathrm{J}}/_{\mathrm{mol}}$	Activation energy for ionic conductivity
F	$^{\mathrm{C}}/_{\mathrm{mol}}$	Faraday's constant
f		Friction factor in momentum equation
f_σ		Ratio of ionic conductivity of porous over bulk electrolyte
ΔG	$^{\mathrm{J}}/_{\mathrm{mol}}$	Free enthalpy of reaction
$\vec{g}$	$^{\mathrm{m}}/_{\mathrm{s}^2}$	Gravitational acceleration
h_i	$^{\mathrm{J}}/_{\mathrm{mol}}$	Molar enthalpy of species i
ΔH	$^{\mathrm{J}}/_{\mathrm{mol}}$	Enthalpy of reaction
h_{Ni}	m	Height of Ni pattern
i_0	$^{\mathrm{A}}/_{\mathrm{m}^3}$	Exchange current density
i^*	$^{\mathrm{A}}/_{\mathrm{m}^3}$	Exchange current density for modified Butler-Volmer
i_{cell}	$^{\mathrm{A}}/_{\mathrm{m}^2}$	Are-specific current density
i_{el}	$^{\mathrm{A}}/_{\mathrm{m}^2}$	Area-specific electronic current density through MIEC
$i_{\mathrm{F}}^{\mathrm{A}}$	$^{\mathrm{A}}/_{\mathrm{m}^2}$	Area-specific Faradaic current density
$i_{\mathrm{F}}^{\mathrm{V}}$	$^{\mathrm{A}}/_{\mathrm{m}^3}$	Volume-specific Faradaic current density
i_{tot}	$^{\mathrm{A}}/_{\mathrm{m}^2}$	Total current density
J_i^{diff}	$^{\mathrm{mol}}/_{\mathrm{m}^2\mathrm{s}}$	Molar diffusion flux of species i
J_i^{flow}	$^{\mathrm{mol}}/_{\mathrm{m}^2\mathrm{s}}$	Darcy flux of species i
j_i^{diff}	$^{\mathrm{kg}}/_{\mathrm{m}^2\mathrm{s}}$	Diffusive mass flux of species i
j_{q}	$^{\mathrm{J}}/_{\mathrm{m}^2\mathrm{s}}$	Heat flux
k_{ct}^0	$^{\mathrm{mol}}/_{\mathrm{m\,s}}$	Preexponential factor of charge-transfer reactions
k^0	$^{\mathrm{mol}}/_{\mathrm{m}^{\mathrm{n}}\mathrm{s}}$	Preexponential factor for chemical reactions (n = 1 to 5 depending on reaction)
$l_{\mathrm{TPB}}^{\mathrm{V}}$	$^{\mathrm{m}}/_{\mathrm{m}^3}$	Volume-specific three-phase boundary length
$l_{\mathrm{TPB}}^{\mathrm{A}}$	$^{\mathrm{m}}/_{\mathrm{m}^2}$	Area-specific three-phase boundary length
l_{con}	cm	Length of connecting wires
$\overline{M}$	$^{\mathrm{kg}}/_{\mathrm{mol}}$	Mean molar mass of gas mixtures
M_i	$^{\mathrm{kg}}/_{\mathrm{mol}}$	Molar mass of species i
P_{cell}	$^{\mathrm{W}}/_{\mathrm{m}^2}$	Power density

Symbol	Unit	Meaning
p	Pa	Pressure
p_i	Pa	Partial pressure of species i
p^0_{O2}	Pa	Temperature dependence modified Butler-Volmer[35]
R	$^{\mathrm{J}}/_{\mathrm{K\,mol}}$	Ideal gas constant
R	Ω	Resistance
R_{pol}	$\Omega\,\mathrm{cm}^2$	Polarisation resistance
S_{g}		Set of gas-phase species
ΔS	$^{\mathrm{J}}/_{\mathrm{K\,mol}}$	Entropy of reaction
$\dot{s}_i^{\mathrm{A}}$	$^{\mathrm{mol}}/_{\mathrm{m^2 s}}$	Surface-area-specific production rate
$\dot{s}_i^{\mathrm{V}}$	$^{\mathrm{mol}}/_{\mathrm{m^3 s}}$	Gas-phase-volume-specific production rate
T	K	Temperature
t	s	Time
U_{th}	V	Theoretical cell voltage
V	m^3	Volume
v	$^{\mathrm{m}}/_{\mathrm{s}}$	Velocity
v^{Stef}	$^{\mathrm{m}}/_{\mathrm{s}}$	Stefan velocity at electrode/gas-phase interface
X_i	%	Mole fraction of species i
$\mathrm{X_i}$	%	Gas-phase species i
Y_i	%	Mass fraction of species i
y	m	Spatial position perpendicular to cell surface
z		Number of electrons in charge-transfer step
z		Spatial position parallel to surface
α		Symmetry factor
α	$^{\mathrm{W}}/_{\mathrm{m^2 K}}$	Heat transfer coefficient
α_{con}	$^{1}/_{\mathrm{K}}$	Temperature-pre-factor for contact wire resistance
β		Symmetry factor in Butler-Volmer equation
Γ	$^{\mathrm{mol}}/_{\mathrm{m^2}}$	Density of adsorption sites
ε		Porosity
ϵ_{q}		Radiative emissivity
η	V	Overpotential
θ_i		Surface coverage of species i
λ_{q}	$^{\mathrm{W}}/_{\mathrm{K\,m}}$	Heat conductivity of species i
μ_i	$^{\mathrm{kg}}/_{\mathrm{s\,m}}$	Viscosity of species i

Symbol	Unit	Meaning
μ	$^{\mathrm{kg}}/_{\mathrm{s\,m}}$	Mixture-averages viscosity
ν_i		Stoichiometric factor of species i
ν_{at}	Hz	Attempt frequency
ρ_i	$^{\mathrm{kg}}/_{\mathrm{m}^3}$	Gas-phase density of species i
ρ_{con}	$^{(\Omega\mathrm{mm}^2)}/_{\mathrm{m}}$	Length-specific resistance of contact wire
σ_i		Surface sites occupied by species i
σ_{elyt}	$^{1}/_{\Omega\,\mathrm{m}}$	Ionic conductivity of electrolyte
$\sigma_{\mathrm{elyt}}^{\mathrm{eff}}$	$^{1}/_{\Omega\,\mathrm{m}}$	Effective ionic conductivity within composite electrode
τ		Tortuosity of porous medium
τ_{w}	Pa	Shear-stress factor
ϕ	V	Electrical potential
$\Delta\phi$	V	Potential difference between phases
Λ	$^{\mathrm{kg}}/_{\mathrm{m}^3\mathrm{s}^2}$	Radial pressure gradient
$\mathrm{V}_{\mathrm{O\,YSZ}}^{\bullet\bullet}$		Oxygen vacancy in YSZ lattice
$\square$		Free surface site
$\mathrm{H}_{\mathrm{i\,Ni}}^{\mathrm{x}}$		Interstitial hydrogen atom in the bulk nickel
$\mathrm{H}_{\mathrm{i\,YSZ}}^{\bullet}$		Interstitial proton in bulk YSZ
$\mathrm{O}_{\mathrm{O\,YSZ}}^{\mathrm{X}}$		Oxygen in the YSZ lattice

Bibliography

[1] A. Roberts. Staat ohne Land. *Der Spiegel*, 37, 2007.

[2] *Key World Energy Statistics 2008.* International Energy Agency, Paris, 2008.

[3] A. Heinzel, F. Mahlendorf, and J. Roes. *Brennstoffzellen.* Müller, Heidelberg, 2006.

[4] A. Atkinson, S. Barnett, R. J. Gorte, J. T. S. Irvine, A. J. McEvoy, M. Mogensen, S. C. Singhal, and J. Vohs. Advanced anodes for high-temperature fuel cells. *Nat. Mater.*, 3(1):17–27, 2004. ISSN 1476-1122.

[5] W. Vielstich, A. Lamm, and H. A. Gasteiger. *Handbook of Fuel Cells.* John Wiley & Sons, Inc., Chichester, 2003.

[6] P. Holtappels and U. Stimming. *Handbook of Fuel Cells*, Volume 1, Chapter Solid oxide fuel cells (SOFC), Pages 335–354. John Wiley & Sons, Inc., Chichester, 2003.

[7] P. W. Atkins. *Physikalische Chemie.* Wiley-VCH, Weinheim, 4. Auflage, 2006.

[8] B. C. H. Steele. Fuel-cell technology - running on natural gas. *Nature*, 400(6745): 619–621, 1999.

[9] H. Tu and U. Stimming. Advances, aging mechanisms and lifetime in solid-oxide fuel cells. *Journal of Power Sources*, 127(1-2):284–293, 2004.

[10] G. D. Agnew, R. D. Collins, M. Jorger, S. H. Pyke, and R. P. Travis. The components of a Rolls-Royce 1 MW SOFC system. *ECS Transactions*, 7:105–111, 2007.

[11] M. Nishiura, S. Koga, T. Kabata, N. Hisatome, K. Kosaka, Y. Ando, and Y. Kobayashi. Development of SOFC-micro gas turbine combined cycle system. *ECS Transactions.*, 7:155–160, 2007.

[12] J. Zizelman, J. Botti, J. Tachtler, and W. Strobl. Solid oxide fuel cell auxiliary power unit - a paradigm shift in electric supply for transportation. *SAE Technical Papers*, 2000-01:C070, 2000.

[13] M. Horiuchi, S. Suganuma, and M. Watanabe. Electrochemical power generation directly from combustion flame of gases, liquids, and solids. *J. Electrochem. Soc.*, 151:A1402–A1405, 2004.

[14] M. Nagao, M. Yano, K. Okamoto, A. Tomita, Y. Uchiyama, N. Uchiyama, and T. Hibino. A single-chamber sofc stack: Energy recovery from engine exhaust. *Fuel Cells*, 8(5):322–329, 2008.

[15] M. Gödickemeier and L. J. Gauckler. Engineering of solid oxide fuel cells with ceria-based electrolytes. *J. Electrochem. Soc.*, 145(2):414–421, 1998.

[16] A. Bieberle, L. Meier, and L. Gauckler. The electrochemistry of Ni pattern anodes used as solid oxide fuel cell model electrodes. *J. Electrochem. Soc.*, 148:A646–A656, 2001.

[17] J. Mizusaki, H. Tagawa, T. Saito, T. Yamamura, K. Kamitani, K. Hirano, S. Ehara, T. Takagi, T. Hikita, M. Ippommatsu, S. Nakagawa, and K. Hashimoto. Kinetic studies of the reaction at the nickel pattern electrode on YSZ in H_2-H_2O atmospheres. *Solid State Ionics*, 70-71(Part 1):52–58, 1994.

[18] B. de Boer. *Hydrogen oxidation at porous nickel and nickel/yttria-stabilised cermet anodes*. PhD thesis, University of Twente, 1998.

[19] A. Sukeshini, B. Habibzadeh, B. P. Becker, C. A. Stoltz, B. W. Eichhorn, and G. S. Jackson. Electrochemical oxidation of H_2, CO and CO/H_2 mixtures on patterned Ni anodes on YSZ electrolytes. *J. Electrochem. Soc.*, 153:A705–A715, 2006.

[20] D. Kek, M. Mogensen, and S. Pejovnik. A study of metal (Ni, Pt, Au)/Yttria-stabilized Zirconia interface in hydrogen atmosphere at elevated temperature. *J. Electrochem. Soc.*, 148:A878–A886, 2001.

[21] K. Vels Hansen, K. Norrman, and M. Mogensen. H_2-H_2O-Ni-YSZ Electrode performance. Effect of segregation to the interface. *J. Electrochem. Soc.*, 151(9):A1436–A1444, 2004.

[22] F. Behrendt, O. Deutschmann, B. Ruf, R. Schmidt, and J. Warnatz. Simulation of Heterogeneous Reaction Systems. In J. Wolfrum, H.-R. Volpp, R. Rannacher, and J. Warnatz, Editors, *Gas phase chemical reaction systems: experiment and models, 100 years after Max Bodenstein*. Springer, Heidelberg, 1996.

[23] V. M. Janardhanan and O. Deutschmann. Modeling of solid-oxide fuel cells. *Zeitschrift für Physikalische Chemie - International Journal of Research in Physical Chemistry*, 221(4):443–478, 2007.

[24] D. H. Jeon, J. H. Nam, and C. J. Kim. Microstructural optimization of anode-supported solid oxide fuel cells by a comprehensive microscale model. *J. Electrochem. Soc.*, 153(2):A406–A417, 2006.

[25] B. Rüger, A. Weber, and E. Ivers-Tiffée. 3D-Modelling and performance evaluation of mixed conducting (MIEC) cathodes. *ECS Transactions*, 7(1):2065–2074, 2007.

[26] H. Zhu and R. J. Kee. Modeling distributed charge-transfer processes in SOFC membrane electrode assemblies. *J. Electrochem. Soc.*, 155(7):B715–B729, 2008.

[27] W. G. Bessler and S. Gewies. Gas concentration impedance of solid oxide fuel cell anodes II. Channel geometry. *J. Electrochem. Soc.*, 154(6):B548–B559, 2007.

[28] W. G. Bessler, S. Gewies, and M. Vogler. A new framework for physically based modeling of solid oxide fuel cells. *Electrochimica Acta*, 53(4):1782–1800, 2007.

[29] S. Gewies and W. G. Bessler. Physically based impedance modeling of Ni/YSZ cermet anodes. *J. Electrochem. Soc.*, 155:B937–B952, 2008.

[30] J. O. Bockris, K. Amulya, N. Reddy, and M. Gamboa-Aldeco. *Modern Electrochemistry - Fundamentals of Electrodics*, Volume 2A. Kluwer Academic/Plenum Publishers, 2000.

[31] S. Adler and W. Bessler. *Handbook of Fuel Cells Vol. 5*, Volume 5, Chapter Elementary kinetic modeling of SOFC electrode reactions. Wiley, Chichester, UK, 2009.

[32] W. G. Bessler. Gas concentration impedance of solid oxide fuel cell anodes I. Stagnation point flow geometry. *J. Electrochem. Soc.*, 153(8):A1492–A1504, 2006.

[33] O. Deutschmann, S. Tischer, C. Correa, D. Chatterjee, S. Kleditzsch, and V. Janardhanan. DETCHEM Software Package, Version 2.0, http://www.detchem.com, 2004.

[34] V. M. Janardhanan and O. Deutschmann. CFD analysis of a solid oxide fuel cell with internal reforming: Coupled interactions of transport, heterogeneous catalysis and electrochemical processes. *J. Power Sources*, 162(2):1192–1202, 2006.

[35] H. Zhu, R. J. Kee, V. M. Janardhanan, O. Deutschmann, and D. G. Goodwin. Modeling elementary heterogeneous chemistry and electrochemistry in solid-oxide fuel cells. *J. Electrochem. Soc.*, 152:A2427–A2440, 2005.

[36] E. S. Hecht, G. K. Gupta, H. Zhu, A. M. Dean, R. J. Kee, L. Maier, and O. Deutschmann. Methane reforming kinetics within a Ni-YSZ SOFC anode support. *Appl. Catal., A*, 295(1):40–51, 2005.

[37] O. Deutschmann. *Modeling of Surface Reactions and their Coupling with Chemically Reacting Flows.* PhD thesis, University Heildeberg, 1996.

[38] W. Nolting. *Grundkurs Theoretische Physik 3 Elektrodynamik.* Zimmermann-Neufang, Ulmen, 1990.

[39] M. A. Khaleel and J. R. Selman. Cell, Stack and System Modelling. In S. C. Singhal and K. Kendall, Editors, *High-Temperature Solid Oxide Fuel Cells: Fundamentals, Design and Applications.* Elsevier Science, Oxford, 2003.

[40] J. Divisek, R. Jung, and I. C. Vinke. Structure investigations of SOFC anode cermets. Part II: Electrochemical and mass transport properties. *Journal of Applied Electrochemistry*, 29:165–170, 1999.

[41] J. M. Bisang, K. Jüttner, and G. Kreysa. Potential and current distribution in porous electrodes under charge-transfer kinetic control. *Electrochimica Acta*, 39(8-9):1297–1302, 1994.

[42] J. D. Solier, I. Cachadina, and A. Dominguez-Rodriguez. Ionic conductivity of ZrO_2-12 mol % Y_2O_3 single crystals. *Phys. Rev. B: Condensed Matter and Materials Physics*, 48(6):3704–3712, 1993.

[43] M. Filal, C. Petot, M. Mokchah, C. Chateau, and J. L. Carpentier. Ionic conductivity of yttrium-doped zirconia and the "composite effect" . *Solid State Ionics*, 80(1-2): 27–35, 1995.

[44] P. S. Manning, J. D. Sirman, R. A. De Souza, and J. A. Kilner. The kinetics of oxygen transport in 9.5 mol % single crystal yttria stabilised zirconia. *Solid State Ionics*, 100(1-2):1–10, 1997.

[45] I. Riess. Mixed ionic-electronic conductors–material properties and applications. *Solid State Ionics*, 157(1-4):1–17, 2003.

[46] Y. Hao and D. G. Goodwin. Numerical study of heterogeneous reactions in an SOFC anode with oxygen addition. *J. Electrochem. Soc.*, 155(7):B666–B674, 2008.

[47] Y. Hao, Z. Shao, J. Mederos, W. Lai, D. G. Goodwin, and S. M. Haile. Recent advances in single-chamber fuel-cells: Experiment and modeling. *Solid State Ionics*, 177, 2006.

[48] R. B. Bird, W. E. Stewart, and E. N. Lightfoot. *Transport phenomena.* John Wiley & Sons, New York, 2. Auflage, 2002.

[49] R. J. Kee, M. E. Coltrin, and P. Glarborg. *Chemically Reacting Flow Modeling: Theory and practice.* Wiley & Sons, 2003.

[50] J. Warnatz, U. Maas, and R. W. Dibble. *Verbrennung.* Springer, Heidelberg, 2001.

[51] W. G. Bessler. Electrochemistry and transport in solid oxide fuel cells. Habilitation, University Heidelberg, 2007.

[52] W. Hort, S. J. Linz, and M. Lücke. Onset of convection in binary gas mixtures: Role of the Dufour effect. *Phys. Rev. A*, 45(6):3737–3748, 1992.

[53] B. Todd. Mass transport in solid oxide fuel cell electrodes. In *Proceedings of the 2nd International Conference on Heat Transfer, Fluid Mechanics and Thermodynamics*, Victoria Falls, Zambia 2003.

[54] J. Warnatz, U. Maas, and R. W. Dibble. *Combustion. Physical and chemical fundamentals, modeling and simulation, experiments, pollutant formation.* Springer, Berlin; New York, 2006.

[55] O. Deutschmann, S. Tischer, S. Kleditzsch, C. Correa, D. Chatterjee, and J. Warnatz. *DETCHEM Software Package, Version 1.5.* http://www.detchem.com, Heidelberg, 2003.

[56] B. Todd and J. B. Young. Thermodynamic and transport properties of gases for use in solid oxide fuel cell modelling. *Journal of Power Sources*, 110(1):186–200, 2002.

[57] J. Warnatz. Calculation of the structure of laminar flat flames III: Structure of burner-stabilized hydrogen-oxygen and hydrogen-fluorine flames. *Ber. Bunsenges. Phys. Chem.*, 82:834–841, 1987.

[58] F. A. L. Dullien. *Porous media.* Academic Press, San Diego, 1992.

[59] J. Bear. *Dynamics of fluids in porous media.* Elsevier, New York, 1972.

[60] T. Zambelli, J. Trost, J. Wintterlin, and G. Ertl. Diffusion and Atomic Hopping of N Atoms on Ru(0001) Studied by Scanning tunneling microscopy. *Phys. Rev. Lett.*, 76(5):795–798, 1996.

[61] R. Gomer. Diffusion of Adsorbates on Metal Surfaces. *Rep. Prog. Phys.*, 53:917–1002, 1990.

[62] S. Singhal and K. Kendall. *High-Temperature Solid Oxide Fuel Cells: Fundamentals, Design and Applications.* Elsevier Science, Oxford, 2003.

[63] T. Horita, H. Kishimoto, K. Yamaji, Y. Xiong, N. Sakai, M. Brito, and H. Yokokawa. Materials and reaction mechanisms at anode/electrolyte interfaces for SOFCs. *Solid State Ionics*, Volume 177:1941–1948, 2006.

[64] M. Mogensen. SOFC fuel electrode kinetics and mechanisms. In *26th Risø International Symposium on Materials Science: Solid State Electrochemistry*, Solid State Electrochemistry, Roskilde, Denmark, 2005. Risø National Laboratory.

[65] M. Mogensen, J. Hoegh, K. Hansen, and T. Jacobsen. A critical review of models of the H_2/H_2O/Ni/YSZ electrode kinetics. *ECS Transactions*, 7:1329–1338, 2007.

[66] M. Mogensen and T. Lindegaard. The kinetics of hydrogen oxidation on a Ni-YSZ SOFC electrode at 1000°C. In H. Iwahara, Editor, *Third International Symposium on Solid Oxide Fuel Cells*, Pages 484–493. The Electrochemical Society Proceedings Series PV 93-4, 1993.

[67] R. J. Aaberg, R. Tunold, S. Tjelle, and R. Odegard. Oxidation of CO and H_2 on Ni/YSZ cermet electrodes. In *17th Risø International Symposium on Materials Science*. Risø National Laboratory, 1996.

[68] M. Ihara, T. Kusano, and C. Yokoyama. Competitive adsorption reaction mechanism of Ni/Yttria-stabilized zirconia cermet anodes in $H_2 - H_2O$ solid oxide fuel cells. *J. Electrochem. Soc.*, 148:A298–A219, 2001.

[69] V. Chebotin, M. Glumov, A. Neuimin, and S. Palguev. Polarization of a hydrogen electrode on a solid oxide electrolyte. *Soviet Electrochemistry*, 7:55–60, 1971.

[70] A. Bieberle. *The Electrochemistry of Solid Oxide Fuel Cell Anodes: Experiments, Modeling, and Simulations*. PhD thesis, Swiss Federal Insitute of Technology, 2000.

[71] W. Bessler. A new computational approach for SOFC impedance from detailed electrochemical reaction-diffusion models. *Solid State Ionics*, 176:997–1001, 2005.

[72] R. Williford. Modeling of environmentally significant interfaces: Two case studies. *J. Electron Spectrosc. Relat. Phenom.*, 150(2-3):171–184, 2006.

[73] R. Williford and L. Chick. Surface Diffusion and Concentration Polarisation on Oxide-Supported metal electrocatalyst particles. *Surf. Sci.*, 547:421–437, 2003.

[74] D. Goodwin. A pattern anode model with detailed electrochemistry. In J. Mizusaki, Editor, *Ninth international symposium on solid oxide fuel cells (SOFC-IX)*, Pages 699–707, Quebec City, Canada, 2005.

[75] S. P. Jiang and S. P. S. Badwal. Hydrogen oxidation at the nickel and platinum electrodes on yttria-tetragonal zirconia electrolyte. *J. Electrochem. Soc.*, 144:3777–3784, 1997.

[76] A. B. Anderson and E. Vayner. Hydrogen oxidation and proton transport at the Ni-zirconia interface in solid oxide fuel cell anodes: Quantum chemical predictions. *Solid State Ionics*, 177:1355–1359, 2006.

[77] G. X. Cao, E. Nabighian, and X. D. Zhu. Diffusion of Hydrogen on Ni(111) over a Wide Range of Temperature: Exploring Quantum Diffusion on Metals. *Phys. Rev. Lett.*, 79(19)(19):3696–3699, 1997.

[78] S. Raz, K. Sasaki, J. Maier, and I. Riess. Characterization of adsorbed water layers on Y_2O_3 -doped ZrO_2. *Solid State Ionics*, 143:181–204, 2001.

[79] A. S. Ioselevich and A. A. Kornyshev. Phenomenological theory of solid oxide fuel cell anode. *Fuel Cells*, 1:40–65, 2001.

[80] A. Bieberle and L. J. Gauckler. State-space modeling of the anodic SOFC system Ni, H_2-H_2, O_{YSZ}. *Solid State Ionics*, 146(1-2):23–41, 2002.

[81] J. Mukherjee and S. Linic. First-principles investigations of electrochemical oxidation of hydrogen at solid oxide fuel cell operating conditions. *J. Electrochem. Soc.*, 154: B919–B924, 2007.

[82] J. Rossmeisl and W. Bessler. Trends in Catalytic Activity for SOFC Anode Materials. *Solid State Ionics*, 178:1694–1700, 2008.

[83] B. Luerßen, E. Mutoro, H. Fischer, S. Günther, R. Imbihl, and J. Janek. In situ imaging of electrochemically induced oxygen spillover on Pt/YSZ catalysts. *Angew. Chem. Int. Ed.*, 45:1473–1476, 2006.

[84] M. Mogensen, S. Sunde, and S. Primdahl. SOFC anode kinetics. In *17th Risø International Symposium on Materials Science*, Pages 77–100, Risø National Laboratory, Roskilde, Denmark, 1996.

[85] S. Primdahl and M. Mogensen. Oxidation of hydrogen on Ni/Yttria-stabilized Zirconia cermet anodes. *J. Electrochem. Soc.*, 144:3409–3419, 1997.

[86] P. Holtappels, L. de Haart, and U. Stimming. Reaction of hydrogen/water mixtures on Nickel-Zirconia cermet electrodes. I. dc polarization characteristics. *J. Electrochem. Soc.*, 146:1620–1625, 1999.

[87] N. Q. Minh and T. Takahashi. *Science and technology of ceramic fuel cells.* Elsevier, Amsterdam, 1995.

[88] M. Brown, S. Primdahl, and M. Mogensen. Structure/performance relations for Ni/Yttria-stabilized Zirconia anodes for solid oxide fuel cells. *J. Electrochem. Soc.*, 147:475–485, 2000.

[89] J. Nowotny, C. C. Sorrell, and T. Bak. Segregation in zirconia: equilibrium versus non-equilibrium segregation. *Surf. Interface Anal.*, 37:316–324, 2005.

[90] P. Deuflhard, E. Hairer, and J. Zugck. One step and extrapolation methods for differential-algebraic systems. *Num. Math.*, 51:501–516, 1987.

[91] M. Chase, C. Davies, J. Downey, D. Frurip, R. McDonald, and A. Syverud. JANAF Thermochemical Tables. *J. Phys. Chem. Ref. Data*, 14, 1985.

[92] R. B. McLellan and W. A. Oates. The solubility of Hydrogen in Rhodium, Ruthenium, Iridium and Nickel. *Acta Mater.*, 21:181–185, 1973.

[93] C. Wagner. Die Löslichkeit von Wasserdampf in $ZrO_2 - Y_2O_3$-Mischkristallen. *Ber. Bunsenges. Phys. Chem.*, 72:778–781, 1968.

[94] X. Guo. On the degradation of zirconia ceramics during low-temperature annealing in water or water vapor. *J. Phys. Chem. Solids*, 60(4):539–546, 1999.

[95] C. Ratsch and M. Scheffler. Density-functional theory calculation of hopping rates of surface diffusion. *Phys. Rev. B: Condens. Matter Mater. Phys.*, 58-19:163–166, 1998.

[96] M. Kizilyalli. Definition of Terms for Diffusion in the Solid State. *Pure Appl. Chem.*, 71:1307–1325, 1999.

[97] A. Tilocca and A. Selloni. Reaction pathway and free energy barrier for defect-induced water dissociation on the (101) surface of TiO_2-anatase. *J. Chem. Phys.*, 119(14):7445–7450, 2003.

[98] J. H. Nowotny. *Surface and near-surface chemistry of oxide materials*, Volume 47. Elsevier, Amsterdam, 1988.

[99] K. Sasaki and J. Maier. Chemical surface exchange of oxygen on Y_2O_3-stabilized ZrO_2. *Solid State Ionics*, 161(1-2):145–154, 2003.

[100] P. S. Manning, J. D. Sirman, and J. A. Kilner. Oxygen self-diffusion and surface exchange studies of oxide electrolytes having the fluorite structure. *Solid State Ionics*, 93(1-2):125–132, 1996.

[101] M. Weller, R. Herzog, M. Kilo, G. Borchardt, S. Weber, and S. Scherrer. Oxygen mobility in yttria-doped zirconia studied by internal friction, electrical conductivity and tracer diffusion experiments. *Solid State Ionics*, 175(1-4):409–413, 2004.

[102] M. Kilo, C. Argirusis, G. Borchardt, and R. Jackson. Oxygen diffusion in yttria stabilised zirconia - experimental results and molecular dynamics calculations. *Phys. Chem. Chem. Phys.*, 5(11):2219–2224, 2003. ISSN 1463-9076.

[103] C. G. Vayenas, S. Bebelis, C. Pliangos, S. Brosda, and D. Tsiplakides. *Electrochemical activation of catalysis. Promotion, Electrochemical Promotion, and Metal-Support Interactions.* Kluwer Academic/Plenum Publishers, New York, 2001.

[104] F. Parmigiani, L. Deperp, L. Sangaletti, and G. Samoggia. An XPS study of yttria-stabilised zirconia single crystals. *Electron Spectrosc. Relat. Phenom.*, 63:1–10, 1993.

[105] B. Bhatia and D. S. Sholl. Chemisorption and diffusion of hydrogen on surface and subsurface sites of flat and stepped nickel surfaces. *J. Chem. Phys.*, 122(20):204707, 2005.

[106] G. Watson, R. Wells, D. Willock, and G. Hutchings. A Comparison of the Adsorption and Diffusion of Hydrogen on the 111 Surfaces of Ni, Pd, and Pt from Density Functional Theory Calculations. *J. Phys. Chem. B*, 105(21):4889–4894, 2001.

[107] O. R. Inderwildi, D. Lebiedz, O. Deutschmann, and J. Warnatz. Coverage dependence of oxygen decomposition and surface diffusion on rhodium (111): A DFT study. *J. Chem. Phys.*, 122(3):034710–034718, 2005.

[108] J. Rossmeisl. Dansk Technical University. Personal communication, 2007.

[109] W. Bartczak and J. Stawowska. Potential barriers for surface diffusion of O and C atoms, OH and CH radicals and CO molecules at the metal (Pd, Ni) surfaces. In *Conference Paper from EFCATS School on Catalysis*, 2004.

[110] J. Völkl and G. Alefeld. *Diffusion of hydrogen in metals. Hydrogen in metals.* Springer, 1978.

[111] D. Martin and D. Duprez. Mobility of Surface Species on Oxides. 1. Isotopic Exchange of $^{18}O_2$ with ^{16}O of SiO_2, Al_2O_3, ZrO_2, MgO, CeO_2, and CeO_2-Al_2O_3. Activation by Noble Metals. Correlation with Oxide Basicity. *J. Phys. Chem.*, 100(22):9429–9438, 1996. ISSN 0022-3654.

[112] A. Galdikas, C. Descorme, and D. Duprez. Surface diffusion upon oxygen isotopic exchange on oxide-supported metal nanoclusters. *Solid State Ionics*, 166(1-2):147–155, 2004.

[113] E. Wahlstrom, E. K. Vestergaard, R. Schaub, A. Ronnau, M. Vestergaard, E. Laegsgaard, I. Stensgaard, and F. Besenbacher. Electron Transfer-Induced Dynamics of Oxygen Molecules on the TiO_2(110) Surface. *Science*, 303(5657):511–513, 2004.

[114] G. A. Somorjai. *Introduction to surface chemistry and catalysis.* Wiley, New York, 1994.

[115] A. E. Hughes and S. P. S. Badwal. Impurity and yttrium segregation in yttria-tetragonal zirconia. *Solid State Ionics*, 46(3-4):265–274, 1991.

[116] Y. L. Liu, S. Primdahl, and M. Mogensen. Effects of impurities on microstructure in Ni/YSZ-YSZ half-cells for SOFC. *Solid State Ionics*, 161(1-2):1–10, 2003.

[117] K. V. Jensen, R. Wallenberg, I. Chorkendorff, and M. Mogensen. Effect of impurities on structural and electrochemical properties of the Ni-YSZ interface. *Solid State Ionics*, 160(1-2):27–37, 2003.

[118] Y. Hao, Z. Shao, J. Mederos, W. Lai, D. G. Goodwin, and S. M. Haile. Recent advances in single-chamber fuel-cells: Experiment and modeling. *Solid State Ionics*, 177(19-25):2013–2021, 2006.

[119] Z. Shao, S. M. Haile, J. Ahn, P. D. Ronney, Z. Zhan, and S. A. Barnett. A thermally self-sustained micro solid-oxide fuel-cell stack with high power density. *Nature*, 435 (7043):795–798, 2005. ISSN 0028-0836.

[120] T. Hibino, A. Hashimoto, T. Inoue, J.-i. Tokuno, S.-i. Yoshida, and M. Sano. A low-operating-temperature solid oxide fuel cell in hydrocarbon-air mixtures. *Science*, 288 (5473):2031–2033, 2000.

[121] J. Bingue, A. Saveliev, A. Fridman, and L. Kennedy. Hydrogen production in ultra-rich filtration combustion of methane and hydrogen sulfide. *Int. J. Hydrogen Energy*, 27:643–649, 2002.

[122] H. Pedersen-Mjaanes, L. Chan, and E. Mastorakos. Hydrogen production from rich combustion in porous media. *Int. J. Hydrogen Energy*, 30:579–592, 2005.

[123] T. Hibino, A. Hashimoto, T. Inoue, J. ichi Tokuno, S. ichiro Yoshida, and M. Sano. A solid oxide fuel cell using an exothermic reaction as the heat source. *Journal of The Electrochemical Society*, 148(6):A544–A549, 2001.

[124] M. Horiuchi, M. Suganuma, S. Watanabe, and Y. Tokutake. Direct flame fuel cells - SOFC operation with combustion flames. In M. Mogensen, Editor, *Proceedings of the 6th European Solid Oxide Fuel Cell Forum, Lucerne, Switzerland*, Volume 6, Pages 154–162, 2004.

[125] H. Kronemayer, D. Barzan, M. Horiuchi, S. Suganuma, Y. Tokutake, C. Schulz, and W. Bessler. A direct-flame solid oxide fuel cell (DFFC) operated on methane, propane, and butane. *Journal of Power Sources*, 166:120–126, 2007.

[126] H. Kronemayer, W. Bessler, M. Vogler, M. Horiuchi, S. Suganuma, Y. Tokutake, C. Schulz, and J. Warnatz. A flame as fuel reformer for solid oxide fuel cells. In *Proceedings of the Seventh European Solid Oxide Fuel Cell Forum, Lucerne*, 2006.

[127] P. S. Gregory, G. David M., F. Michael, M. Nigel W., E. Boris, G. Mikhail, B. C. Thomas, H. Ronald K., S. Song, G. J. William C., L. Vitali V., and Q. Zhiwei. GRI-Mech 3.0, http://www.me.berkeley.edu/gri_mech. Web page.

[128] O. Deutschmann, R. Schwiedernoch, L. Maier, and D. Chatterjee. Natural gas conversion in monolithic catalysts: Interaction of chemical reactions and transport phenomena. In E. Iglesia, J. Spivey, and T. Fleisch, Editors, *Natural Gas Conversion VI, Studies in Surface Science and Catalysis*, Volume 136, Pages 215–258. Elsevier, 2001.

[129] W. Bessler, M. Vogler, O. Maykivets, J. Warnatz, H. Kronemayer, H. Yang, and C. Schulz. Modeling and experimental study of a direct flame fuel cell. Technical report, Shinko Electric Industries, 2007.

[130] V.-G. V. und Chemieingenieurswesen, Editor. *VDI Wärmeatlas*, Volume 4. Springer, Berlin, 1984.

[131] S. D. Alaruri, L. Bianchini, and A. J. Brewington. Emissivity measurements for YSZ thermal barrier coating at high temperatures using a 1.6-μm single-wavelength pyrometer. *Optical Engineering*, 37:683–687, 1998.

[132] G.-B. Jung, T.-J. Huang, and C.-L. Chang. Effect of temperature and dopant concentration on the conductivity of samaria-doped ceria electrolyte. *Journal of Solid State Electrochemistry*, 6(4):225–230, 2002.